ISSN 1028-8546

Volume XXVIII Number 2
Section: En July, 2022

Azerbaijan Journal of Physics

Fizika

www.physics.gov.az
www.physics.gov.az/ajpfizika.html

Institute of Physics
Azerbaijan National Academy of Sciences
Department of Physical, Mathematical and Technical Sciences

Published from 1995
Ministry of Press and Information
of Azerbaijan Republic,
Registration number 514, 20.02.1995

ISSN 1028-8546
vol. XXVIII, Number 02, 2022
Section: En

Azerbaijan Journal of Physics

FIZIKA

Institute of Physics
Azerbaijan National Academy of Sciences
Department of Physical, Mathematical and Technical Sciences

PUBLISHING OFFICE

131, H. Javid ave., AZ-1143, Baku
ANAS, Institute of Physics

Tel.: (99412) 539-51-63, 539-32-23
Fax: (99412) 537-22-92
E-mail: jophphysics@gmail.com
Internet: www.physics.gov.az

Published at "_____"
_____str., Baku

Sent for printing on: __.__. 201_
Printing approved on: __.__. 201_
Physical binding:_____
Number of copies:_____200
Order:_____

It is authorized for printing:

EFFECT OF GAMMA IRRADIATION ON THE CRYSTAL STRUCTURE OF $Cd_{1-x}Fe_xTe$ THIN FILMS

A. A. ABDULLAYEVA
Azerbaijan Technical University, Baku, Azerbaijan
H. Javid avn. 25, Baku, Azerbaijan, AZ1073
c.aybeniz@hotmail.com

In the present investigations effect of *γ*-irradiation on crystal structure and surface morphology of $Cd_{1-x}Fe_xTe$ (x = 0.08) thin films were studied. The properties of thin films exposed to *γ*- rays of 50, 100 and 150 kGy doses were characterized by XRD, SEM, EDX methods. XRD analysis confirmed the change in orientation of crystal planes after *γ*- exposure. It was defined that the peak intensity of (111) plane increased with irradiation dose and crystallite sizes were increased.

Keywords: Thin film, semimagnetic semiconductor, SEM, XRD, EDX, *γ*-radiation.
PACS: 81.15.-z, 61.05.c-, 61.80.Ed

1. INTRODUCTION

Obtain of new semiconductor materials, study of their physical properties, purposeful management and identification of applications in the creation of devices is one of the important issues of modern material science.

Thin films of II-VI compounds are attractive candidates for various optoelectronic applications in engineering. Bulk crystals of $Cd_{1-x}Fe_xTe$ semimagnetic semiconductors (SMSC) have been successfully used in modern instrumentation, especially in solar cells, radiation detectors, IR detectors, photodetectors, optical insulators, and etc. However, today it is impossible to imagine modern electronics without thin films. Because the devices are created on the crystals surface and all structural changes are reflected in the parameters of the devices, it is necessary to obtain thin films with a perfect crystal structure and clean smooth surface.

On the other hand, obtain of radiation-resistant and radiation-sensitive materials with stable physical properties is one of the actual problems of modern physics. It should be noted that under certain conditions, materials exposed to the strongest effects of ionizing radiation, change their physical properties due to the formation of radiation defects. Therefore, the study of effect of ionizing radiation on the physical properties of semiconductor materials is relevant.

It should be noted that $Cd_{1-x}Fe_xTe$ thin films are considered to be of special importance for fundamental research and practical application [1-5]. Few works have been devoted to the study of their physical properties. Present work devoted to the investigations of effect of *γ*-irradiation on crystal structure and surface morphology of $Cd_{1-x}Fe_xTe$ (x=0.08) thin films.

2. METODOLOGY

$Cd_{1-x}Fe_xTe$ (x=0.08) SMSC thin films of thickness 1.2 μm were deposited on cleaned glass substrates at the rate of υ=18-20 Å/s by molecular beam condensation technique in a vacuum of 10^{-4} Pa. All technical details of the preparation methodology were given in our earlier works [4].

The films were irradiated with γ- rays obtained from a ^{60}Co source of E=1.17MeV, E=1.33MeV energies.

The structure and phase purity of the as-deposited and irradiated films were checked at room temperature by means of X-ray diffraction (XRD) using a BRUKER XRD D8 ADVANCE.

The studies of surface morphology were performed on the JEOL JSM-7600F Field Emission SEM.

3. EXPERIMENTAL AND RESULTS

Since the characteristics of electronic devices are mainly related to the surface morphology of the crystals, the study of external influences (temperature, pressure, illumination, radiation, etc.) on their surface diagnostics is of particular importance. It is known that one of the most convenient methods for the modification of semiconductor materials is radiation technology. Thus, it is possible to control the physical properties of materials by irradiation of material and predict the characteristics of the devices on their base. In this regard, it is of great interest to study the changes in the surface of the $Cd_{1-x}Fe_xTe$ thin films as a result of the effects of γ-radiation. The results of SEM and XRD studies of $Cd_{1-x}Fe_xTe$ (x= 0.08) thin films exposed to γ-irradiation ($D_\gamma \leq 200$kGy) are presented in this study.

X-ray diffraction pattern of as-prepared $Cd_{1-x}Fe_xTe$ (x = 0.08) thin films is shown in fig. 1,a. The XRD measurement reveals that all the sharp diffraction peaks (111), (220), (311), (400), (331) and (422) confirmed face centered cubic structure of $Cd_{1-x}Fe_xTe$ with crystal lattice parameter of a=6,47Å. The crystallite size of $Cd_{1-x}Fe_xTe$ (x = 0.08) thin films may be estimated from the width of the XRD peak using Debye–Scherrer's formula [6] given by

$$D = (0.9\,\lambda)/(\beta \cos\theta)$$

where, D - is crystallite size, β - is full width at half maxima (FWHM) of the peak intensity, θ - is diffraction angle in degrees and λ - is the wavelength of X-ray used (1.54060 A˚). The average crystallite size of $Cd_{1-x}Fe_xTe$ thin films was found to be 1.7 nm (table 1).

131, H.Javid ave, AZ-1143, Baku
ANAS, Institute of Physics
E-mail: jophphysics@gmail.com

№	2θ (deg)	Crystal system (hkl)	FWHM, β (deg)	Crystal size, D (nm)
1	24	111	0.15	2.2
2	39.5	220	0.15	4.24
3	46.5	311	0.15	1.15
4	57	400	0.1	1.55
5	62.5	331	0.25	0.6
6	71.5	422	0.25	0.8
7	76.5	111	0.2	1.46

a

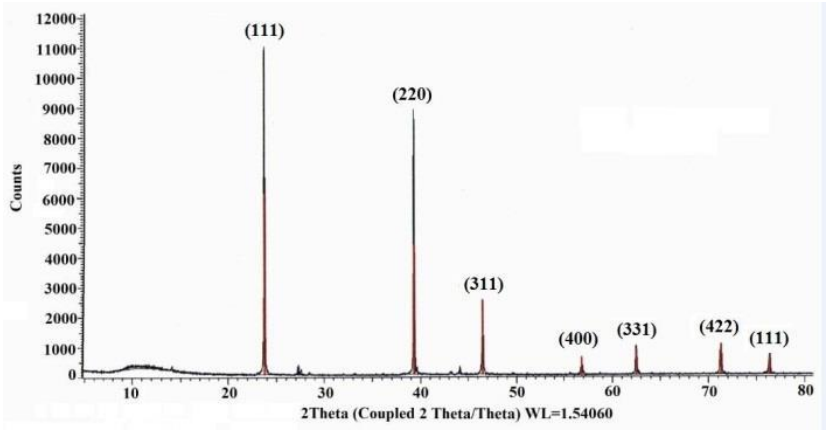

b

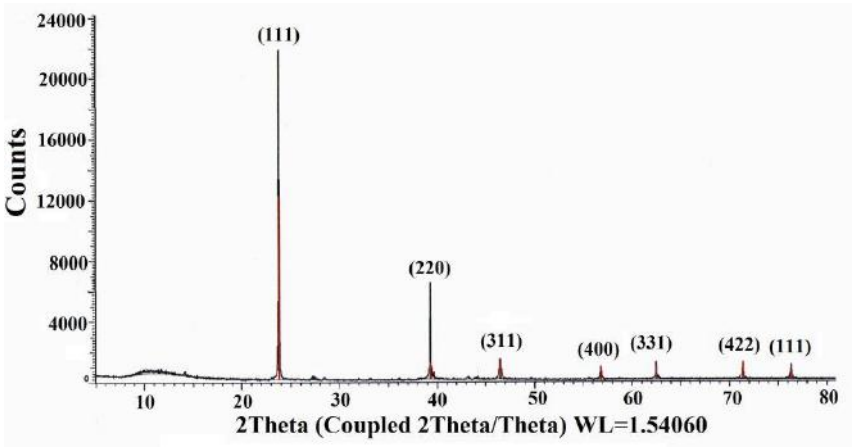

c

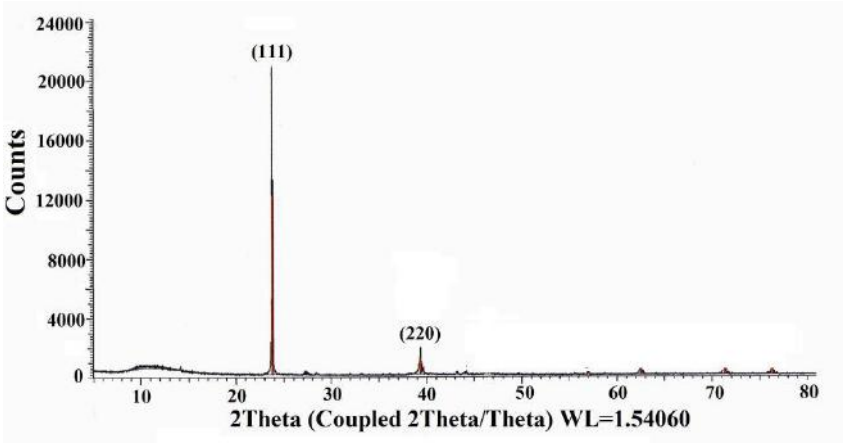

Fig.1. X-ray diffraction patterns of $Cd_{1-x}Fe_xTe$ (x=0.08) thin films a) D_γ =0, b) D_γ = 100 kGy, c) D_γ = 150 kGy

XRD patterns of pristine $Cd_{1-x}Fe_xTe$ thin film on glass substrate and further irradiated with γ- radiation (E=1.17MeV, E=1.33MeV) with different doses ($D_\gamma \leq 200$ kGy) are shown in fig. 1. The diffraction pattern of γ -irradiated thin films with different doses 50, 100 and 150 kGy revealed that the peak intensity of (111) plane of $Cd_{1-x}Fe_xTe$ increased with dose. This indicates that the number of planes aligned along the (111) direction increased with γ- irradiation. This is because ^{60}Co γ -rays are high energy electromagnetic waves. When the radiation dose is large enough (100 kGy and 150 kGy) the surface energy will play an important role in the crystal growth process. In this process, atoms are easy to be attracted by (111) crystal face with high surface energy and condense there, which can result in the preferential growth of (111) plane [7]. Thus, XRD analysis confirmed the change in orientation of planes after gamma exposure.

The SEM method was used to study the effect of γ-irradiation on the surface morphology of $Cd_{1-x}Fe_xTe$ (x=0.08) thin films (fig.2). The morphology of $Cd_{1-x}Fe_xTe$ thin film was analyzed by SEM before and after γ- irradiation (Fig. 2). $Cd_{1-x}Fe_xTe$ (x=0.08) thin films irradiated by γ-quanta at a dose of D_γ=100 kGy, which is due to the interaction of γ-quanta with atoms in their path during irradiation.

After gamma irradiation, $Cd_{1-x}Fe_xTe$ crystallite size was increased (Fig. 2b) which is a good agreement with XRD results. Compositional analysis of pristine $Cd_{1-x}Fe_xTe$ thin film was done using Energy Dispersive X-Ray Analysis (EDX) shown in fig. 3.

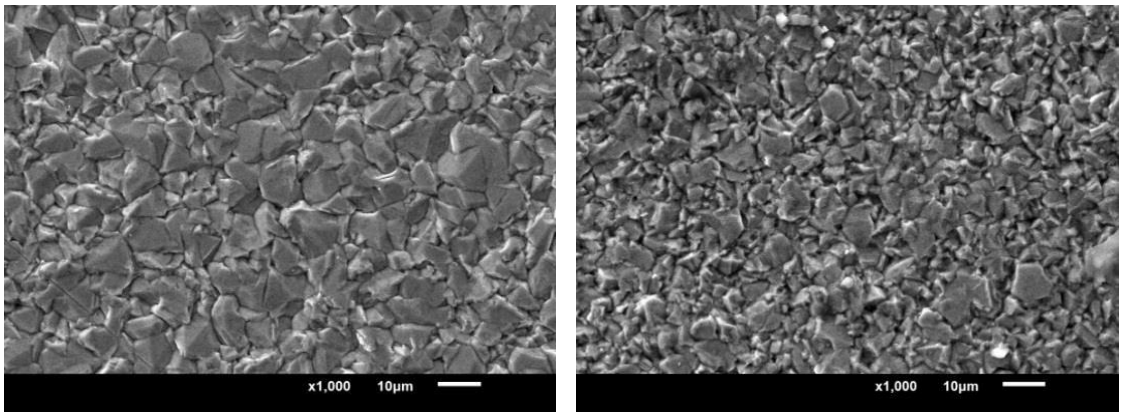

a) b)

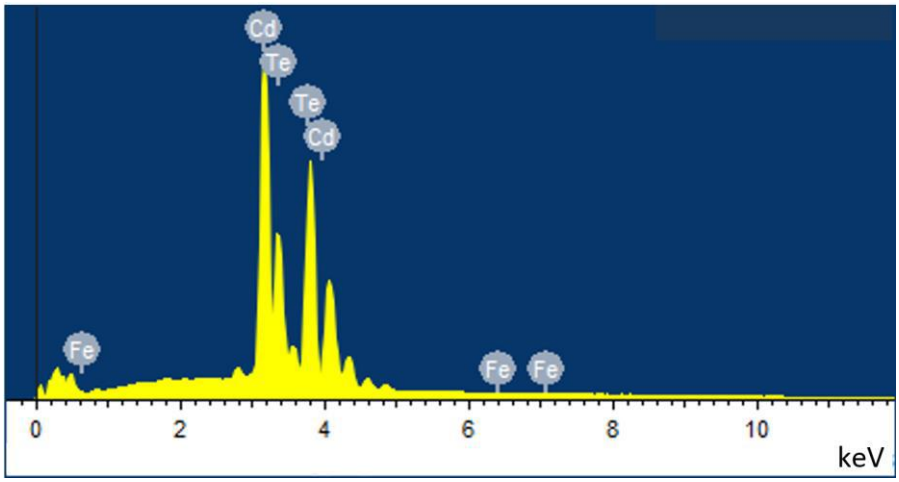

Fig.2. SEM imaging of the surface morphology of $Cd_{1-x}Fe_xTe$ (x=0.08) thin films: a) D_γ=0, b) D_γ = 100kGy.

Element	Weight %	Atom%
Fe K	0.08	0.16
Cd L	47.33	50.45
Te L	52.60	49.39
Total	100.00	100.00

Fig. 3. EDX analysis of pristine $Cd_{1-x}Fe_xTe$ (x = 0.08) thin film.

4. CONCLUSION

In the present investigations, $Cd_{1-x}Fe_xTe$ (x = 0.08) solid solutions were synthesized and thin films were obtained on their base by molecular beam condensation technique. We studied effect of *γ*-irradiation on crystal structure and surface morphology of obtained thin films. The properties of $Cd_{1-x}Fe_xTe$ ($x = 0.08$) thin films exposed to 50, 100 and 150 kGy doses of *γ*- rays from ^{60}Co source were characterized by XRD, SEM, EDX methods. XRD analysis revealed that the peak intensity of (111) plane of $Cd_{1-x}Fe_xTe$ increased with dose. After *γ*- irradiation, crystallite size was increased. Thus, it is possible to manage some crystal properties by γ-irradiation.

[1] *P. Zhukovski, Ya. Partyka., P. Vengerek, T. Koltunovich, Yu. Sidorenko, V. Stelmakh, N. Lapchuk.* Conductivity and electron paramagnetic resonance of $Cd_{1-x}Fe_xTe$ compounds. Semiconductors. 2007, v. 41, №5, p. 544-548.

[2] *A. Kisiel.* X-ray absorption near edge structure analysis of CdFeTe: XANES experiment and theoretical LMTO calculations. Solid State Communications. 1992, v. 81, №2, p. 151–154.

[3] *C. Testelin, C. Rigaux, A. Mycielski, M. Menant,*

[4] *M. Guillot.* Exchange interactions in CdFeTe semimagnetic semiconductors. Solid State Communications**.** 1991, v. 78, №7, p. 659–663.

[5] *I.R. Nuriyev, A.M. Nazarov, M.A. Mehrabova, R.M. Sadigov.* Growth features, structure and surface morphology of $Cd_{1-x}Fe_xTe$ epitaxial films. Journal of Inorganic Materials. 2016, v. 52, №.9, p. 1-4.

[6] *M.A. Mehrabova, H.R. Nuriyev, H.S. Orujov, N.H. Hasanov, T.I. Kerimova, A.A. Abdullayeva, A.I. Kazimova.* Effect of gamma irradiation on conductivity of $Cd_{1-x}Fe_xTe$. FTT, 2019, №12, p. 2306–2309.

[7] *S. Shanmugan, D. Mutharasu.* An effect of N+ ion bombardment on the CdTe thin films, Radiation Physics Chemistry 2012, 81, 2, p. 201-207.

[8] *Z. Wang, W. Jiang, S. Li, J.S. Tong.* Effects of ^{60}Co γ-ray irradiation on microstructure and ferroelectric properties of $Bi_{3.25}La_{0.75}Ti_3O_{12}$ thin films. Nucl. Instrum. Methods. Phys. Res. B 2016, 366, p. 1-5.

Received: 28.02.2022

CRYSTALLIZATION KINETICS OF AMORPHOUS NANOTHICKNESS $CuGa_5Se_8$

A.Ch. MAMEDOVA[1], N.K. KERIMOVA[2], I.T. MAMMADOVA[1]

[1]Institute of Physics of Azerbaijan National Academy of Sciences, AZ-1143, H. Javid ave., 131, Baku, Azerbaijan
[2] Azerbaijan State University of Economics, AZ – 1001, Istiglaliyyat Street, Baku, Azerbaijan
amamedova@inbox.ru

The processes of phase formation and phase transitions in $CuGa_5Se_8$ thin layers allowing the carrying out of the continuous object shooting at treatment different conditions are investigated by kinematic electronography method. It is shown, that amorphous films form at evaporation of synthesized compound and thermal spraying of binary compounds Cu_2Se and Ga_2Se_3 in ratio 1:5. There have been established kinetic parameters of $CuGa_5Se_8$ compositions amorphous films crystallization. The crystal growth regularity, activation energy values of germ – formation and their further growth are obtained.

Keywords: crystallizations kinetics, amorphous film, nano-thickness.
PACS: 548.74; 539,234

1. INTRODUCTION

The interest in defective-ordered compounds $CuGa_5(In_5)Se_8$ related to the system $A^1 – B^3- C^6$[A-Cu, B – (In,Ga), C- (S,Se,Te)] is caused by the width of their band gaps. For $CuGa_5Se_8$, the band gap (E_G) is 1.85 eV [3].

To study the processes of phase formation and phase transformations in nanothick films $Cu(In,Ga)_5Se_8$), recognized in [4,5] as promising materials for creating high-efficiency solar cells of a new generation, the high-energy diffraction method was used.

The aim of this work is to determine the conditions of the synthesis of $CuGa_5Se_8$ formed during the vacuum condensation of double compositions Cu_2Se, Ga_2Se_3, and kinetic parameters of the crystallization of amorphous $CuGa_5Se_8$ films.

The main method for determination of crystal structure and phase compositions of thin layers is the electron beam diffraction on nanodimensional films. The essence of kinematic electronography method based on rapid electron diffraction on objects, the dimensions of which are commensurable ones with wavelength of incident radiation, is the fact that diffraction picture is fixed on moving photographic plate which is mechanically drawn. The stationary values of activation energies showing on phase transition end when whole material of different compositions taking part in process transits from the amorphous state into crystal one or from the one crystal modification into another one, are obtained by kinematic electronoqraphy for thin films of each compound. The coherently scattered electrons having the big sensitivity to relatively scattered substance allow us to fix the reaction beginning and follow its further motion. This method can't be considered as alternative one to X – ray spectrometry and other optic methods not applying to nano –thickness films. The kinematic electronography is the unique independent method for quantitative investigations of phase transformation kinetics taking place in nano - thickness amorphous and crystalline films: texture, polycrystalline, monocrystalline films. The data obtained by this method can't be found with enough definiteness by other above-mentioned methods which aren't potentially suitable for films by thickness by several decades nanometers. The result interpretation obtained by kinematic electronography presents the big interest for semiconductor material science. They can be based on optical measurements up to present time and give the direct comparison possibility of obtained result for thin films with data for massive samples.

2. EXPERIMENT TECHNIQUE

The very narrow strip is cut from total diffraction patterns by kinematic method with the help of shutters being in electron diffractograph EMR-102. using these shutters one can make the gap of any width. As diffraction maximum width on photo – plate increases with gap increase then the diffraction ring curvature strongly reveals with gap increase. However, the diffraction lines from polycrystalline sample keep its width and sharpness within limits of gap width change. The gap width at photo – plate drawing is selected by shutter establishment and in dependence on primary beam intensity one can be established in limits 0,1; 0,3; 0,5 mm. The instrument constant $2L\lambda$ was 52,73 mm Å at an accelerating voltage of 75 kV. It should switch off the forepump and close the fore valve for neutralization of vibrations from vacuum forepump at electron diffraction pattern kinematic shooting.

The study complexity of kinetics amorphous film crystallization processes and appearance of new crystalline modifications in case of phase transformations is in the fact that mechanism crystallization center formation and their further growth is often unknown. The data on crystal growth

131, H.Javid ave, AZ-1143, Baku
ANAS, Institute of Physics
E-mail: jophphysics@gmail.com

mechanism and dependence of phase transformation rate on temperature one can obtain by studying of time – temperature dependences of amorphous film crystallization and thin crystal layers recrystallization with establishment of phase transition kinetic parameters.

The thin – film materials suitable for investigations by diffraction method of high – energy electrons are obtained by both evaporation of synthesized compound $CuGa_5Se_8$ and thermal spraying of binary compounds of Cu_2Se and Ga_2Se_3 in ratio 1:5. At simultaneous and layer – by – layer precipitation of Cu_2Se and Ga_2Se_3 the evaporation sources which are tungsten baskets of conic profile lag behind each other on distance 150 mm at height 70 mm relatively to freshly cleaved NaCl and grids covered by celluloid serving as substrates. The vapor condensation is carried out on substrates being at room temperature in vacuum, the residual gas pressure in which is ~10^{-4} Pa. The precipitation rate is ~0,2 nm/sec. For prevention of re –evaporation and thin – film sample oxidation in case of their thermal treatment at high temperatures, the thin films are covered by celluloid thin layer so that they are involved in singular capsule. It should be noted that at temperatures 423 K and higher the celluloid protective film destroys. For removal of such processes, the probabilities of oxidation in air and decomposition in the process of following thermal treatments at increased temperatures or at their long storage, the investigated samples are capsulated by thin layers of amorphous carbon [1-2]. Taking into consideration the carbon layer thickness the total thickness of investigated objects doesn't exceed ~ 50 nm. The structural characteristics of $CuGa_5Se_8$ thin layers obtained on NaCl and KCl surfaces being at different temperatures and film phase composition formed by simultaneous and consistent evaporation of Cu_2Se and Ga_2Se_3 are studied on electron diffractograph EMR-102.

3. RESULTS AND THEIR DISCUSSION

The layer-by-layer precipitation of Cu_2Se and Ga_2Se_3 on substrates at room temperature leads to phase distribution on condensation plane corresponding to calculated component composition at both simultaneous evaporation and independent on evaporation order.

On the base of scheme of phase according to experimental data obtained as the result of analysis of electron diffraction pattern taken from points situated from each other on distance 4 mm, it is established that forming films are amorphous ones in substrate region where by calculation the triple compound of $CuGa_5Se_8$ composition should form. The diffuse lines of electron diffraction pattern from amorphous films contain values $S = 4\pi \sin\theta / \lambda = 27{,}42;\ 35{,}87;\ 55{,}08$ nm^{-1}. The amorphous films forming in sufficiently wide region of condensation plane at temperature 443 K crystallize with structural characteristics a=0,5483; c= 1,094 nm according with data for hexagonal compound given in [3]

With the to study of $CuGa_5Se_8$ amorphous film crystallization kinetics the isothermal kinematic electron diffraction patterns showing diffraction patterns showing the crystallization process at 413 K, 428 K, 443 K are obtained.

The kinematic electron diffraction pattern, on which the crystallization process of amorphous $CuGa_5Se_8$ at temperature 373 K is registered, is given in fig.1.

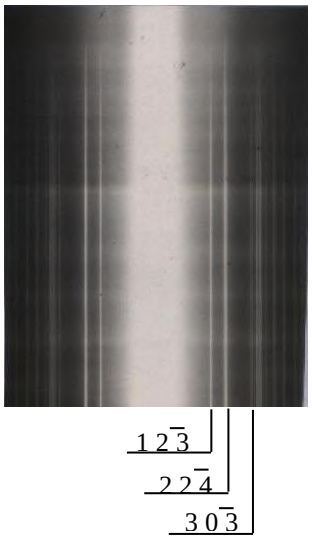

Fig 1. Kinematic electron diffraction pattern form $CuGa_5Se_8$ thin films.

The polycrystalline hexagonal $CuGa_5Se_8$ forms in the crystallization process. The diffuse lines of the amorphous phase of the $CuGa_5Se_8$ film which become "weaker' as result of annealing disappear completely with time, and the intensities of diffraction lines of the hexagonal crystal phase increase.

The lines with $(12\bar{3}0)$, $(22\bar{4}0)$ and $(30\bar{3}0)$ indexes not overlapping with amorphous phase lines and neighboring crystal phase lines that could make mistakes in intensity measurements, are chosen for both photometric definition and intensity electrometric measurement of $CuGa_5Se_8$ hexagonal diffraction lines in dependence on annealing time. The electron diffraction patterns from the polycrystalline $CuGa_5Se_8$ sample were indexed and the formed phases were indentified by comparison of the experimentally observed interplanar distances d_{hkl} with the calculated ones.

The intensity maximal value is compared with one of fully crystallized volume of investigated object for transition of intensity values to quantity of crystallized $CuGa_5Se_8$. The volume fitting on intensity unit is defined by the way finally allows us to find the values of substance crystallized part volume in dependence on annealing time.

We use the following expression:

$$I_{hkl} = I_o \lambda^2 \left| \frac{\Phi_{hkl}}{\Omega} \right|^2 V \frac{d_{hkl} \Delta P}{4\pi L \lambda} \qquad (1)\ [6]$$

where I_o is primary beam intensity, λ is electron beam wave length, Φ is structural factor, Ω is elementary cell volume, V is radiated volume of polycrystalline substance, d_{hkl} is interplanar spacing, Δ is Debye ring small sector, P is multiplicity factor, Lλ is device constant.

Crystallization isotherms of amorphous films shown in Fig. 2 were constructed by normalizing and passing from the intensity values to the volume of the crystallized substance.

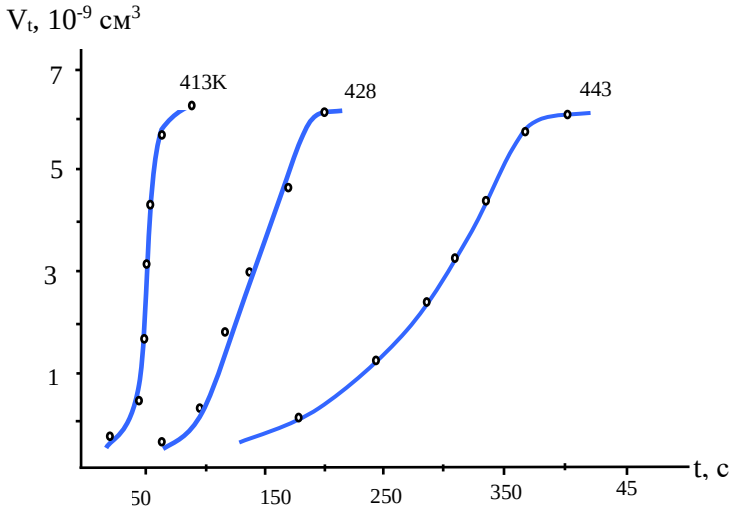

Fig. 2. The kinetic crystallization curves of amorphous $CuGa_5Se_8$

The comparison of isotherm data with following analytical expression

$$V_t = V_o[1-\exp(-kt^m)] \qquad (2)$$

Established by Avrami – Kolmogorov for phase transmation kinetics shows that the best coincidencr takes place at m≈4. The value m=4 shows that in case of crystallization of amorphous $CuGa_5Se_8$ the three-dimensional crystal growth takes place. *lnK* values for 413, 428, 443 K are egual to -17,7; -15,3 and -12,2 correspondingly. *lnK* dependence on reversal temperature for $CuGa_5Se_8$ is linear one.

According to arrhenius equation:

$$\ln K = A - \frac{1}{RT}(E_{gf} + 3E_g) \qquad (3)$$

where E_{gf} and E_g are activation energies of germ-formation and growth correspondingly. The sum value E_{gf}+3 E_g defined by straight line inclination of *lnK* dependence on 1/T, is equal to 125 kcal/mol. The activation energy of germ-formation (E_{gf}), edtablished from dependence $1/\tau_o$ on 1/T, is equal to 27 kcal/mol. The value of growth activation energy, obtained by equality $E_{tot.}$= E_{gf}+3 E_g, is equal to 32,6 kcal/mol. Thus, it is established that at crystallization of amorphous $CuGa_5Se_8$ the values of activation energy necessary for crystallization center formation, i.e. germ-formation and their furter growth have appoximately identical values: 27 kcal/mol and 32,6 kcal/mol, that is very seldom.

CONCLUSION

The phase transformation kinetics in $CuGa_5Se_8$ amorphous films takes place on regularities established by Avrami – Kolmoqorov and is described by analytical experssion $V_t = V_o[1-\exp(-kt^m)]$. At crystallization of $CuGa_5Se_8$ amorphous films, the three – dinensional crystal growth takes place. The activation energies of germ-formation and growth have approximately identical values: 27 kcal/mol and 32,6 kcal/mol.

[1] *A.Ch. Mamedova, D. I. Ismailov.* Journal of Surface İnvestigation, 2016. v.10, No1, pp. 217-220.
[2] *D.I. Ismailov, A. Ch. Mamedova*. Inorg.Mater. 2008. 44, 800.
[3] *L. Duran, S.M. Wasim, C.A. Durante Rincon et al.* Phys.stat.sol. 2003. v.199, № 2, pp. 220-226.
[4] *C. Rincon, S.M. Wasim, G. Marin et al.* Journ. Appl. Phys., 2001. v.90, №9, p. 4423 – 4428.
[5] *K. Ramanathan, M.A. Conreras, C.L. Perkins et al.* Prog.Photovolt.: Res. Appl., 2003. v.11, 225 – 227.
[6] *B.K. Vainshteyn.* Structural Electronoqraphy. 1956.

Received: 02.03.2022

GRAPHENE-BASED CATHODE MATERIALS FOR DYE-SENSITIZED SOLAR CELLS: A REVIEW

B. EMDADI [2], A. ASIMOV [1,2], F. TATARDAR [1,2]

[1] Institute of Physic of Azerbaijan National Academy of Science, AZ-1143, 131, H. Javid ave., Baku, Azerbaijan

[2]Institute of Physics & Electronic of Khazar University (Neftchilar Campus), AZ-1096, Khazar University 41 Mahsati Str., Baku, Azerbaijan

Corresponding author: emdadi.babak2021@khazar.org

In recent years, color-sensitive solar cells (DSSCs) have gained widespread attention for serving as potentially low-cost alternatives to silicon-based solar cells. In DSSCs, platinum-based materials (Pt) used as counter-electrodes (CEs) show superior catalytic ability than triiodide ion reduction reactions, which are attributed to their excellent catalytic activity and high electrical conductivity. However, in order to achieve cost-effective DSSCs, reasonable efforts have been made to discover alternatives without Pt. Recently, a large number of ground-based catalysts, especially carbon-based materials, have shown high activity, low cost, and good stability, making them attractive candidates for platinum replacement in DSSCs. Recently, inexpensive graphene-based counter (CE) electrodes have been developed that could serve as a potential alternative to expensive platinum-based CEs. In this review article, the development of DSSCs and the properties of graphene are briefly described. Then, the application of graphene-based materials for photo electrodes (transparent electrode, semiconductor layer, and color sensitizer) in DSSCs is discussed in depth. Finally, we have a comprehensive perspective on graphene materials in DSSCs is presented.

Keywords: Dye-Sensitized Solar Cells, Ghraphene, Graphene Molecules, Graphene-Carbon Nanotube Components, Solar Cells, Renewable energy.
PACS: 65.80 Ck, 61.48 Gh, 63.37 Hk

1. DYE-SENSITIZED SOLAR CELLS

Energy is one of the very crucial public difficulties which this generation confronts now because we demand energy in each direction of our routine life. Hence, copious several sources of energy, containing fossil, thermic, atomic, hydroelectric, wind, natural gas, and solar [1–5] are used to comply with our increasing plea. Solar energy is one of the excellent concerns because it provides pure energy harvested from the Sun [6]. The increase in energy demand and rising concern for the environment, brought solar cells into the limelight, as it is one of the best sources of sustainable, cleaner, and Renewable energy [7]. The dye-sensitized solar cell can prove itself as a suitable alternative to silicon solar cells. Systems based on intercrossing networks of mesoscopic semiconductors have displayed significantly great transformation efficiencies, which challenge those of conventional devices.

The archetype of this family of devices is the dye-sensitized solar cell, which figures out the optical attraction and the charge segregation processes by the association of a sensitizer as light-absorbing material with a vast bandgap semiconductor of Nano crystalline morphology [8]. Dye-sensitized solar cells (DSSCs) have got up as a technologically and economically reliable alternative to the p-n linkage photovoltaic systems [9]. Meanwhile, DSCs are as well as very economical to the scope that their price-to-performance proportion, which governs the economics of solar cells, exceeds “grid-parity” status. For instance, their value-to-efficiency ratio exceeds that of fossil fuels, which gives them competitive with customary energy technologies [10].

DSSCs are devices that convert solar to electric energy by light sensitization established on wide energy band semiconductors. DSSC shows a very promising future in the field of photovoltaic cells [11]. Dye-sensitized solar cells (DSCs) are typical third-generation photovoltaic devices with a mesoporous architecture and some attractive features, such as cost-effectiveness, environment friendliness, easy processing, and relatively high power conversion efficiency (PCE).

Dye-sensitized solar cells (DSSCs) are one potential alternative to silicon solar cells. DSSCs separate the light absorption and charge transfer processes, unlike Si-based cells. With the expansion of dye-sensitized solar cells (DSCs), 2 conventional solid-state photovoltaic technologies are now challenged by systems functioning at a molecular and Nano level [11]. DSCs suggest the probability of layout solar cells with huge flexibility in shape, hue, and transparency. Integration into diverse products opens up new commercial chances. Besides the exciting possibilities of using DSCs for solar energy application, the riddles of the device are as thrilling [12]. Dye Solar Cells were designed on a large internal interface prepared in a simple laboratory surrounding with no hard requests on the purity of the materials [12]. Dye sensitizer imbibes the incident sunlight and exploits the light vigor to persuade a vectorial electron transition response. Hence, DSSCs have the following privileges compared with Si-based photovoltaic [11].

131, H.Javid ave, AZ-1143, Baku
ANAS, Institute of Physics
E-mail: jophphysics@gmail.com

2. STRUCTURE AND WORKING PRINCIPLES OF DYE-SENSITIZED SOLAR CELLS

Dye-sensitized solar cell (DSSC) is the just solar cell that is able to propose both flexibility and transparency [13]. DSSCs were found to be very helpful, exclusively in the applications of wireless detector networks (clever cities, smart homes, and smart buildings), sports and officinal systems, cameras, safety sensors, and wearable electronics. The structure of DSSCs is comprised of various sheets as compared to the conventional solar cells based on silicon. Each layer of DSSCs has various chemical matters that do a special act in the electricity generation from solar vigor. The fundamental assembly of the ingredients is presented in Fig. 1 [14].

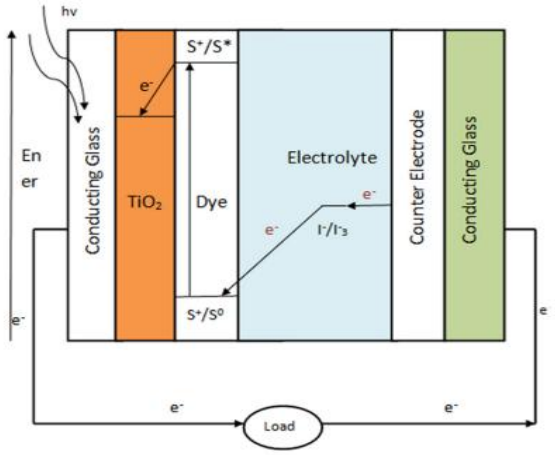

Fig. 1. Adjustment of ingredients and working principle of DSSCs. [9].

A DSSC includes three primary ingredients: the organic dye, the Nano crystalline semiconductor, and the redox couple in the electrolyte [15-22].

DSSC is composed of five elements: two transparent conductive substrates, titanium dioxide layer, dye molecules, electrolyte, and counter electrode (Carbon or Pt). The typical construction of DSSC is shown in Figure 1. The basic operating principle for any solar cell consists of absorption, separation, and collection. Different types optimize these parameters accordingly to attain better efficiency. Thus, absorption occurs in the first step of the reactions occurring in DSSC. The following steps are involved in the conversion of photons into current (as shown in Fig. 2):

1. Firstly, under illumination (photon) is absorbed by a photosensitizer, and thus, due to the photon absorption, electrons get promoted from the ground state (TiO_2/S) to the excited state (TiO_2 /S*) of the dye (Eq. 1).
2. After having been excited (S*) by a photon of light, the dye-usually a transition metal complex whose molecular properties are specifically for the task is able to transfer an electron to the semiconductor (TiO_2) by the injection process (Eq. (II))
3. The injected electron is transported between the TiO_2 nanoparticles and then extracted to a load where the work done is delivered as electrical energy (Equation III).
4. Electrolytes containing I^-/I_3^- redox ions are used as an electron mediator between the TiO2 photoelectrode and the carbon-coated counter electrode. Therefore, the oxidized dye molecules (photosensitizer) are regenerated by receiving electrons from the I^- ion redox mediator that get oxidized to I_3^- (Tri-iodide ions). This process is represented by Eq. 4
5. The I_3^- substitutes the internally donated with that from the external load and reduced back to I^- ion, (Eq. 6) [22]. The movement of electrons in the conduction band of the wide bandgap nanostructured semiconductor is accompanied by the diffusion of charge-compensating captions in the electrolyte layer close to the nanoparticle surface. Therefore, the generation of electric power in DSSC causes no permanent chemical change or transformation.

$$S + h\nu \rightarrow S^*$$
(I) Excitation process

$$S^* + TiO_2 \rightarrow e^-_{(TiO2)} + S^+$$
(II) Injection process

$$e^-_{(TiO2)} + C.E. \rightarrow TiO_2 + e^-_{(C.E)}$$
(III) Energy generation

$$S^+ + (3/2)I^- \rightarrow S + (1/2)I^-$$
(IV) Regeneration of dye

$$(1/2)I_3^- + e^-_{(C.E.)} \rightarrow (3/2)I^- + C.E.$$
(V) e- Recapture reaction

In a DSSC, the sunlight harvesting procedure is accomplished by the photosensitizing dye. It is so significant that the dye has a higher spectral attraction span so that it can attract as much sunlight as probable.

Figure. 3 displays the chemic structures of a few commonly used redox electrolytes, solid-state electrolytes (HTMs), and photosensitizers in the construction of DSSCs.

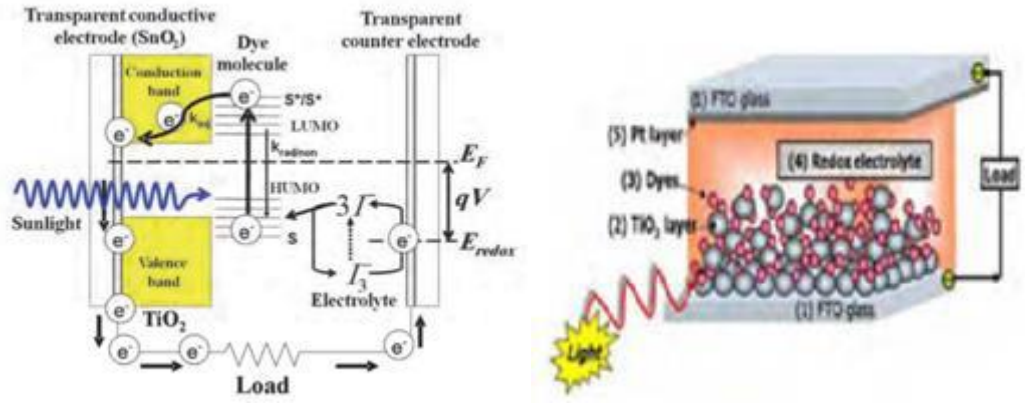

Fig. 2. Typical design of a dye-sensitized solar cell.

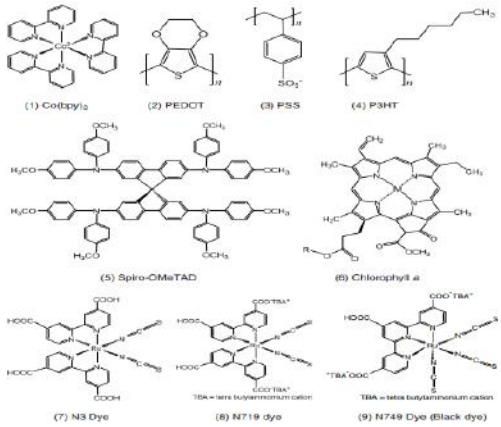

Fig. 3. Chemical structures of a few commonly used redox electrolytes, solid-state electrolytes (HTMs) and photosensitizers.

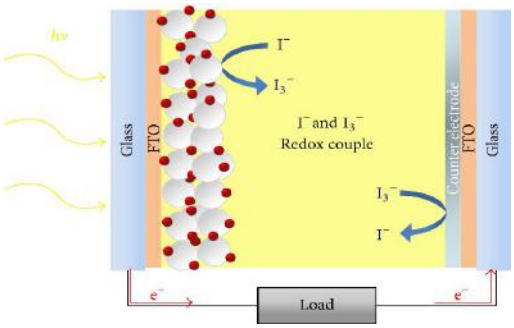

Fig. 4. Schematic illustration of the operation principle of a DSSC.

As displayed in Figure 4, a general DSSC fundamentally includes a nano crystalline semiconductor oxide, a dye sensitizer, an electrolyte redox pair, and a catalyst material as cathode, also named counter electrode (CE) [26].
To obtain high cell performance, the individual ingredients in DSSCs are incumbent to be optimized [27].

3. NEED OF GRAPHENE IN SOLAR INDUSTRY

A crucial origin of materials, critical to energy descendent, are irons found in our earth's scale. Prevalent semiconductor electronic industries are based on silicon tech. Even though these metals ((including platinum (Pt), gallium (Ga), germanium (Ge), selenium (Se), tellurium (Te), gold (Au), chromium (Cr), tungsten (W), and molybdenum (Mo)) are utilized in a very little amount, running and appearing great technology industries can face jeopardizes due to the unacceptable of these critically crucial minerals. Once fossil fuel-based energy resources become used up, high-tech industries and our routine life will be more related to other sources, containing renewable energy sources such as solar energy [6]. The necessities of 11 minerals, containing copper, gallium, indium, lithium, manganese, niobium, some platinum group metals, and some uncommon-earth origins, as assessed by a criticality matrix, are shown in Figure 5 [6].

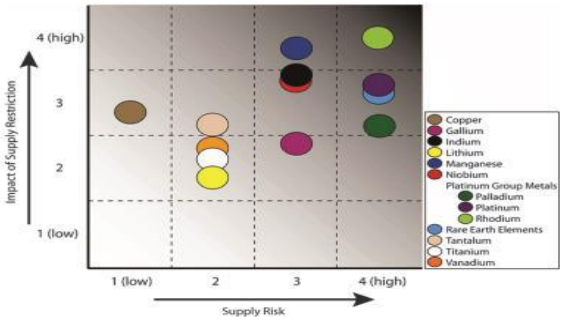

Fig. 5. Criticality assessments for 11 minerals or mineral-based materials.

Between these 11 critical minerals, traditionally used platinum and indium were found to be the most important minerals from the sight of their future accessibility due to likewise factors (some unpredictable) as use up of natural resources, economic and environmental tolerability, and geopolitical concerns. It has become a preference to detect fit low-value organic successors for solar energy industries as well as other appearing future technologies [6].

Alternative crucial metal is platinum, which is although more costly in comparison to gold but is worth for electronic ingredients manufacturing, catalytic technologies, and chemotherapy. In reality, indium and platinum are the main and significant metals currently used in solar energy investigation as electrode materials for dye-sensitized solar cells (DSSCs). Graphene and graphene-based materials suggest the flexibility to create systems over huge districts; Moreover, their low-value generation and low gravity are also absorbing characters for tapping their possible in organic solar cells.

Graphene has appeared as a possible novel material to substitute inorganic semiconductors in solar cell fabrication and hence, has drawn the consideration of the scientific association [6]. Novel materials display a significant duty in processing solar energy technologies. Graphene, one of the allotropes of plentifully exciting carbon, has appeared as one of the main promising materials for benefits in solar cells since its exploration in 2004 [23-25]. Scientists are exploring novel chemical and physical methods to create a feigned band gap in graphene, which is one of the demands for the construction of electronic systems [6]. In as much as graphene is an atom-thick substrate, it is a full-scale nano scale material and, therefore, has excellent potential in a very extensive span of applications in the field of nanotechnology.

Graphene is a 2D carbon-based material having a single layer of carbon atoms; hence, it is an ordinary nanostructured material. Because of this, graphene has been widely studied for nano technological applications in field-effect transistors, solar cells, fuel cells, super capacitors, rechargeable batteries, optical modulators, chemical sensors, medicine delivery, and biomedical applications, in addition to other areas [6]. Graphene has been evaluated as one of the undertaking Pt-free CE alternatives in DSSCs due to its particular attributes of great electrical conductance, perfect electro catalytic activity, supreme anti-corrosion opposition, and larger surface area [28, 29].

This review outlines details from easily accessible research articles on graphene-based DSSCs.

4. CONCLUSION

In this review article, we've tried to give a comprehensive view of Dye-Sensitized Solar Cells, and Structure and Working principles of that. Moreover, we've strived for giving some explanations about graphene in the solar industry, and graphene-Based Cathode Materials. As we've elucidated in this paper, energy is one of the very crucial public difficulties which this generation confronts now because we demand energy in each direction of our routine life. Hence, copious several sources of energy, containing fossil, thermic, atomic, hydroelectric, wind, natural gas, and solar are used to comply with our increasing plea. Solar energy is one of excellent concern because it provides pure energy harvested from the Sun. Last but not least, Novel materials display a significant duty in processing solar energy technologies. Graphene, one of the allotropes of plentifully exciting carbon, has appeared as one of the main promising materials for benefits in solar cells since its exploration, and this material is one of the demands for the construction of electronic systems.

[1] Energy Technology Perspectives 2015, International Energy Agency, Paris, France, 2015.

[2] *C. Philibert.* Solar energy perspectives 2011, Organizations for Economic Co-operation and Development and International Energy Agency, Paris, France 2011.

[3] International Technology Roadmap for Photovoltaic (ITRPV).

[4] *T. Bradford.* Solar Revolution: The Economic Transformation of the Global Energy Industry, MIT Press, Cambridge 2006.

[5] *V. Balzani and N. Armaroli.* Energy for a Sustainable World— From the Oil Age to a Sun-Powered Future, Wiley-VCH, Weinheim 2011.

[6] *Eric Singh, Hari Singh Nalwa.* "Graphene-Based Dye-Sensitized Solar Cells: A Review" Sci. Adv. Mater. 2015, Vol. 7, No. 10

[7] *K.L. Chopra, P.D. Paulson, & V. Dutta.* 2004. Thin-film solar cells: An overview, progress in photovoltaics. Res. Appl., 12, 69–92.

[8] *Michael Grätzel.* "Dye-sensitized solar cells" , Journal of Photochemistry and Photobiology C: Photochemistry Reviews, Volume 4, Issue 2, 2003, Pages 145-153.

[9] *Khushboo Sharma, Vinay Sharma, S.S. Sharma.* "Dye-Sensitized Solar Cells: Fundamentals and Current Status" Nanoscale Research Letters volume 13, 2018, Article number: 381.

[10] *Cole, M. Jacqueline, Pepe, Giulio, Al Bahri, K. Othman, B. Cooper, Christopher.* 2019. Cosensitization in Dye-Sensitized Solar Cells. Chemical Reviews, acs. chemrev.8b00632.

[11] *B. O'Regan, M. Gratzel.* 1991. A Low-cost highefficiency solar cell based on dye-sensitized colloidal TiO_2 films, Nature, 353: 737-740.

[12] *Anders Hagfeldt, Gerrit Boschloo, Licheng Sun, Lars Kloo, and Henrik Pettersson.* "Dye-Sensitized Solar Cells" Chem. Rev. 2010, 110, 6595–6663.

[13] *Di Wei.* "Dye Sensitized Solar Cells", Int. J. Mol. Sci. 2010, 11, 1103-1113.

[14] *Aslam, Asad; Mehmood, Umer; Arshad, Muhammad Hamza; Ishfaq, Abdulrehman; Zaheer, Junaid; Ul Haq Khan, Anwar; Sufyan, Muhammad.* 2020. Dye-sensitized solar cells (DSSCs) as a potential photovoltaic technology for the self-powered internet of things (IoTs) applications. Solar Energy, 207, 874–892.

[15] *M.-E. Ragoussi, T. Torres.* Chem. Commun. 51, 2015, 3957–3972.

[16] *N.S. Lewis, D.G. Nocera.* Proc. Natl. Acad. Sci. U.S.A. 103, 2006. 15729–15735.

[17] *M.A. Green.* Phil. Trans. R. Soc. A 371, 2013, 1–14.

[18] *M.A. Green, K. Emery, Y. Hishikawa, W. Warta, E.D. Dunlop.* Prog. Photovolt: Res. Appl. 21, 2013, 827–837.

[19] *L.M. Peter, Phil.* Trans. R. Soc. A 369, 2011, 1840–1856.

[20] *P.M. Beaujuge, J.M.J. Fréchet.* J. Am. Chem. Soc. 133, 2011, 20009–20029.

[21] *M. Urbani, M. Grätzel, M.K. Nazeeruddin, T. Torres.* Chem. Rev. 114, 2014, 12330–12396.

[22] *M. Grätzel.* Acc. Chem. Res. 42, 2009, 1788–1798.

[23] *K.S. Novoselov, A.K. Geim, S.V. Morozov, D. Jiang, M. I. Katsnelson, I. V. Grigorieva, S. V. Dubonos, and A. A. Firsov.* 2D gas of massless Dirac fermions in graphene. Nature 438, 197–200, 2005.

[24] *A.K. Geim and K. S. Novoselov.* The rise of graphene. Nature Mater. 6, 183–191, 2007.

[25] A.K. Geim. Graphene: Status and prospects. Science 324, 2009. 1530–1534.

[26] *Man-Ning Lu, Chin-Yu Chang,Tzu-Chien Wei, Jeng-Yu Lin.* "Recent Development of Graphene-Based Cathode Materials for Dye-Sensitized Solar Cells" Volume 2016, |Article ID 4742724.

[27] *G. Calogero, A. Bartolotta, G. Di Marco, A. Di Carlo, and F. Bonaccorso.* "Vegetable-based dye-sensitized solar cells," Chemical Society Reviews, vol. 44, no. 10, pp. 3244–3294, 2015.

[28] *J.D. Roy-Mayhew, D.J. Bozym, C. Punckt, and I.A. Aksay.* "Functionalized graphene as a catalytic counter electrode in dye-sensitized solar cells," ACS Nano, vol. 4, no. 10, pp. 6203–6211, 2010.

[29] *D.W. Zhang, X.D. Li, H.B. Li* et al., "Graphene-based counter electrode for dye-sensitized solar cells," Carbon 2011, vol. 49, No. 15, pp. 5382–5388.

Received:11.03.2022

RED - YELLOW - RED REVERSIBLE SHIFT OF PHOTOLUMINESCENCE MAXIMUM IN STAIN ETCHED POROUS SILICON AT DILUTE HF POSTTREATMENT

F.A. RUSTAMOV, N.H. DARVISHOV, V.E. BAGIEV, M.Z. MAMEDOV, E.Y. BOBROVA, H.O. QAFAROVA

Condensed Matter Physics Division, Institute for Physical Problems, Baku State University, Baku AZ 1148, Azerbaijan

E-mail: farhad.rustamov@bsu.edu.az

The effect of posttreatment in a diluted HF solution on the photoluminescence spectra of stain etched porous silicon has been investigated. It is shown that this posttreatment of as–prepared samples leads to a shift of the photoluminescence maximum from ~1.85*eV* to ~2.1*eV*. For posttreatment times less than 15min, subsequent atmospheric oxidation displaces the photoluminescence maximum again to 1.85*eV*, exhibiting a full red–yellow–red cycle. For posttreatment times more than 15min, subsequent atmospheric oxidation leads to photoluminescence quenching. The role of oxygen bonds in the observed phenomena is discussed.

Keywords: porous silicon; stain etching; posttreatment; diluted *HF*; yellow *PL*; oxygen bonds.
PACS: 81.40.−z; 78.67. Rb; 78.55.−m. doi:

1. INTRODUCTION

Since the discovery of the phenomenon of visible photoluminescence (*PL*) in porous silicon (*PS*), there has always been a question of tuning the position of its maximum [1, 2]. It would seem that the very reason that porous silicon, in contrast to bulk silicon, produces visible *PL* suggest such tuning method. Indeed, it is the phenomenon of quantum confinement that assumes the broadening of the bandgap of silicon nanocrystallites with a decrease in their size [1, 3–5]. Therefore, reducing the size of nanocrystallites during formation or postetching after formation, it is possible to increase the bandgap of nanocrystallites. However, in the experimental implementation of these methods, it turned out that in practice there is no significant shift of the PL maximum, despite the possible broadening of the bandgap [1, 4, 6, 7].

It is known that the position of the *PL* maximum and the size of silicon nanocrystallites during the electrochemical etching method depends on the type and value of the substrate conductivity, the composition of the solution, the current value, the duration of etching and illumination. In stain etching method, the *PL* peak position depends on the type and value of conductivity of the substrate, the composition of solution and the etching duration. But changing these etching conditions, affecting the intensity of the radiation, only leads to a slight shift of the *PL* peak position all *PS* samples obtained by conventional electrochemical or stain etching method and not subjected to additional postetching, regardless of their porosity, exhibit red or red-orange luminescence in air. The explanation for this fact lies in the oxidation of nanocrystallites, a theoretical basis is given in the works [3, 4]. In this work, it was theoretically shown that when hydrogen bonds Si – H are replaced by oxygen bonds Si–O, local levels appear in the *PS* bandgap. It is the appearance of these radiative register such a displacement, PS samples were kept and investigated in an argon atmosphere to prevent their recombination levels that leads to red-orange photoluminescence regardless of the porosity and size of silicon nanocrystallites.

Oxygen bonds in the *PS* may occur at various stage of formation, according to the method of preparation. In the electrochemical etching method, the surface of as-prepared *PS* is covered with hydrogen bonds and they are replaced by oxygen bonds during subsequent exposure of the samples in air [8-10]. This oxidation, and hence the appearance of local radiation levels, occurs very quickly, during the first minutes of expose in air. Depending on the porosity of the samples, the existence of these levels manifests itself in different ways. As long as porosity of *PS* is low, the oxidation of nanocrystallites does not lead to the appearance of local levels in the bandgap, band-to-band transitions with red *PL* prevail. With an increase in porosity and a decrease in the size of Si nanocrystallites, the *PL* maximum shifts slightly to the high energy (orange) region. But if the porosity is high and the sizes of nanocrystallites are small (~2nm), then this oxidation leads to the appearance of local levels of radiative recombination in the bandgap of *PS*. In this case, radiative recombination proceeds through these local levels, band-to-band transitions are not relevant, and such *PS* samples exhibit red-orange or orange photoluminescence. In this case, with an increase in porosity and a decrease in the size of nanocrystallites, the further shift to the high energy region is very insignificant [6, 7, 11].

For *PS* samples obtained by electrochemical etching, there are two possible ways of tuning the position of the PL maximum to the high energy region. In low porosity *PS*, regardless of the presence or absence of oxygen bands, postetching is required to reduce the size of nanocrystallites. And this is not a very convenient way. In works [1,4,12,13], such additional etching was carried out in hydrofluoric (*HF*) solutions with mandatory illumination for ~1 hour. In this case, the *PL* maximum shifted to the blue zone. To oxidation. When the sample was exposed to air, the *PL* maximum very quickly (1÷3min) shifted back to the

131, H.Javid ave, AZ-1143, Baku
ANAS, Institute of Physics
E-mail: jophphysics@gmail.com

red–orange region. Investigation of the *FTIR* spectra showed the correlation of this shift with the appearance of oxygen bonds when the samples were exposed to air. However, in highly porous samples with silicon nanocrystallites of about 2*nm* in size, additional postetching to reduce the size of nanocrystallites is not required. In this case, it is sufficient to remove the oxide layer, i.e. remove oxygen bonds which create local levels in the bandgap. Then the *PL* maximum should shift to the high–energy region. Unfortunately, such works are not found in the literature, which is apparently associated with the difficulty of obtaining highly porous *PS* samples by electrochemical etching without additional postetching.

In porous silicon obtained by chemical etching, the situation is somewhat different. These *PS* samples are usually highly porous, and oxygen bonds in them are formed already in the working solution [14-17], i.e. in the process of formation of porous silicon. That is, for the appearance of Si–O bonds and occurrence of radiative recombination local levels in the bandgap, atmospheric oxidation is not required. As a consequence, instead of the band-to-band transitions, transitions through these local levels immediately prevail here. Therefore, stain etched porous silicon, regardless of the porosity, immediately after preparation exibits red – orange or orange *PL*. To shift the *PL* maximum in these PS samples, it is necessary to remove these oxygen bonds. As is known, oxygen bonds on the silicon surface are very easily and quickly removed with dilute 10% aqueous *HF* solution. But the effect of an aqueous *HF* solution, depending on the etching time, leads to both the removal of oxygen bonds and a further decrease in the size of silicon nanocrystallites. Therefore, the final result of the effect of posttreatment on *PL* requires further experimental research. In this work, we studied the effect of stain etched porous silicon posttreatment in a diluted aqueous – alcoholic *HF* solution on the *PL* spectra.

2. EXPERIMENT

Porous silicon samples were obtained by stain etching on monocrystalline silicon substrates of p- type polished on both sides, with a resistivity of 0.1*Om·cm* and (111) orientation. To remove contaminant and degrease the surface, the plates were immersed in acetone for 50 min and then washed with bidistilled water. Then, to remove the oxide layer, the surface of the plates was treated in a 10% aqueous HF solution for 1min, and then in concentrated HF for 5min. The formation of PS layers was carried out at room temperature and daylight illumination in a HF(50%):HNO_3(65%):CH_3COOH(glacial) modified solution in volume proportion 1200:1:800, i.e. at oxidant insufficiency [18]. After the incubation time, the reaction of PS formation lasted 9 minutes. Such samples have a porosity of more than 70%, with crystallites size of 1.5÷2.8*nm* [16, 19, 20] (fig.1).

Some of the samples immediately after the formation of PS layers were washed in bidistilled water, then in isopropyl alcohol, and thereafter posttreated with a mixture of isopropyl alcohol and 10% aqueous HF solution (in a volume ratio 1:1) during 1÷60min. An alcoholic solution was used to increase the wettability of porous silicon. In all these procedures, it is important to prevent premature contact of the PC with atmospheric air. Then the samples were washed in bidistilled water, isopropyl alcohol and dried by N_2 jet. Immediately after drying, the *PL* spectra of the obtained samples were studied under ambient atmospheric conditions.

The PL spectra have been investigated under room temperature. The PL was excited by Xenon lamp *DKSL*-1000, passed through an *SPM-2* monochromator and was recorded with an IKS-12 monochromator in the reflection geometry. In *PL* measurements, the excitation wavelength was 320nm.

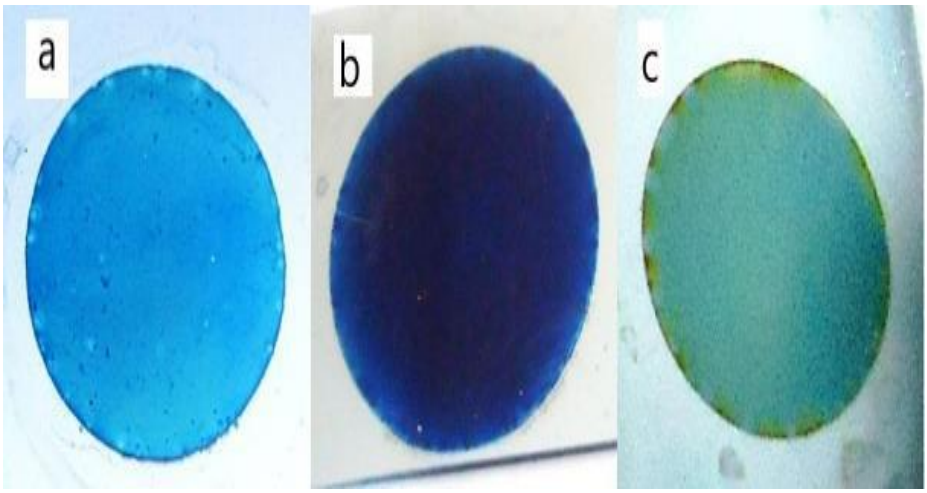

Fig.1. Stain etched *PS* layers formed in HF:HNO_3:CH_3COOH solutions for a) 1.5min, b) 9min and c) 45min.

3. RESULTS

Fig.2 shows the photoluminescence spectra of stain etched PS samples both immediately after formation (*a*) and of *PS* samples immediately after posttreatment in an alcohol solution of 10% *HF* (*b*) at room temperature. As can be seen from the figure, these spectra are a strikingly different from each other.

The samples that have not undergone additional treatment exhibit red photoluminescence with a peak at ~1.85*eV*, and this maximum hardly shifts upon exposure to air (fig.2a). This is a common *PL* spectrum observed in relatively highly porous *PS* samples obtained by conventional electrochemical or stain etching methods without posttreatment. Those samples that were subjected to posttreatment in an alcohol solution of 10% *HF* for 1÷15min immediately after formation exhibit yellow photoluminescence with a maximum at 2.1*eV* (fig.2b). If the posttreatment of the samples was carried out for less than 15min, then upon contact the air their *PL* spectrum is transformed very quickly (2÷3min) and the maximum shifts back to 1.85*eV* (fig.2 *b-c* transition). In this case, the *PL* spectra of untreated samples and samples posttreated in an alcohol solution of 10% *HF* and exposed in air for more than 5min practically coincide. Further exposure in air leads to a slight increase in the *PL* intensity without shifting its maximum (fig.2. *c-d* transition). If posttreatment in an alcohol solution of 10%*HF* lasts more than ~15min, the situation (PL behavior) changes somewhat. In this case, immediately after posttreatment, the samples also exhibit yellow *PL* with a peak at 2.1*eV*. But then, when exposed to air their *PL* is no longer shifted to the red region, and very quickly (1÷2min) irreversibly quenched (fig.2 *b-e* transition).

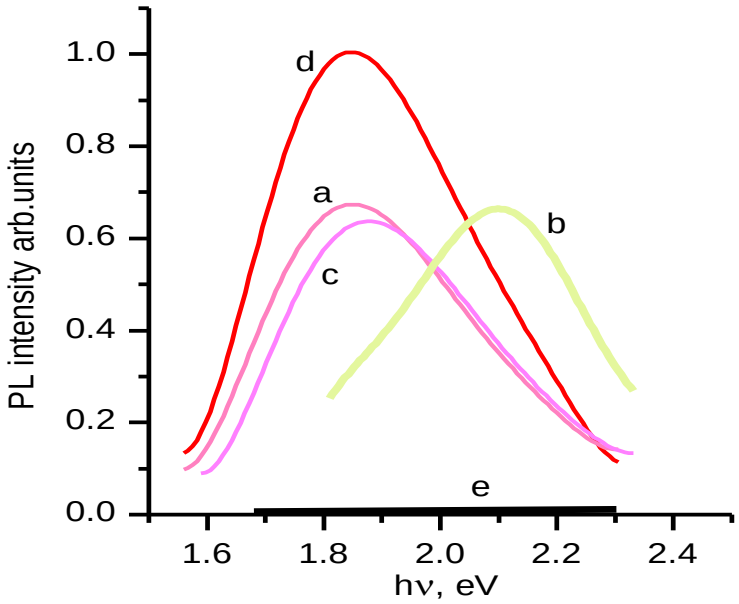

Fig.2. a) as-prepared PS without postetching; b) as-prepared *PS* postetched in dilute HF; c) postetched (< 15min) *PS* after 2min expose in air; d) postetched (< 15 min) *PS* after 5min expose in air; e) PL quenching of postetched (> 15min) *PS* after 2min expose in air.

4. DISCUSSION

In fig.2a can be seen that porous silicon, immediately after formation by the chemical etching method, exhibits a red – orange (1.85*eV*) *PL* despite its high porosity. The position of this maximum is fairly stable and almost does not change at further atmospheric oxidation. Such stability of the *PL* spectra of stain etched *PS* distinguishes it from *PS* obtained by electrochemical etching [17, 21, 22]. Our earlier studies of the *FTIR* spectra [17] of such *PS* samples show that this fact is associated with the oxidation of silicon nanocrystallites (the band of 1108cm^{-1} corresponding to Si-O-Si asymmetric stretching of interstitial oxygen in Si and absorption peaks at 882cm^{-1} and 224cm^{-1} corresponding to O_3–Si–H bending and stretching mode) already during the formation of *PS* in the etching solution (fig.3).

This fact distinguishes stain etched *PS* from samples obtained by electrochemical etching. That is, in these samples, local radiative recombination levels located in the bandgap and associated with Si-O bonds arise in the process of PS formation. Therefore, in spite of their high porosity and small size of silicon crystallites (1.8÷2.3*nm*) [19, 20] these samples immediately after formation exhibit only red–orange *PL*.

As expected, the posttreatment of samples in a dilute *HF* solution immediately after formation led to significant shift of the *PL* maximum from 1.85*eV* to 2.1*eV* (fig.1, *a-b* transition). It is known that a dilute aqueous solution of *HF* very quickly removes the oxide layer on the silicon surface, what is widely used in silicon technology.

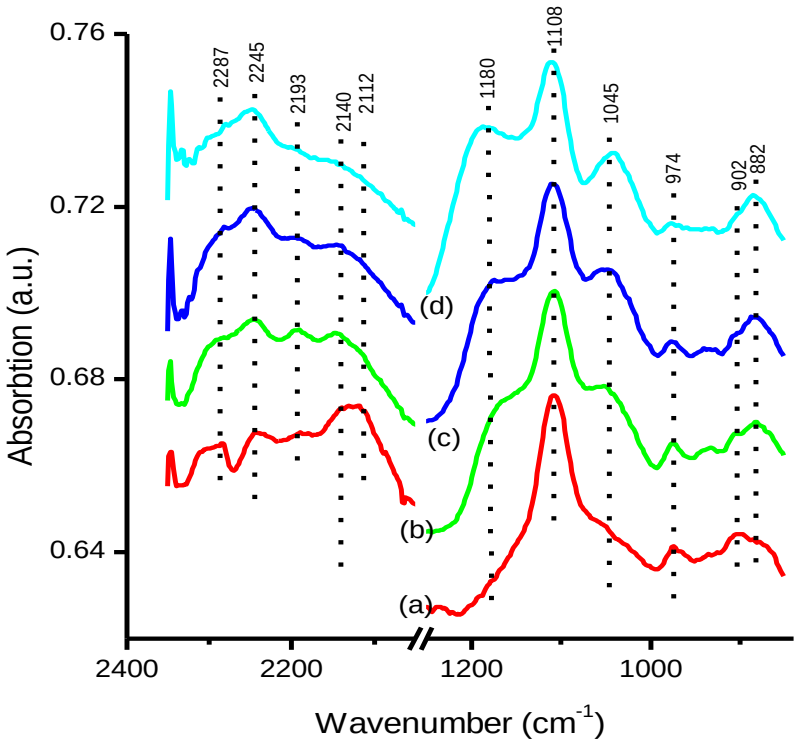

Fig.3. FTIR spectra of stain etched *PS* upon exposure to air: a) as-prepared, b) after 1 day, c) after 7 day, d) after 3 month.

In our case, such a treatment of the samples, by removing the Si–O bands, also leads to the removal of the local radiative levels associated with these bonds located in the bandgap of silicon nanocrystallites. Thus, the discrepancy between the small sizes of silicon crystallites and the position of the *PL* maximum is really associated with oxygen bonds, which in our case are formed during the formation of *PS*, namely, in the etching solution. But it should be noted that such a displacement can be detected only immediately after postetching *PS* in dilute *HF*, i.e. it is in freshly prepared samples, until it is affected by atmospheric oxidation.

Due to the high oxidizing ability of silicon, the situation changes after several minutes of exposure to atmospheric air. Depending on the posttreatment time in the HF solution, two radically different variants are observed. If the treatment time in the solution of HF is less than 15 minutes, then the *PL* maximum is reversed to the low energy region ~1.8*eV* again (fig.2, *b–c* transition), i.e. the *PL* spectrum, which was observed before treatment in *HF* solution, is restored. This indicates the fact that when the treated samples are exposure in atmospheric air, silicon nanocrystallites are re –oxidized, which means that radiative recombination levels are again formed in the bandgap, leading to the observed shift of the *PL* peak. In terms of *PL* manifestation, a full cycle is formed: red–yellow– red. This once again prove the decisive role of Si –O bonds in the photoluminescence phenomenon manifested by silicon nanocrystallites in highly porous samples. On the other hand, this indicates that the posttreatment of freshly prepared *PS* samples in a dilute *HF* solution for less than 15min leads only to the removal of the oxide layer without changing the average size of Si nanocrystallites. With further exposure to air, a certain increase in the PL intensity occurs at unchanged maximum position (fig.2, *c–d* transition). Such an increase in intensity is associated with additional oxidation of silicon particles in air (fig.3) (absorption peak at 1180cm^{-1} and 1045cm^{-1}, corresponding to Si–O–Si stretching *LO* and *TO* modes), resulting in better compensation for dangling bonds on the surface [17].

If the posttreatment time in diluted HF solution exceeds 15min, then, as in the previous case, yellow *PL* is first observed, but then exposure to air leads to the quenching of the visible *PL* (fig.2, *b–e* transition). In this case, the *PL* intensity during 2÷3min drops to zero. Of course, this should also be connected with the oxidation of silicon nanocrystallites in atmospheric air. With an increase in the posttreatment time of freshly prepared *PS* samples in a dilute *HF* solution, not only the removal of the oxide layer occurs. Most likely, due to the long treatment time in *HF*, chemical etching of the nanocrystallites themselves begins to affect. In this case, the sizes of the crystallites are critically reduced. When such samples are exposure in air, their oxidation also occurs, but in this case, it is fully. This complete oxidation leads to the transformation of Si nanocrystallites into silicon oxide, and their ability to photoluminescence disappears.

5. CONCLUSION

The effect of posttreatment in a dilute aqueous *HF* solution on the photoluminescence of stain etched porous silicon has been investigated. The *PS* samples were obtained on the Si wafers by stain etching in a HF:HNO3:CH3COOH solution. Immediately after

formation, all PS samples exhibited red *PL* (~1.85*eV*) associated with oxygen bonds formed directly in the etching solution during formation. All samples were subjected to posttreatment in a dilute *HF* solution for various time. It was revealed that such posttreatment of the investigated samples always leads to a shift in the maximum of their *PL* from the red (~1.85) to the yellow (~ 2.1e*V*). This shift is associated with the removal of oxide layers on the surface of Si nanocrystallites, which led to the formation of radiative recombination levels in the bandgap and was the cause of the red *PL* regardless of the size of the nanocrystallites. When exposed to air, due to atmospheric oxidation, the *PL* spectra transformed within 2÷3min. If posttreatment time was less than 15min, then the *PL* maximum shifted again to the red region, completing the red–yellow–red cycle. This shift is associated with the repeated formation of oxygen bonds on the surface of nanocrystallites. If the posttreatment time was more than 15min, then the yellow *PL* was extinguished. This is due to the fact that, at long postetching times in *HF* solutions, etching of the silicon crystallites themselves begins to affect. In this case, the size of the nanocrystallites decreases critically, and when they are exposed in air, they are completely oxidized, transforming into silicon oxide, and the ability to *PL* disappears.

[1] *L.T. Chanham.* Silicon quantum wire array fabrication by electrochemical and chemical dissolution of wafer, Appl. Phys. Lett. 1990, 57, pp. 1046-1048. https://doi.org/10.1063/1.103561

[2] *V. Lehmann, U. Gosele*. Porous silicon formation: A quantum wire effect, Appl. Phys. Lett. 1991, 58, pp. 856-858. https://doi.org/10.1063/1.104512

[3] *C. Delerue, G. Allan, M. Lannoo.* Theoretical aspects of the luminescence of porous silicon, Phys. Rev. 1993, B 48, 15, pp.11024-11036. https://doi.org/10.1103/PhysRevB.48.11024

[4] *M.V. Wolkin, J. Jorne, P.M. Fauchet, G. Allan, C. Delerue.* Electronic States and Luminescence in Porous Silicon Quantum Dots: The Role of Oxygen, Phys. Rev. Lett. 1999, 82, 1, pp. 197-200. https://doi.org/10.1103/PhysRevLett.82.197

[5] *Md. N. Islam, Satyendra Kumar*. Influence of surface states on the photoluminescence from silicon nanostructures, J. Appl. Phys. 2003, 93, 3, pp. 1753-1759. https://doi.org/10.1063/1.1535254

[6] *V. Lehmann*. Electrochemistry of Silicon. Willey VCH, New York, 2002.

[7] *L.T. Chanham.* Properties of porous silicon. EMIS Data Review Series No. 18, London, 1997.

[8] *E. Kayahan.* The role of surface oxidation on luminescence degradation of porous silicon, Appl. Surf. Sci. 2011, 257(9) , pp. 4311-4316. https://doi.org/10.1016/j.apsusc.2010.12.045

[9] *N. Arad-Vosk, A. Sa'ar*. Radiative and nonradiative relaxation phenomena in hydrogen- and oxygen-terminated porous silicon, Nanoscale Research Letters. 2014, 9, 47, pp. 1-6. https://doi.org/10.1186/1556-276X-9-47

[10] *E. Galeazzo, A. Beltran, F. J. Ramirez-Fernandez.* Natural Oxidation of Porous Silicon, Brazilian Journal of Physics, 1997, 27/ A, 4, pp. 170-172.

[11] *S.M. Hossain, S. Chakraborty, S.K. Dutta, J. Das, H. Saha*. Stability in photoluminescence of porous silicon, J. Lumin. 2000, 91, pp.195-202.https://doi.org/10.1016/S0022-2313(00)00225-8

[12] *H. Koyama, N. Koshida*. Photo-assisted tuning of luminescence from porous silicon. J. Appl. Phys. 1993, 74, pp. 6365-6367. https://doi.org/10.1063/1.355160

[13] *B. Bessais, H. Ezzaouia, H. Elhouichet, M. Oueslati, R. Bennaceur*. Correlation of photoluminescence spectra and structure of porous silicon. Semicond. Sci. Technol. 1996, 11, pp. 1815–1820.

[14] *Y.Q. Jia, L.Z. Zhang, J.S. Fu, B.R. Zhang, J.C. Mao.* Characterization of stain etched porous Si with photoluminescence, electron paramagnetic resonance, and infrared absorption spectroscopy, J. Appl. Phys. 1993, 74 (12), pp. 7615-7617. https://doi.org/10.1063/1.354940

[15] *É. Vázsonyi, E. Szilágyi, P. Petrik, Z. Horvath, T. Lohner, M. Fried, G. Jalsovszky.* Porous silicon formation by stain etching, Thin Solid Films. 2001, 388, pp. 295-302. https://doi.org/10.1016/S0040-6090(00)01816-2

[16] *B. González-Díaz, R. Guerrero-Lemus, J. Méndez-Ramos, B. Díaz-Herreraa, V.D. Rodríguez*. Gradual oxidation of stain etched porous silicon nanostructures applied to silicon-based solar cells. Sens. Actuators. 2009, A 150, pp. 97–101. https://doi.org/10.1016/j.sna.2008.12.006

[17] *F.A. Rustamov, N.H. Darvishov, V.E. Bagiev, M.Z. Mamedov, G.M. Eyvazova, E.Y. Bobrova, H.O. Qafarova.* Reversible quenching of photoluminescence in stain etched porous silicon at HNO_3 posttreatment and role of oxygen bonds. J. Lumin. 2018,195, pp. 49-53. https://doi.org/10.1016/j.jlumin.2017.11.011

[18] *F.A. Rustamov, N.H. Darvishov, M.Z. Mamedov, E.Y. Bobrova, H.O. Qafarova*. Formation of lateral homogeneous stain etched porous silicon with acetic acid at oxidant insufficiency, Azerb. J. Physics. 2012, 18, 3, pp. 44-49. http://inis.iaea.org/search/search.aspx?orig_q=RN:44023241

[19] *F.A. Rustamov, N.H. Darvishov, V.E. Bagiev, M.Z. Mamedov, E.Y. Bobrova, H.O. Qafarova*. Determination of size and bandgap distributions of Si nanoparticles from photoluminescence excitation and emission spectra in n-type stain etched porous silicon, J. Lumin., 2014, 154, pp. 2024-2028. https://doi.org/10.1016/j.jlumin.2014.04.037

[20] *G. Di. Francia, A. Citarella.* Kinetic of the growth of chemically etched porous silicon. J. Appl. Phys. 1995, 77 (7), pp. 3549–3552. https://doi.org/10.1063/1.358585

[21] *M.J. Winton, S.D. Russell, J.A. Wolk, R. Gronsky.* Processing independent photoluminescence response of chemically etched porous silicon, Appl. Phys. Lett. 1996, 69, pp. 4026-4028. https://doi.org/10.1063/1.117859

[22] *M. Nahidi, K.U. Kolasinski*. Effects of stain etchant composition on the photoluminescence and morphology of porous silicon, J. Electrochem. Soc. 2006,153, 1, pp. C19-C26. https://doi.org/10.1149/1.2129558

Received: 04.04.2022

THEORETICAL STUDY OF ELECTRONIC PROPERTIES OF Ag_2Te

R.A. HASANOVA
Institute of Physics of Azebaijan NAS
H. Javid ave 131, Baku, AZ-1143

The electronic band structure and density of state calculations were performed for the low-temperature modification of a silver chalcogenide - β-Ag_2Te through Atomistic Simulation Software Quantum ATK. The structures are characterized by three, four and five coordinations of silver by the chalcogen. According to the band structure calculations, β-Ag_2Te is semiconductor with an about 0.1–0.2 eV forbidden zone. The calculations have shown that β-Ag_2Te has a very low DOS in the energy range from about –0.1 to +0.5 eV.

Keywords: electronic band structure, chalcogenide, density of state, silver, semiconductor.
PACS: 72.25.Pa; 71.23.An

INTRODUCTION

Ag_2Te, one of silver chalcogenides, is known as Hessite mineral in nature. It was used as ionic conductor at high temperature phase. The zone structure of Ag_2Te was studied through local spherical wave (LSW) mathod. In accordance with the LSW calculation of the zone structure, this compound is semi-metallic having approximately $0,1 \div 0,2eV$ energy cover (forbidden zone). It undergoes a phase transition below $417K$ into the phase, a narrow gap semiconductor, where the ion migration is frozen and the compound is nonmagnetic. Ag_2Te changes from a regular structure to a chaotic structure at low temperatures. The transition temperature of Ag_2Te is $1450°C$. The gap of β-Ag_2Te is in the range of several tens *meV*, the mobility of carriers is high and the effective mass is of the order of 102 m_0 (m_0 is the free electron mass) [1, 2].

It is known that the low-temperature (β) phases for Ag_2Te has large and positive magneto-resistance. This compound is non-magnetic. In order to understand the origin of magneto-resistance, it is important to have profound knowledge about its electronic structure.

The Ag chalcogenides are of great importance first of all due to the high ionic conductivity (of Ag+) of the high temperature (α) structure and electronic conductivity. The high ionic conductivity in the α phase of the Ag_2Te is due to the static distribution of silver atoms in the lattice. These compounds show a transition at rather low temperatures from the β structure to α structure. The transition temperature is $139°C$ for Ag_2Se and 145°C for Ag_2Te [3].

The electrical transport properties of Ag_2Te have been extensively studied and reported [4-7]. In these studies, a very small temperature range is studied and the phase transition environment is studied. According to the results of the band structure calculations it is small gap (20-50 meV) semiconductor. The deviation from stoichiometry determines both the electronic conductivity and activation energy. The mobility of electrons and holes is high with small effective mass. Concentration of electron - carriers is about $3 \times 10^{18} cm^{-3}$. Earlier, the lattice parameters of β-Ag_2Te were calculated by Van der Lee, A. and J.L. de Boer. Lattice parameters and coordinates of β-Ag_2Te are from an accurate single crystal refinement by the mentioned researchers [7].

RESULTS

In this article the electronic band structure and density of state were calculated for β-Ag_2Te using the Atomistic Simulation Software Quantum ATK method [8].

Figure 1 shows the atomic structure of β-Ag_2Te. As it can be seen from the figure, the extraordinary superconducting properties of β-Ag_2Te is associated with these linear chains of Ag atoms.

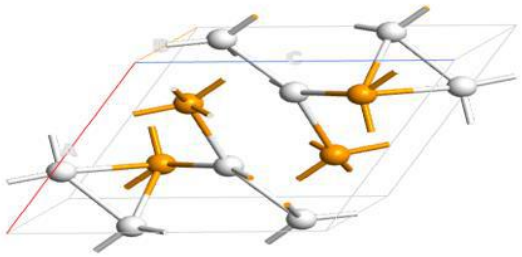

Fig. 1. Atomic structure of β -Ag_2Te.

Besides the metal–chalcogen distances corresponding to bonding, there are also metal-metal-distances as in pure metals. Table 1 presents the interatomic distances for β-Ag_2Te. β -Ag_2Te has two types of silver atoms in its structure. Both types of Ag atoms have a four-fold coordination by Te atoms. The Ag-Ag distances range from 2.84 to 3.13 Å. The chalcogen packing is distorted face-cantered cubic.

The band structure of β-Ag_2Te plotted for high symmetry points Γ-X- M-Γ-R-X at T=300K is given in figure 2. The band structure calculated based on density functional theory within spin-polarized PBE-GGA approximation.

Figure 3 presents some calculated results of the density of state (DOS) constructed for *s*-, *p*- and *d*-electrons of β-Ag_2Te.

131, H.Javid ave, AZ-1143, Baku
ANAS, Institute of Physics
E-mail: jophphysics@gmail.com

Table 1.

Interatomic distances between atoms in β-Ag_2Te crystal ($\AA$)

Ag(1)-Te	2.877	2.895	2.965	3.016
Ag(2)-Te	2.842	2.905	3.011	3.034
Ag(1)- Ag(1)	2.841	3.010	-	-
Ag(2)- Ag(2)	3.053	-	-	-
Ag(1)- Ag(2)	3.061	3.133	2.909	

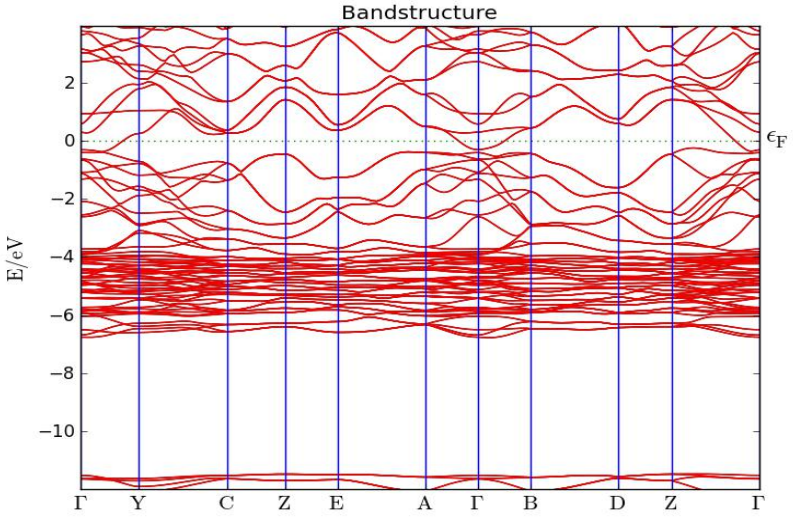

Fig. 2. Electronic band structure of β-Ag_2Te.

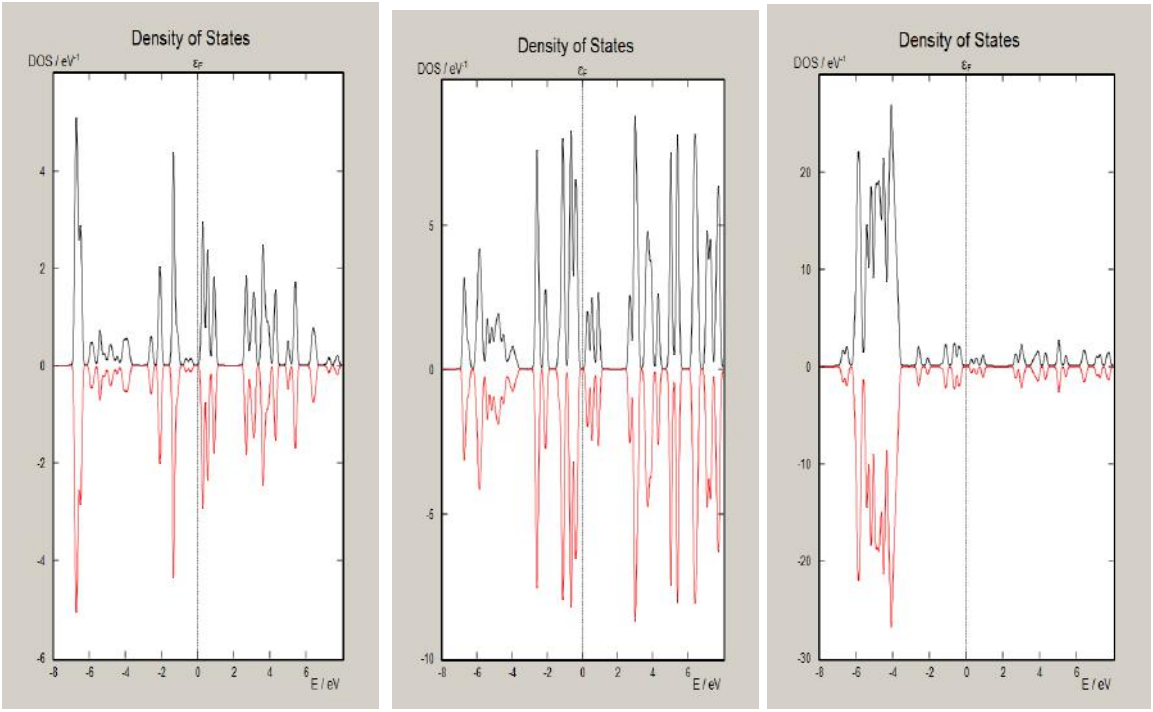

a b c

Fig. 3. DOS for *s- (a); p-(b)* and d-(c) electrons of β-Ag_2Te.

CONCLUSION

The electronic band structure and density of state were calculated for low temperature β-Ag_2Te using the Atomistic Simulation Software Quantum *ATK* method It was found that the extraordinary superconducting properties of β-Ag_2Te is associated with the linear chains of Ag atoms. There is a small overlap between the conduction and valence band of β-Ag_2Te. In addition, DOS was calculated for *s- (a); p-(b)* and d-(c) electrons of β-Ag_2Te.

Based on the calculations, we can say that β-Ag_2Te have a very low *DOS* in the energy range from about –0.1 to +0.5*eV*.

[1] *W. Zhang, R. Yu, W. Feng* et al. Topological aspect and quantum magnetoresistence of β- Ag_2Te. Physical Review Letters., 2011, 106, № 4, pp. 156808 (1-4).

[2] *C.Z. Gottlieb, W. Kane, F.A. Walsch et al*. Electrical properties of Ag_2Te-I. Phys.an Chem. Sol., 1960, №107, pp.977-982.

[3] *C.M. Fang, R.A. De Groot, G.A. Wiegers.* Ab initio band structure calculations of the low-temperature phases of Ag_2Se, Ag_2Te and Ag_3AuSe_2. Journal of Physics and Chemistry of Solids., 2002, № 63, pp. 457-464.

[4] *V. Vassilev, V. Vachkov, S. Parvanov*. On one possibility of application of new thermoelectric materials based on Ag_2Te. Transactions of Faculty of Mathematics and Natural Sciences, section: Chemistry., 2011, pp.147-154.

[5] *L. Dong, A. Wang, E. Li et al.* Formation of two-dimensional AgTe monolayer atomic crystal Ag (111) substrate. Chin. Phys. Lett., 2019, vol.36, №2, pp. 028102 (1-3).

[6] *D. Yung, K. Kurosaki,Y. Ohishi et al.* Effect of phase transition on the thermoelectric properties of Ag_2Te. Materials Transactions., 2012, vol.53, №7, pp. 1216-1219.

[7] *Van der Lee, A. and J.L. de Boer*. Redetermination of the structure of hessite, Ag2Te-III. Acta Crystallographica, 1959, vol. 49, pp. 1444-1446.

[8] *S.O. Mammadova*. Electronic and magnetic properties of A15 and $D8_m$ phase Ti_3Sb. Proceedings of 7th International Conference MTP-2021: Modern Trends in Physics, pp. 23-30.

Received: 05.04.2022

NONSTATIONARY SUM FREQUENCY GENERATION IN INHOMOGENEOUS OPTICAL FIBER

RENA J. KASUMOVA[1], Sh.Sh. AMIROV[1,2,3*]
[1]*Physics department, Baku State University, 23 Z. Khalilov str., Az-1148, Baku, Azerbaijan*
renajkasumova@gmail.com
[2]*Department of Medical and Biological Physics, Azerbaijan Medical University, A. Gasimzade str., 14, AZ 1022, Baku, Azerbaijan*
[3]*Department of Physics and Electronics, Khazar University, 41 Mahsati str., Az 1096 Baku, Azerbaijan*
[*]*Corresponding author e-mail:* phys_med@mail.ru

An effect of inhomogeneuity of refractive index in optical fiber on the sum frequency generation in analyzed in the constant intensity approximation*(CIA*). It was revealed effect of regular inhomogeneity of medium on the character of nonlinear process at various values of pump intensity as well as medium losses. The influence of inhomogeneity of medium on the duration of sum frequency pulse for the Gaussian shape of pump wave pulse is investigated. It was shown possibility of manipulation of duration of sum frequency output pulse in a medium with regular inhomogeneity. Comparisons of the obtained results with the results of constant field approximation(*CFA*), the accurate calculation as well as the case of homogenous nonlinear medium were carried out.

Keywords: regular inhomogeneuity of refractive index, optical fiber, pulse duration, constant intensity approximation, sum frequency generation.
PACS: 42.62-b, 42.65-Ky, 42.70 Hj, 42.81-I

1. INTRODUCTION

A study of inhomogeneity of media in nonlinear optics remains urgent since this is the subject of technological problem that reduces efficiency of frequency converters. In reality, nonlinear crystals being the basic element in frequency converters are subjected to high requirements for their homogeneity. When growing and processing nonlinear materials, optical inhomogeneity arises due to inhomogeneity of the composition, the presence of impurities, defects etc. It leads to a non-constant value of refractive index *n* along the total length of the material. In the sample of optical fiber fabrication process occurs with a refractive index gradient where the core size and refractive index profiles must be kept strictly constant. It should be noticed that, dispersion in a fiber light guide plays the important role in the course of propagation of the short laser pulses. The static inhomogeneity when either refractive index *n* or the direction of the optical axis changes randomly and the regular inhomogeneity when a change in refractive index can be described analytically are distinguished [1-2]. Above mentioned types of inhomogeneity can be inherent in the nonlinear medium itself or arise as a result of parametric interaction due to effect of laser radiation on the medium parameter. The value of inhomogeneity in *n* directly affects the efficiency of the converters as well as the parametric amplification threshold. Scientific researches of the world's leading laboratories over past decades confirm the promise of using optical fiber for information transmission. Specifically, optical solitons are used for this purpose; laser pulses that propagate practically without varying the shape of the pulse due to compensation caused by two reverse effects: dispersion broadening and the effect of narrowing the spectrum of laser emission upon propagating along nonlinear medium. Besides, using soliton's it is possible to control the parameters of ultrashort optical pulses [3-4]. Unlike the bulk medium in optical fiber the transvers dimension of laser radiation is preserved along the entire propagation length of optical fiber. For this reason, due to minimum losses and high concentration of a field, a significant increase in conversion efficiency is observed. Both facts also lead to large interaction lengths. Consequently, fiber-optic sensors, devoid of the disadvantages of traditional electrical sensors, are quite successfully used for monitoring oil wells [5-6]. Parametrical three wave interactions in optical waveguides, in particular, the squeezed states of light, wave generation and propagation of optical solitons have been studied in the approximation of undepleted pumping i.e. *CFA* or numerically [3-4]. Note, that to understand the qualitative pattern of the nonlinear interaction of waves the analytical approach for solving the set of reduced wave equations is preferable. A theoretical study of nonlinear processes has showed that the phase relationships between interacting waves play significant role [7-10], which is not taken into account in the *CFA*.

In this paper, non-stationary generation of the sum frequency in a spatially inhomogeneous optical fiber is studied by employment *CIA*. *CIA* [17,19], which has allowed to take into account the depletion of the pump wave and changes in the phases of all interacting waves. In this approximation we have already analyzed the nonlinear processes *SHG* and CARS in an optical fiber, the effects of self-action and cross-interaction [12-13]. The influence of a regular inhomogeneity of the medium on the nature of the nonlinear process is studied for various values of the pump intensity.

131, H.Javid ave, AZ-1143, Baku
ANAS, Institute of Physics
E-mail: jophphysics@gmail.com

A comparison is made with the case of homogeneous medium. It is considered how the inhomogeneity of the medium affects the duration of the pulse of excited wave.

2. THEORY AND DISCUSSIONS

We analyze non-stationary process of sum frequency generation in fiber with optical inhomogeneity. Theoretical analysis will be carried out in the first order dispersion theory, i.e. without taking into account the effect of dispersive spreading of pulses in the course of wave propagation. Then the coupled equations describing three frequency interaction of optical waves by taking into account the medium losses have view [3, 12]:

$$\begin{aligned}
&\frac{\partial A_1}{\partial z}+\frac{1}{u_1}\frac{\partial A_1}{\partial t}+\delta_1 A_1=-i\gamma(|A_1|^2+|A_2|^2+|A_3|^2)A_1-i\beta_1 A_2^* A_3\exp[i\Delta_0 z+i\psi(z)],\\
&\frac{\partial A_2}{\partial z}+\frac{1}{u_2}\frac{\partial A_2}{\partial t}+\delta_2 A_2=-i\gamma(|A_1|^2+|A_2|^2+|A_3|^2)A_2-i\beta_2 A_3 A_1^*\exp[i\Delta_0 z+i\psi(z)],\\
&\frac{\partial A_3}{\partial z}+\frac{1}{u_3}\frac{\partial A_3}{\partial t}+\delta_3 A_3=-i\gamma(|A_1|^2+|A_2|^2+|A_3|^2)A_3-i\beta_3 A_1 A_2\exp[-i\Delta_0 z-i\psi(z)].
\end{aligned} \quad (1)$$

where $A_{1,2,3}$ -are the complex amplitudes of the pump wave (ω_1) and waves at frequencies $\omega_{2,3}$ ($\omega_3=\omega_1+\omega_2$), $u_{1,2,3}$ -are the group velocities of the corresponding waves, $\delta_{1,2,3}$ -are the linear losses of the interacting waves, γ is an average value of nonlinear coupling coefficient of the interacting waves where the contribution is imported by the self–phase and cross–phase modulation processes,

$$\beta_1=\gamma_{SH}^*/2,\ \beta_2=\gamma_{SH},\ \gamma_{SH}=3\omega_1\varepsilon_o^2\alpha_{SH}f_{112}\chi^{(3)}|E_p|^2|E_{SH}|,$$

ε_0 is a dielectric permittivity of free space , α_{SH} is a constant, depending on the microscopic process, f_{112} is an integral of the overlapping, defining through mode distribution for optical fields and average on transverse coordinates x and y [14], E_p is a field of pump wave at frequency ω_p , E_{SH} is a field of a weak seed second harmonic at frequency $2\omega_p$. $\Delta_0=k_3-k_2-k_1-\Delta(z)$, where Δ_0 and $\Delta(z)$ denote the constant and variable parts of the wave parts of the phase detuning between the interacting waves, respectively, and $\psi(z)=\int_0^z\Delta(z')dz'$. For further simplification the above overlap integrals $f_{ijk}\cong f_{112}\cong 1/A_{eff}$ $(i,j,k=1,2,3)$ and the effective area of a fiber core) are taken identical, that is valid for single-mode waveguides [3]. The boundary conditions for the case of two input waves are written as follows

$$A_{1,2}(z=0)=A_{10,20}(t),\ A_3(z=0)=0 \quad (2)$$

We consider a quasistatic approximation when $u_1=u_2=u_3=u$. Then in (1), it is reasonable to substitute variables z and t with local ones z and $\eta=t-z/u$. Then equation (1) can be given by

$$\begin{aligned}
&\frac{\partial A_1}{\partial z}+\delta_1' A_1=-i\beta_1 A_2^* A_3\exp[i\Delta_0 z+i\psi(z)],\\
&\frac{\partial A_2}{\partial z}+\delta_2' A_2=-i\beta_2 A_3 A_1^*\exp[i\Delta_0 z+i\psi(z)],\\
&\frac{\partial A_3}{\partial z}+\delta_3' A_3=-i\beta_3 A_1 A_2\exp[-i\Delta_0 z-i\psi(z)],
\end{aligned} \quad (3)$$

where

$$\delta_j'=\delta_j+i\gamma(|A_1|^2+|A_2|^2+|A_3|^2),\quad j=1\div 3.$$

$$\delta_j'=\delta_j+i\gamma(|A_1|^2+|A_2|^2+|A_3|^2),\quad j=1\div 3.$$

Then complex amplitude $A_3(z)$ obeys following second-order differential equation obtained from (3)

$$\frac{d^2A_3}{dz^2}+\left[\delta_1'+\delta_2'+\delta_3'+i\Delta_0+i\Delta(z)\right]\frac{dA_3}{dz}+\left[\Gamma_1^2+\Gamma_2^2+(\delta_1'+\delta_2')\delta_3'+i\delta_3'\Delta_0+i\delta_3'\Delta(z)\right]A_3=0, \quad (4)$$

Here $\Gamma_1^2 = |\beta|_2|\beta_3|I_1(z,\eta)$, $\Gamma_2^2 = |\beta|_1|\beta_3|I_2(z,\eta)$, $I_{1,2} = A_{1,2}\cdot A_{1,2}^*$. Here $I_{1,2}(z,\eta)$ is a function of two variables. Wherein obtaining a rigorous analytical solution for $A_3(z)$ becomes difficult. However assuming that $I_{1,2}(z,\eta)$ is a function of single variable η, i.e. $I_{1,2}(z,\eta) = I_{1,2}(\eta)$, equation (4) can be solved. This means employment of *CIA*, since no limitations are imposed to the change in the pump wave phase.

Having put substitution $A_3 = V\exp[-i\psi(z)]$ in the equation (4) we obtain a differential equation for $V(z)$:

$$\frac{d^2V}{dz^2} + [\delta_1' + \delta_2' + \delta_3' + i\Delta_0 - i\Delta(z)]\frac{dV}{dz} + \left[\Gamma_1^2 + \Gamma_2^2 + \delta_3'(\delta_1' + \delta_2') + \Delta_0\Delta(z) + i\delta_3'\Delta_0 - i(\delta_1' + \delta_2')\Delta(z) - i\frac{d\Delta(z)}{dz}\right]V = 0 \quad (5)$$

Further consideration will be carried out for the regular linear inhomogeneous medium $\Delta(z) = \alpha\cdot z$, where α -is the constant quantity. As a result from (5) we get ($\Delta_0 = 0$)

$$\frac{d^2V}{dz^2} + [\delta_1' + \delta_2' + \delta_3' - i\Delta(z)]\frac{dV}{dz} + \left[\Gamma_1^2 + \Gamma_2^2 + \delta_3'(\delta_1' + \delta_2') - i(\delta_1' + \delta_2')\Delta(z) - i\frac{d\Delta(z)}{dz}\right]V = 0 \quad (6)$$

To solve the obtained equation, we put substitution $V(z) = f(\xi)\cdot\exp[(-\delta_1' - \delta_2')z]$, where $\xi = \sqrt{\alpha}(z + i\frac{\delta_3' - \delta_1' - \delta_2'}{\alpha})$. For the function $f(\xi)$ we obtain the Weber's equation [15]:

$$\frac{d^2f}{d\xi^2} - \xi\frac{df}{d\xi} - lf = 0$$

where $l = (1 + i\frac{\Gamma_1^2 + \Gamma_2^2}{\alpha})$, whose solution is given by

$$f(\xi) = c_1[1 + \frac{l}{2!}\xi^2 + \frac{l(l+2)}{4!}\xi^4] + c_2[\xi + \frac{l+1}{3!}\xi^3 + \frac{(l+1)(l+3)}{5!}\xi^5]$$

Hence, for the complex amplitude of the sum frequency wave we obtain $A_3(z) = V\cdot\exp(-i\psi(z)) = f(\xi)\cdot\exp[-(\delta_1' + \delta_2')z - i\psi(z)]$. After substituting the values of the variables by taking into account the boundary conditions for the relative intensity at sum frequency in the regular inhomogeneous medium we obtain ($\delta_3' = \delta_1' + \delta_2'$):

$$I_3(z)/I_{10}(\eta) = (|\beta_3|z)^2\cdot I_{20}(\eta)\cdot\exp[(-2(\delta_1 + \delta_2)z)]\times \left\{\left[1 - \frac{1}{3}|\alpha|z^2 + \frac{1}{15}|\alpha|^2 z^4 - \frac{(\Gamma_1^2 + \Gamma_2^2)^2}{120}z^4\right]^2 + \frac{1}{25}\left[1 - \frac{1}{2}|\alpha|z^2\right]^2\frac{(\Gamma_1^2 + \Gamma_2^2)^2}{4}z^4\right\} \quad (7)$$

In the absence the inhomogeneity of nonlinear medium i.e. $\Delta(z) = 0$ ($\alpha = 0$), for the homogeneous medium we get

$$I_3(z) = |\beta_3|^2 I_{10}(\eta)I_{20}(\eta)z^2\cdot\left\{1 - \frac{(\Gamma_1^2 + \Gamma_2^2)^2 z^4}{300}\left[2 - \frac{1}{48}(\Gamma_1^2 + \Gamma_2^2)^2 z^4\right]\right\}\cdot\exp[-2(\delta_1 + \delta_2)z)]$$

Hence in *CFA*, when $\beta_1 = 0$ ($\Gamma_1 = 0$) and δ_1=0, we get

$I_3^{CFA}(z) = |\beta_3|^2 I_{10}(\eta)\cdot I_{20}(\eta)z^2(1 - \frac{\Gamma_2^4 z^4}{6})\cdot\exp[-2\delta_2 z)]$, and for the stationary case

$I_3^{CFA}(z) = \left|\beta_3\right|^2 I_{10}\cdot I_{20} z^2 (1-\frac{\Gamma_2^4 z^4}{180})\cdot \exp\left[-2\delta_2 z)\right]$ [16].

Below we analyze expression (7), obtained in the CIA, for the cases of a weak and strong inhomogeneous medium with a pulsed character of the pump wave and the wave at frequency of ω_2. Assume that the ultrashort pump wave with duration of τ_1 and a long pulse wave at frequency of ω_2 with duration τ_2 at the left entrance to the optical fiber have the form of a Gaussian beam $A_{10,20}(\eta) = A_{10,20}\exp(-\eta^2/2\tau_{1,2}^2)$, provided that $\tau_1 << \tau_2$ Wherein relationships for the $\Gamma_{1,2}z$ in the *CIA* have the view

$\Gamma_1 z = \sqrt{|\beta_2\|\beta_3|I_{10}(\eta)}z = \sqrt{|\beta_2\|\beta_3|I_{10}}\cdot z\exp(-\eta^2/2\tau_1^2) = \Gamma_1(0)z$, where $\Gamma_1(0) = \sqrt{|\beta_2\|\beta_3|I_{10}}$,

$I_{10} = A_{10}\cdot A_{10}^*$ and $\Gamma_2 z = \sqrt{|\beta_1\|\beta_3|I_{20}(\eta)}z = \sqrt{|\beta_1\|\beta_3|I_{20}}\cdot z\exp(-\eta^2/2\tau_2^2) = \Gamma_2(0)z$, here $\Gamma_2(0) = \sqrt{|\beta_1\|\beta_3|I_{20}}$.

In the case of a weak inhomogeneous medium $|\alpha|z^2 < 1$ and small interaction lengths $\Gamma z < 1$, from (7) we get

$$I_3(z) \approx \left[\left|\beta_3\right|z\right]^2 I_{10}(\eta)I_{20}(\eta)\cdot\left[1-\frac{2}{3}|\alpha|z^2 - \frac{(\Gamma_1^2+\Gamma_2^2)^2}{60}z^4\right]\cdot\exp[-2(\delta_2+\delta_1)z], \qquad (8)$$

Hence from (8) in the *CFA* we obtain

$$I_3(z) \approx \left[\left|\beta_3\right|z\right]^2 I_{10}(\eta)I_{20}(\eta)\left(1-\frac{2}{3}|\alpha|z^2 - \frac{\Gamma_1^4}{60}z^4\right)\cdot\exp(-2\delta_2 z) \approx \left[\left|\beta_3\right|z\right]^2 I_{10}(\eta)I_{20}(\eta)$$

Taking into account the pulsed character of pump wave, we rewrite (8) in the form

$I_3(z)/I_{10} \approx I_2\exp\left\{(-\eta^2/\tau_1^2)\cdot\left[1-\frac{1}{30}\left(\Gamma_1^2(0)+\Gamma_2^2(0)\right)\Gamma_1^2(0)z^4\right]\right\}$. It is seen that an increase in the input pulse duration is determined by the following relation

$\tau_{3in\,\mathrm{hom}} = \tau_1/\sqrt{1-\frac{1}{30}\left(\Gamma_1^2(0)+\Gamma_2^2(0)\right)\Gamma_1^2(0)z^4}$. In the CFA, this effect of increasing the pulse duration is weak $\tau_{3in\,\mathrm{hom}} = \tau_1/\sqrt{1-\frac{1}{30}\Gamma_1^4(0)z^4}$ since Γ_2.

In a strong inhomogeneous medium $|\alpha|z^2 > 1$ and $\Gamma z < 1$, from (7) we obtain

$$\begin{aligned} I_3(z) \approx{}& \left[\left|\beta_3\right|z\right]^2\cdot I_{10}(\eta)I_{20}(\eta)\exp\left[(-2(\delta_1+\delta_2)z)\right]\times \\ &\left(1-\frac{2}{3}|\alpha|z^2+\frac{11}{45}|\alpha|^2z^4-\frac{2}{45}|\alpha|^3z^6-\frac{1}{45\cdot 4}|\alpha|z^2\left(\Gamma_1^2+\Gamma_2^2\right)z^4\right)\cdot \end{aligned} \qquad (9)$$

Hence in the *CFA* we obtain

$$I_3(z)/I_{10} \approx \left[\left|\beta_2\right|I_{20}(\eta)z\right]^2\cdot\left(1-\frac{2}{3}|\alpha|z^2+\frac{11}{45}\alpha^2z^4-\frac{2}{45}|\alpha|^3z^6-\frac{1}{45\cdot 4}|\alpha|z^2\Gamma_1^4z^4\right).$$

In a homogeneous environment $I_2(z)/I_{10} \approx \left[\left|\beta_2\right|I_{10}(\eta)z\right]^2\cdot\exp\left[(-2(\delta_1+\delta_2)z)\right]$

For the homogeneous medium $I_2(z)/I_{10} \approx \left[\beta_2 \left| I_{10}(\eta) z \right]^2 \cdot \exp[(-2(\delta_1+\delta_2)z)\right]$.

Analysis of (9) for the duration of the sum frequency pulse with $|\alpha| z^2 < 1.5$ yields

$$I_3(z)/I_{10} \approx I_{20} \exp\left[(-\eta^2/\tau_1^2) \cdot \left(1 - \frac{1}{45} |\alpha| z^2 \left(\Gamma_1^2(0) + \Gamma_2^2(0) \right) \Gamma_1^2(0) z^4 \right) \right]$$

Hence duration of output pulse of radiation at sum frequency ω_3 in a strong inhomogeneous medium is determined by $\tau_{3in\,\mathrm{hom}} = \tau_1 / \sqrt{1 - \frac{1}{45} |\alpha| z^2 \left(\Gamma_1^2(0) + \Gamma_2^2(0) \right) \Gamma_1^2(0) z^4}$, and in the homogeneous medium $\tau_{3\,\mathrm{hom}} = \tau_1$. This fact of increasing the duration of pulse becomes significantly weak in *CFA* $\tau_{3in\,\mathrm{hom}} = \tau_1 / \sqrt{1 - \frac{1}{45} |\alpha| z^2 \Gamma_1^4(0) z^4}$ As can be seen from (7) intensity of the wave of sum frequency depends on the relationship between parameters Γ_1^2 and Γ_2^2 whose ratio equals $\Gamma_1^2/\Gamma_2^2 = \beta_2 I_{10}/\beta_1 I_{20} = n_1 \omega_2 I_{10}/n_2 \omega_1 I_{20}$. For the intensity of pump wave $I_{10} >> I_{20}$ and frequency conversion upward $\omega_1 >> \omega_2$ the ratio $\Gamma_1^2/\Gamma_2^2 \sim 1$, however when $\omega_1 << \omega_2$ the ratio $\Gamma_1^2/\Gamma_2^2 >> 1$ and one can neglect Γ_2^2 in this case. Consider second case to evaluate the pulse duration at sum frequency for various inhomogeneous media. Let $\Gamma_1(0) z = 0.9$ and we neglect parameter Γ_2.

As expected, with increase in the degree of inhomogeneity of the optical system, the quality (*Q*-factor) of the system, by analogy with the *Q*-factor of an optical resonator, decreases, that leads to broadening of the sum frequency pump excited in the given system. Really in the case of strong inhomogeneity the term of regular inhomogeneity included into exponential dependence (9) affects onto duration of pulse increasing it. If in a weak inhomogeneous medium $|\alpha| z^2 = 0.3, \tau_{2in\,\mathrm{hom}} = 1.0041 \cdot \tau_1$, but in a strong inhomogeneous medium if $|\alpha| z^2 = 1.5$ we obtain $\tau_{2in\,\mathrm{hom}} = 1.01378 \cdot \tau_1$.

Let us carry out numerical analysis of equation (7) obtained in *CIA*. Fig.1 shows, how the pulse duration varies depending on problem parameters according to analysis of equations (8) and (9). Really, in the case of strong inhomogeneity the term of regular inhomogeneity included into exponential dependence (9) affects onto duration of pulse increasing it (compare solid and marked curves). Variation of intensities of frequency ω_3 in a strong inhomogeneous medium is determined by

$\tau_{3in\,\mathrm{hom}} = \tau_1 / \sqrt{1 - \frac{1}{45} |\alpha| z^2 \left(\Gamma_1^2(0) + \Gamma_2^2(0) \right) \Gamma_1^2(0) z^4}$, and in the homogeneous medium $\tau_{3\,\mathrm{hom}} = \tau_1$. This fact of increasing the duration of pulse becomes significantly weak in *CFA* $\tau_{3in\,\mathrm{hom}} = \tau_1 / \sqrt{1 - \frac{1}{45} |\alpha| z^2 \Gamma_1^4(0) z^4}$ As can be seen from (7) intensity of the wave of sum frequency depends on the relationship between parameters Γ_1^2 and Γ_2^2 whose ratio equals $\Gamma_1^2/\Gamma_2^2 = \beta_2 I_{10}/\beta_1 I_{20} = n_1 \omega_2 I_{10}/n_2 \omega_1 I_{20}$. For the intensity of pump wave $I_{10} >> I_{20}$ and frequency conversion upward $\omega_1 >> \omega_2$ the ratio $\Gamma_1^2/\Gamma_2^2 \sim 1$, however when $\omega_1 << \omega_2$ the ratio $\Gamma_1^2/\Gamma_2^2 >> 1$ and one can neglect Γ_2^2 in this case. Consider second case to evaluate the pulse duration at sum frequency for various inhomogeneous media. Let $\Gamma_1(0) z = 0.9$ and we neglect parameter Γ_2.

As expected, with increase in the degree of inhomogeneity of the optical system, the quality (*Q*-factor) of the system, by analogy with the *Q*-factor of an optical resonator, decreases, that leads to broadening of the sum frequency pump excited in the given system. Really in the case of strong inhomogeneity the term of regular inhomogeneity included into exponential dependence (9) affects onto duration of pulse increasing it. If in a weak inhomogeneous medium $|\alpha| z^2 = 0.3, \tau_{2in\,\mathrm{hom}} = 1.0041 \cdot \tau_1$, but in a strong inhomogeneous medium if $|\alpha| z^2 = 1.5$ we obtain $\tau_{2in\,\mathrm{hom}} = 1.01378 \cdot \tau_1$.

Let us carry out numerical analysis of equation (7) obtained in *CIA*. Fig.1 shows, how the pulse duration varies depending on problem parameters according to analysis of equations (8) and (9). Really, in the case of strong inhomogeneity the term of regular inhomogeneity included into exponential dependence (9) affects onto duration of pulse increasing it (compare solid and marked curves). Variation of intensities of input pump wave and second wave at frequency ω_2 directly affects the duration of output sum frequency wave through the parameters Γ_2 and Γ_1 respectively. The given result is more weaker in *CFA* since there is no exponential dependence versus pump intensity related to the condition $\Gamma_2 = 0$ (dashed curve). Hence with increase in the degree of inhomogeneity of

nonlinear medium as can be expected the pulse duration increases. In Fig.2 variation of relative intensity of sum frequency wave is shown. Temporary dependences of relative intensity I_3 / I_{10} are depicted for different values of losses and intensities of interacting waves. At smaller values of intensities of interacting waves and larger values of losses the curve flattening and saturation of the dependence is observed (curve 1). Also in fig.2 it is seen that how the enhancement of pump intensity (curves 3-5) and decrease in losses (curves 1 and 3) lead to increased conversion efficiency. Along with this process the ratio I_3 / I_{10} also varies due to change in the phase of pump wave which is taken into account in *CIA* (curves1,3-5). Here the result of *CFA* (curve 2) is given too. Comparison of curves 1 and 2 calculated at the same parameters of problem demonstrates lower efficiency of the process in *CIA* than that of *CFA*. This is explained by nonzero parameter β_1 in the *CIA*, taking into account reverse reaction of excited wave on the pump wave. Really, unlike the *CFA*, where the amplitude of pump wave remains constant, in the *CIA* taking into account the change of complex amplitude of pump wave leads to decrease in the ratio I_3 / I_{10}.

As a result of the nonlinear interaction of optical waves upon generation of the wave at sum frequency occurs broadening of the wave at sum frequency in the regular inhomogeneous medium as compared with the case of homogeneous medium. It has allowed to manipulate the duration of the output harmonic pulse of sum frequency wave in a regular inhomogeneous medium by changing intensities of both pump wave and wave with frequency ω_2 at the input.

Thus, the possibility of controlling the parameter of the output pulse by a nonlinear optical method is shown. In a regular inhomogeneous medium, one can manipulate the parameter of the output radiation by adjusting the input pump intensity.

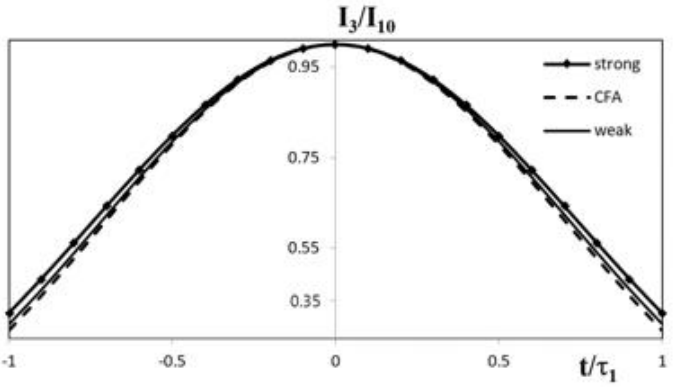

Fig.1. Dependences of relative intensity of sum frequency wave I_3 / I_{10} versus time t / τ_1 at $\delta_3 = 0$, $\Gamma_1 z$ =0.9, $\Gamma_2 = 0.8\Gamma_1$. The dashed curve is the result of calculation for uniform medium ($\alpha = 0$), so and in *CFA* ($\Gamma_2 z$ =0). Solid curve corresponds to the weak inhomogeneous medium, solid line with dots corresponds to the strong inhomogeneous medium at $|\alpha| z^2$ =1.5 calculated in *CIA*.

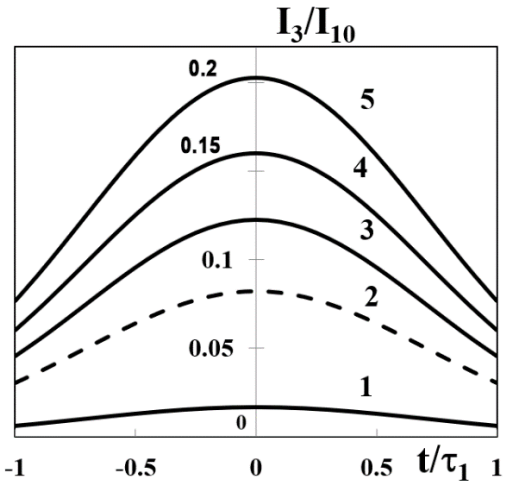

Fig. 2. Dependences of relative intensity of sum frequency wave I_3 / I_{10} versus time t / τ_1 at $\Gamma_2 = 0.5\Gamma_1$, $|\alpha| z^2$ =1.5 for $\Gamma_1 z$ =0.9 (curve 4), 0.8 (curve 3), 0.7 (curves 1 and 2), $\delta_3 z$ =0 (curves 2-5) and 0.5 (curve (1) Calculations were carried out in *CIA* (curves 1, 3-5) and in *CFA* (dashed curve 2).

3. CONCLUSIONS

Thus, in the constant intensity approximation, we have carried out investigation of sum frequency generation in an optical fiber with a linear regular inhomogeneity of the refractive index. An analytical expression is obtained for the intensity of sum frequency wave by taking into account the effects of self-action and cross-actions of interacting three waves. The analytical and numerical results are compared with the results in the *CFA*. A broadening of a pulse wave at sum frequency in a regular inhomogeneous medium as compared to the case of a homogeneous medium. The possibility of manipulating the duration of the output pulse of generated wave in a regular inhomogeneous medium due to variations of input values of intensities both pump wave and wave with frequency ω_2 is shown.

[1] *F.S. Ghen.* Optically induced change of refractive indices in $LiNbO_3$ and $LiNaO_3$. Appl. Phys. 1960, 40(8), pp. 3389-3396.

[2] *S.A. Akhmanov, D.P. Krindach, A.P. Sukhorukov, R.V. Khokhlov*. Letters to JETP, 1967. 6(2), pp. 509-513.

[3] *G. Agrawal*. Nonlinear Fiber Optics. Academic, San-Diego, Calif., 1995.

[4] *L.F. Mollenauer, J.P. Gordon.* Solitons in Optical Fibers. Fundamentals and Applications. 2006 Elsevier, pp. 296.

[5] *R. Cannon, F. Aminzadeh.* University of Southern California. Distributed Acoustic Sensing: State of the Art. Paper SPE 163688 Presented at the 2013 SPE Digital Energy Conference and Exhibition held in The Woodlands, Texas, USA, 5-7 March 2013, pp. 1-10.

[6] *A. Bukhamsin, R. Horne*. Paper SPE 170679-MS Presented at the 2014 SPE Annual Technical Conference and Exibition held in Amsterdam, the Netherlands, 27-29 October 2014, pp. 1-19.

[7] *N. Blombergen. W.A. Benjamin.* Nonlinear Optics., Inc. New York-Amsterdam., 1965.

[8] *Y.R. Shen.* Principles of Nonlinear Optics., Wiley, New York, 1984.

[9] *M.D. Reid, P.D. Drummond.* Phys. Rev. Lett., 1988, 60, pp. 2731.

[10] *R.W. Boyd.* Nonlinear optics., San Diego, Academic Press, 2008, pp. 613.

[11] *Z.H. Tagiev, R.J. Kasumova, R.A. Salmanova, N.V. Kerimova.* J. Opt. B: Quantum Semiclas. 2001, Opt. 3, 84.

[12] *Z.H. Tagiev, R.J. Kasumova.* Theoretical studies on frequency doubling in glass optical fibers in constant-intensity approximation. Optics & Communications, 2006, v.261, pp.258-265.

[13] *R.J. Kasumova, N.V. Kerimli, G.A. Safarova*. Phase effects on coherent anti-Stokes Raman scattering. J. of Applied Spectroscopy. 2020.

[14] *J.G. Gabriagues, L. Fersing.* In Digest of Conference on Lasers and Electro Optics, OSA, Washington, D.C., 1984, pp.176. *J.G. Gabriagues, H. Fevrier.* Opt. Lett.,1987,12, pp. 720.

[15] *E. Kamke.* Differential Gleichungen. Leipzig, 1959, pp. 576.

[16] *V.G. Dmitriev, L.V. Tarasov.* Applied Nonlinear Optics. Fizmatlit, Moscow, 2004, 360.

[17] *Z.H. Tagiev, A.S. Chirkin.* Kvantovaya Electronika (Moscow), 4(7) (1977), 1503-1508.

[18] *H. Bateman, A. Erdelyi.* Higher transcendental functions. New-York, Mc Graw –Hill Book Company, Inc. 1953, v.1, 296p.

[19] *R.J. Kasumova, Z.H. Tagiev, Sh.Sh. Amirov*. Laser pulse manipulation in optical fiber, News of Baku State University. 2021, N1, pp.72-82.

Received: 06.04.2022

ELECTROPHYSICAL PROPERTIES OF GAMMA-IRRADIATED POLYETHYLENE TEREPHTALATE (PETPh\CdS) NANO-COMPOSITS ON THE BASE OF POROUS MEMBRANES

M.A. NURIYEV, A.A. SHUKUROVA, A.SH. MAMMADOVA, A.I. GASIMOVA
Institute of Radiational Problems of Azerbaijan NAS
Az 1143, B. Vakhabzade, 9, Baku, Azerbaijan

The electrophysical properties of initial and irradiated *PETh/CdS* nano-composites obtained on the base of industrial track membranes from *PETPh* with three and twenty of formation cycles are investigated in the present work. It is shown that the observable effects in frequency dependence of electrophysical properties of *PETh/CdS* composites are connected with polarization change in matrix interphase boundary with filler and CdS nano-particles in PETPh near-surface region and radiation processes in polymer matrix at influence of gamma radiation. The study of frequency dependence of resistivity of porous *PETPh* and composites on *PETh/CdS* base shows that the resistivity of porous *PETPh* decreases as a result of destruction after influence of gamma radiation and the taking place matching leads to the increase of physical interaction in boundary nano-particle – polymer, and resistivity of *PETh/CdS* composites relatively increases.

Keywords: Polyethylene terephthalate (*PETPh*), porous track membrane, dielectric constant, dielectric losses, resistivity, interphase boundary, layerwise chemisorption, irradiation dose.
PACS: 61.80Ed;72.80. Tm;72.80. Le

INTRODUCTION

Last time the fields of technique and science which are connected with formation of nano-dimensional materials and structures on their base rapidly develop. The big interest to this direction is connected with unique properties which substance particles have in nano-dimensional scale. It is known that material nano-dimensional particles have unique optical, electrophysical and magnetic properties in comparison with unitary materials of the same chemical composition [1,2].

In this connection with this fact, the scientific investigations are directed to development of synthesis methods of nano-dimensional semiconductor crystals and compositions on their base for the problem solving in instrument engineering, biology, ecology and medicine [3–5]. The metal chalcogenides of CdS, CuS, ZnS types are the most studied from these semiconductor materials. They are obtained in the form of powders, films, solutions and are introduced in the composition of the different polymer matrixes [6–11].

The saving of the nano-particle stability and their optical characteristics connected with them are the important fact in synthesis process. For this problem solving the nano-particles are introduced in the different polymer matrixes and thus their fixation in attitude positions is carried out [12–14]. That's why the investigations of nano-particle synthesis methods and their stabilization by different manners are the actual problems.

The nano-particle synthesis method in tracks of polymer membranes obtained at their irradiation by heavy particles is the one of the perspectives nano-composite obtaining method. We consider that tracks of these membranes are well for stabilization of nano-particle different types including chalcogenide particles [15–16]. The formation of these materials requires the carrying out of the fundamental investigations of the processes carrying out at their formation and influence of different external factors on their electrophysical properties. The porous structure of polyethylene of low density (*PELD*) and polyethylene terephthalate (*PTPh*) have been obtained earlier by us by the method of orientation extract [17]. PELD/CdS and PTPh /CdS nano-composites are formed on the base of obtained porous structures by the method of layerwise chemisorption and their electrophysical properties before and after gamma irradiation are studied [18–19]. The results of electrophysical characteristic study in particular, frequency-temperature dependences of the main dielectric parameters (ε, tgδ and ρ) of *PETPh/CdS* nano-composites obtained on the base of industrial track membranes from *PETPh* with three and twenty formation cycles modified by gamma irradiation, are shown in the given work. The study of these composite properties is of big interest for their application in the different fields of science and electrotechnique.

EXPERIMENTAL PART

PETPh/CdS nano-composites obtained on the base of industrial track membranes (porous films) from *PETPh* by thickness h~27 μm prepared in *JNR* (Dubna) are the objects of investigation. The pore concentration in these membranes is $n=5\cdot10^9\ cm^{-2}$. CdS nano-particles are formed in pores of track membranes of *PETPh* by the method of layerwise chemisorption [20]. The samples of porous PETPh and nano-composites PETPH/CdS on its base with three and twenty cycles of CdS formation are investigated. The supposed schematic image of PETPh/CdS nano-composite cross-section with three and twenty cycles of CdS formation is shown in fig.1. We suppose that the formed CdS nano-particles in porous polymer matrix mainly form in near-surface layer of porous *PETPh* at layerwise chemisorption and the small part from these particles penetrates into matrix pores. The change of dielectric parameters (ε, $tg\delta$ and ρ) in alternative field is measured with the help of emittance *E*7-20 at hate rate 2,5*K/min*. The sample irradiation is carried out on installation *MPX-γ-25M* on the base of Co^{60} isotope.

131, H.Javid ave, AZ-1143, Baku
ANAS, Institute of Physics
E-mail: jophphysics@gmail.com

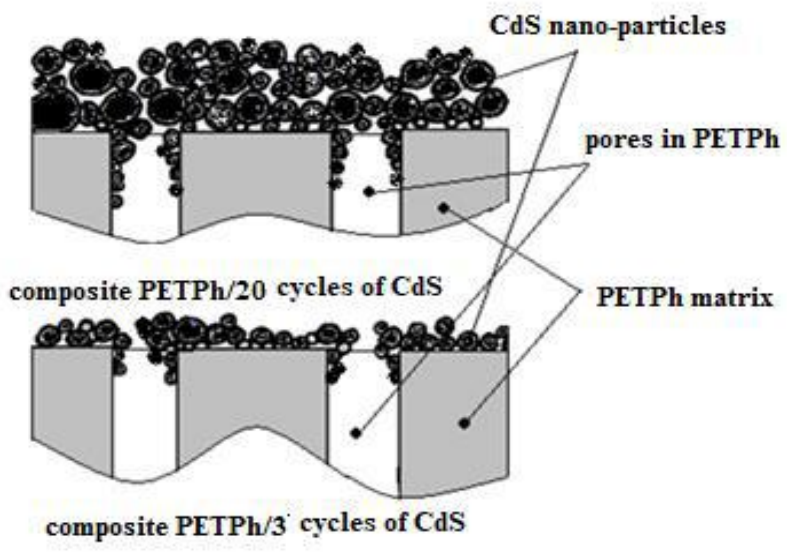

Fig. 1. Schematic image of cross-section of *PETPh/CdS* nano-composites with three and twenty cycles of CdS nano-particle formation.

RESULT DISCUSSION

The frequency dependences $\varepsilon(\nu)$, $tg\delta(\nu)$ and $lg\rho(\nu)$ of polyethylene terephthalate (*PTPh*) and *PETPh/CdS* composites on its base with different cycles of formation which are irradiated at dozes 100, 300 and 500Gy are shown in presented figures below.

The frequency dependences of dielectric constant of initial and irradiated porous *PETPh* and *PETPh/CdS* composites on its base with different formation cycles are shown in fig.2. It is known that values of *PETPh* dielectric constant is in interval ~3,1÷3,25 [21,22]. But tracks lead to the formation of porous structure on the surface and in *PETPh* volume as a result of the fact ε values decrease and as experimental data show that these values are in region ~1,6 for polymer and in region ~(1,2÷1,3) for nano-composite. We consider that this fact causes to increase of CdS nano-particle concentration increase, high value of dielectric constant of CdS (ε~9) and changes of the thickness of each layer. As it is seen from the frequency dependences the influence of gamma irradiation leads to ε value increase up to ~2,6 for *PETPh* and up to ~1,8 for nano-composites on their base. We consider that such change of ε values is the result of transversal matching taking place after irradiation influence in polymer matrix and improvement of polymer matrix interaction with CdS nano-particles in polymer near-surface layer. The given results (fig.1) show that sample dielectric constant decreases with increase of measuring field frequency. Such change shows the relaxation character of dielectric constant dependence for matrix and all composites. The relatively high value of dielectric constant at low frequencies with filler increase is caused by increase of effective surface of interphase layer and charged accumulated in it taking part in relaxation process Maxwell-Vagner in composite material. The tendency to the increase of ε dielectric constant value is observed in the end of measured frequency range ($\nu > 5\times10^5 Hz$).

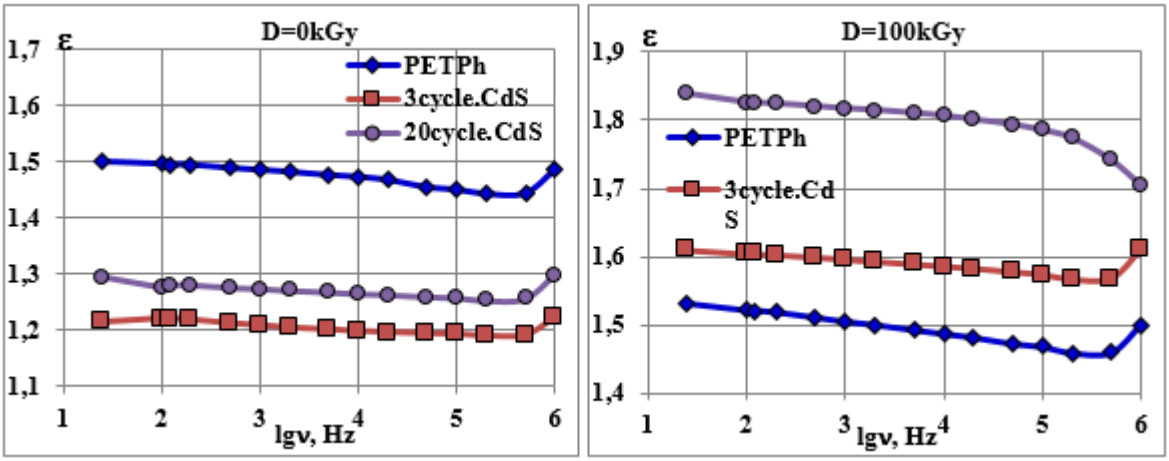

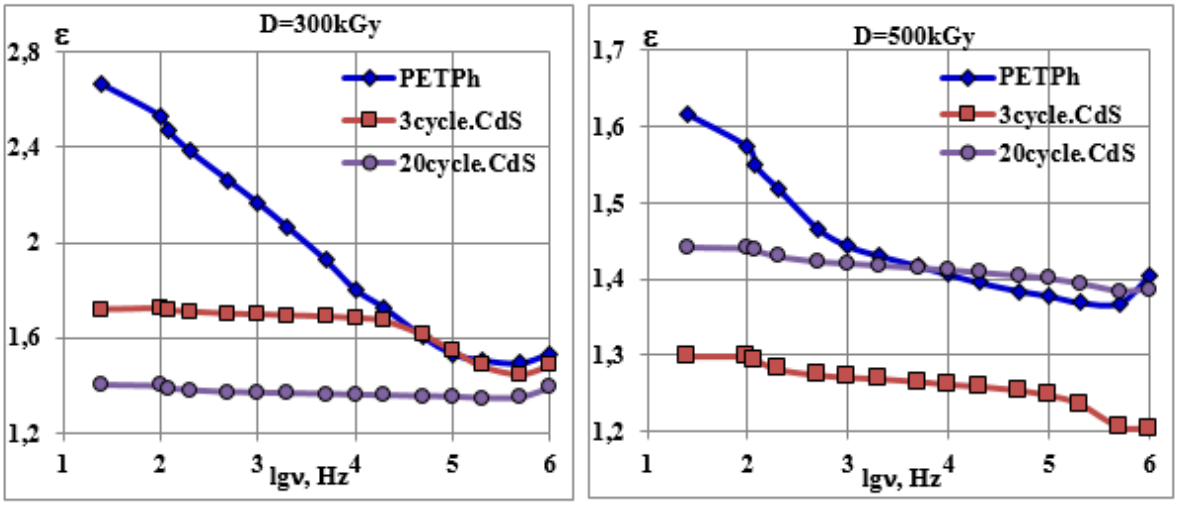

Fig.2. The frequency dependences of dielectric constant of initial and irradiated porous PETPh and PETPh/CdS composites on its base with different number of formation cycles.

As it is seen from the frequency dependences after influence of gamma irradiation the dielectric constant of *PETPh* increases up to doze *300Gy* with the further decrease at *500Gy*.It is considered that such trend of a curve causes to maximum matching at irradiation up to doze *300Gy*. This leads to the increase of polymer crystallinity and increase of effective surface of interphase between crystalline and amorphous regions of *PETPh*. Besides *ε* increase can cause the polarity of polyethylene terphtalate itself. This proves the maximums in relatively low-frequency region of *tgδ=f(ν)* dependence of porous polyethylene terephtalate (fig.3).

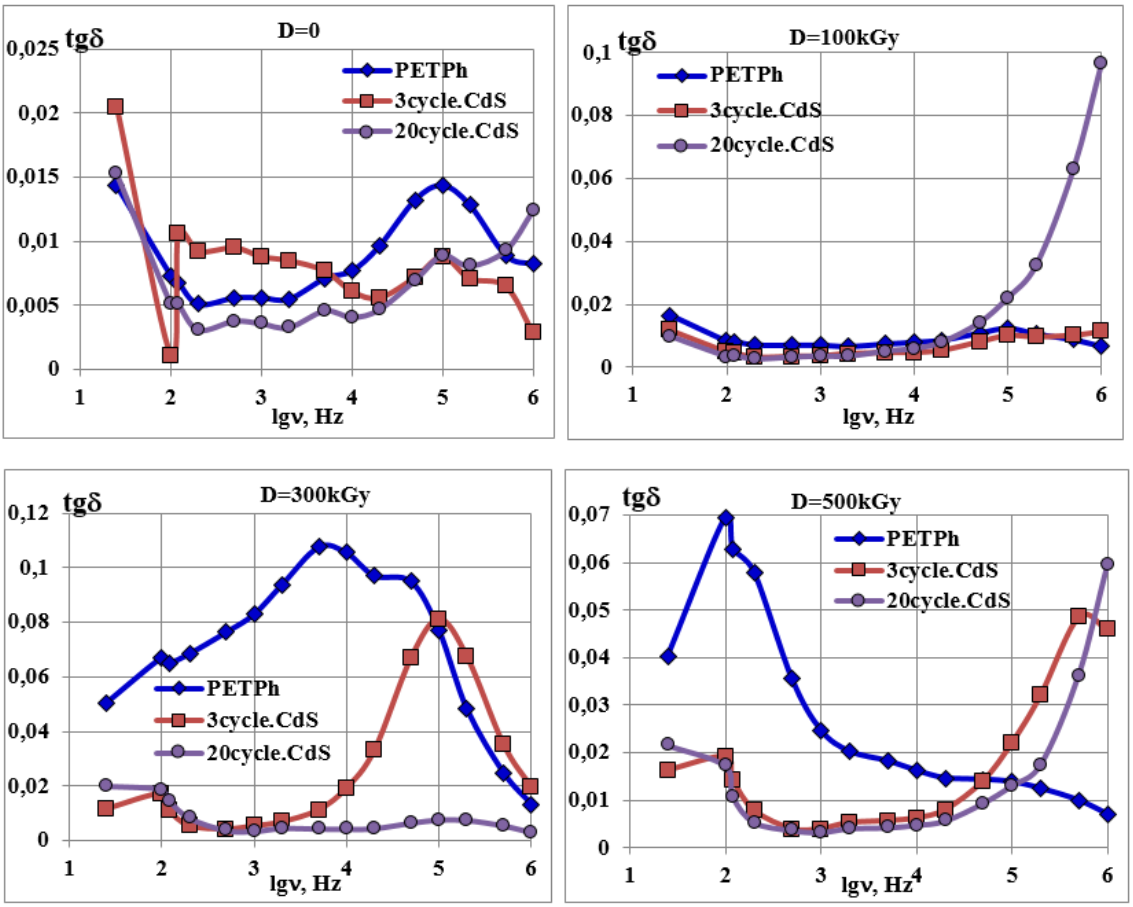

Fig.3. The frequency dependences of dielectric losses of initial and irradiated porous *PETPh* and *PETPh/CdS* composites on its base with different number of formation cycles.

The increase of dielectric constant is observed in frequency dependence of *PETPh/CdS* composites obtained at 3 and 20 cycles of formation and irradiated up to doze 100kGy. It is considered that ε increase is connected with both the increase of nanoparticle interaction between each other and active products on polymer surface appearing after initial destruction in polymer matrix chains, polarity and piezoelectricity of CdS particles [23]. The above mentioned proves the increase of *PETPh/CdS* composite dielectric constant in initial stages of irradiation doze (up to 100*kGy*) with the increase of filler content and observable increase of tgδ of composites *PETPh/20* cycles of CdS irradiated by doze 100*kGy* at high frequencies (fig.3). The observable increase of tgδ of *PETPh/20* cycles of CdS irradiated at doze 100*kGy* is connected with both increase of active product interaction formed after irradiation (for example, low-molecular impurities and polar groups C-O) by each other and CdS nano-particle polarity.

The further increase of irradiation doze (up to 300*kGy*) leads to decrease of ε value for both composites. The composites with high filer content (of PETPh/20th cycles of CdS) has relatively low values of dielectric constant and dielectric loss tangent (fig.2 and fig.3) than the composite with low content (*PETPh/3* cycles of CdS). It is considered that observable fact is connected with increase of transversal matching process between polymer chains and interaction improving in interphase boundary polymer-filler which leads to decrease of relaxor mobility in polymer composite *PETPh/CdS*. The further increase of radiation dose (up to 500*kHz*) leads to stabilization of ε value as a result of destruction dominating in polymer composites *PETPh/CdS* and relaxor polarization increase in CdS. The above mentioned proves the maximums in the dependence of $tg\delta=f(v)$ composites in freqiency region $5\cdot10^6 Hz$ and which corresponds to filler dipole polarization. Besides, in this case the big role of volume charges in composite polymer layer formed at irradiation by dose 500*kGy* which leads to their interlayer division at polarization.

The frequency dependences of resistivity of initial and irradiated *PETPh* and *PETPh/CdS* composites on its base with different number of formation cycle are presented in following figure (fig.4).

It is known that frequency dependence of resistivity of non-homogeneous structures is described by following regularity:

$$\rho = \rho_0 v^s \quad (1)$$

where s is constant which characterizes the change of resistivity in the dependence of frequency. *S* parameter value defines the charge carrier mobility character, i.e. material electric conduction mechanisms under influence of alternating electric field. If the condition $s<1$ is carried out then carrier motion is the translation one, if $s>1$ then it is considered that carrier motion is the localized one, i.e. the displacement or oscillation of the charge takes place between localized states [24, 25]. If for the value of this constant the condition $0,7\leq s\leq 1$ is carried out, then it is considered that hopping of electric conduction is the right one for the measured material [26]. It is considered that composite electric conduction *PETPh/CdS* on the base of porous *PETPh* which has the heterogeneous structure also can be described by expression (1). Taking logarithm of this expression we obtain the following formula for the calculation of *s* parameter value:

$$s=\Delta(lg\rho)/\Delta(lgv) \quad (2)$$

The values of parameter s calculated from dependences $lg\rho=f(v)$ (fig.4) for the initial and irradiated porous *PETPh* and *PETPh/CdS* composite is presented in the table.

Table

s parameter values calculated from dependences $lg\rho=f(v)$

№	D, *kGy*	*CdS* contene in the composites	$\Delta(lgv)$	$\Delta(lg\rho)$	***s***
1	0	0; 3ts.; 20ts.	2,0	2, 26	1,13
2	100	0; 3ts.; 20ts.	2,0	2,48	1,24
3	300	0	2,0	1,84	0,92
		3ts.	2,0	3,2	1,6
		20ts.	2,0	2,4	1,2
4	500	0	2,0	1,72	0,86
		3ts.; 10ts.	2,0	2,62	1,3

As it is seen from the table the condition $s>1$ is mainly carried out for the s parameter value for irradiated and initial samples, the irradiated samples of porous *PETPh* at dozes 300 and 500*kGy* for the which the condition $0,7\leq s\leq 1$ are the exclusion. As it is above mentioned, the carried-out condition $0,7\leq s\leq 1$ corresponds to electric conduction hopping, i.e., in irradiated samples at dozes 300 and 500*kGy* of porous PETPh the charge motion takes place in the volume or on pores of the surface. At condition $S>1$ it is considered that carrier motion is the localized one, i.e., the charge displacements (oscillations) between localized states is observed. In first case the sample resistivity relatively decreases and becomes closer to semiconductors and in second place the sample resistivity relatively increases and becomes close to dielectrics where interlayer and dipole polarization processes dominate.

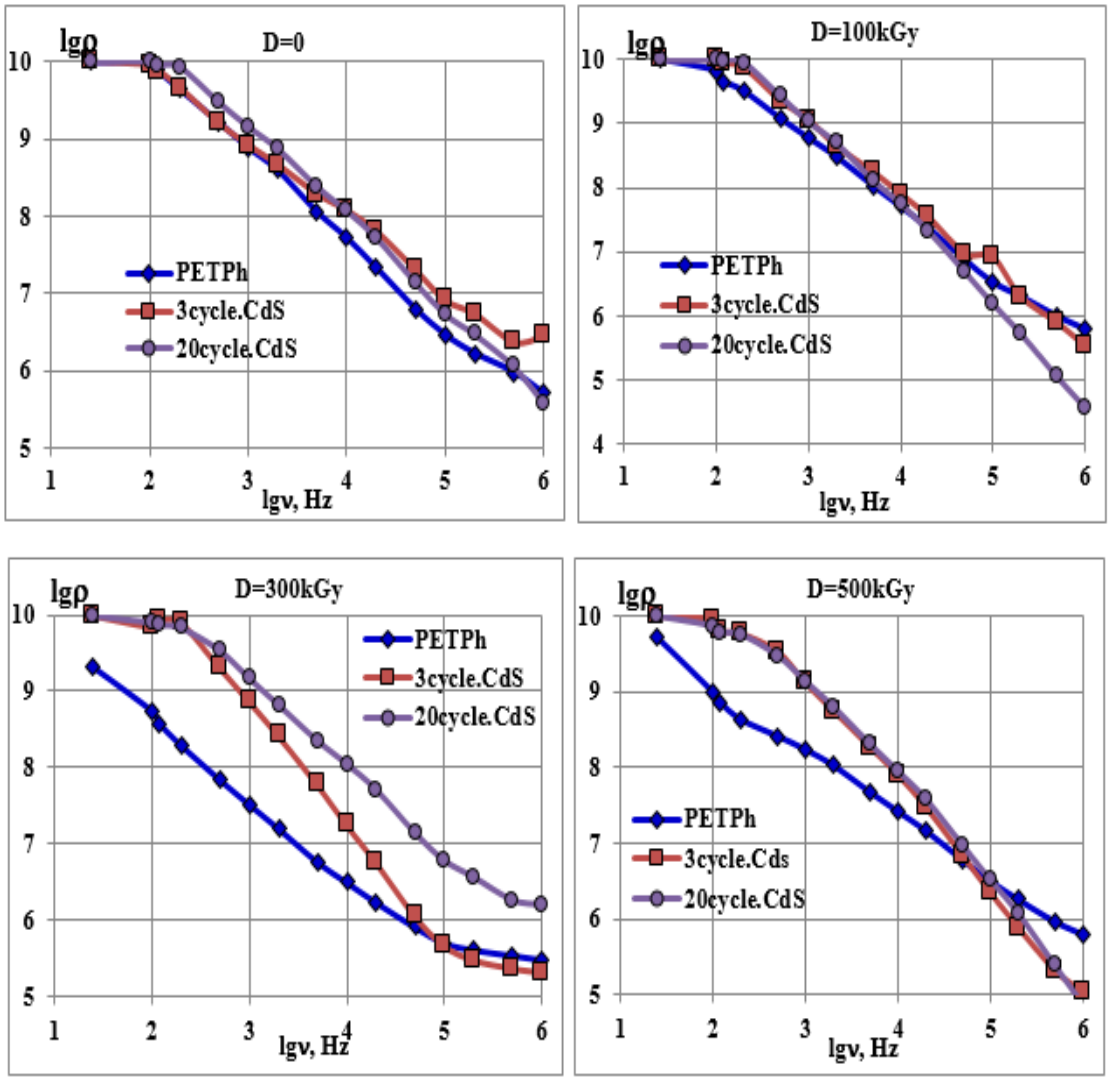

Fig.4. The frequency dependence of resistivity of initial and irradiated porous *PETPh* and *PETPh/CdS* composites on its base with different number of formation cycles.

The temperature dependences of resistivity of initial and irradiated porous *PETPh* and *PETPh/CdS* composites on its base prove the above-mentioned version of conduction mechanism (fig.5). The observable minimums in low-temperature region in temperature dependence of resistivity of polymer and composites are considered as the result of retained moisture desorption. From the dependences it is seen that samples of irradiated *PETPh* have the relatively low value of resistivity which coincides with obtained data from frequency dependences for the irradiated samples at dozes 300 and 500*kGy*.

By other hand, the relatively low inclination of direct composites irradiated by doses 100 and 300*kGy* in comparison with *PETPh* inclinations in dependence high-temperature part can be estimated as dominating of matching in this doze region for the composites. The thickness increase with the increase of cycle number in near surface layer from CdS nano-particles leads to the decrease or disappearance of minimum depth in low-temperature region as the result of increase of physical interaction between nano-particles and polymers after influence of gamma radiation.

CONCLUSION

Thus, the observable effects in frequency dependence of *PETPh/CdS* composite dielectric properties obtained on the base of porous track membranes of PETPh are connected with both the change of polarization in matrix interphase boundary with filler and CdS nano-particles in near-surface region of *PETPh* and radiation processes of polymer matrix at influence of gamma radiation. By study of irradiation of resistivity frequency dependence of porous *PETPh* and composites on its base of *PETPh/CdS* it is established that resistivity of porous *PETPh* relatively decreases after influence of gamma radiation as the result of taking place destruction. And after interaction of gamma radiation the taking place matching leads to the increase of physical interaction in boundary nano-particle –polymer and composite resistivity of *PETPh* relatively increases.

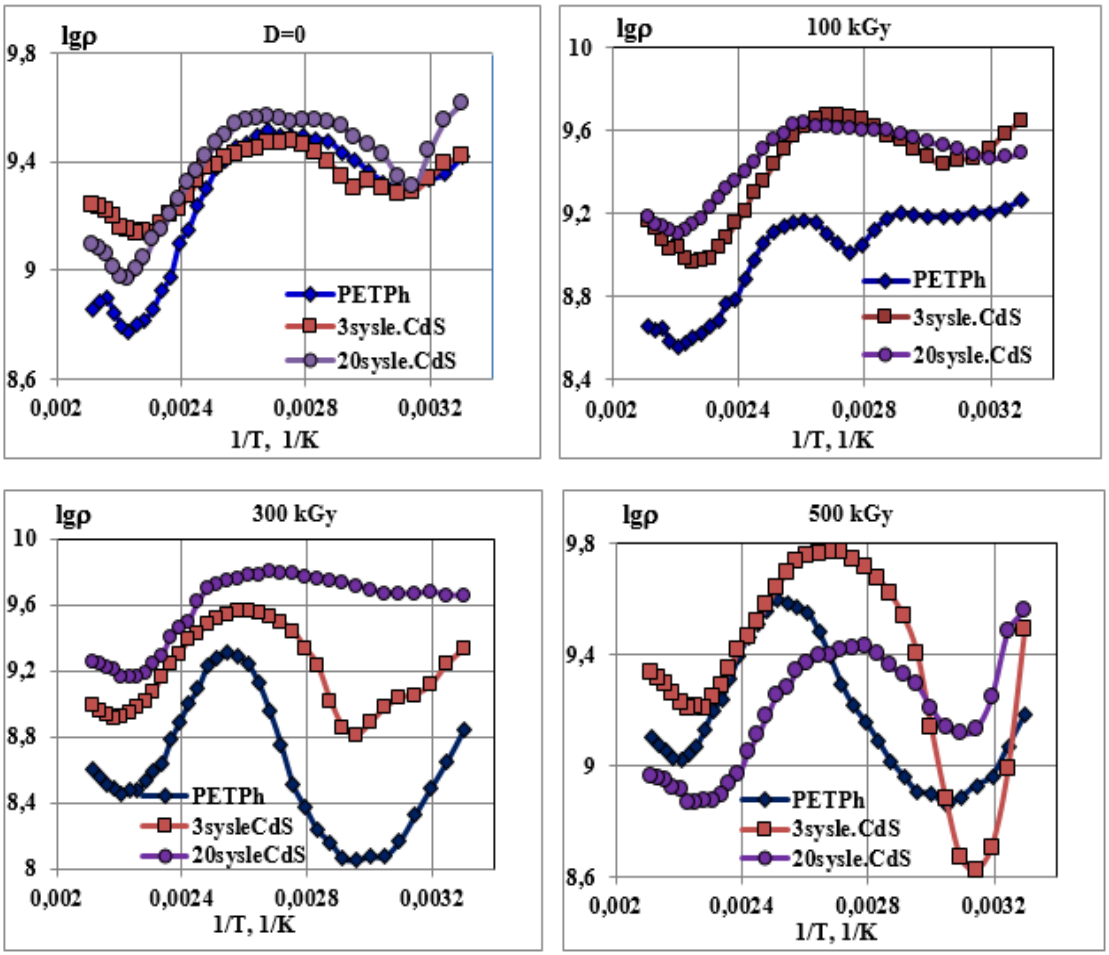

Fig.5. Temperature dependence of resistivity of initial and irradiated porous *PETPh* and *PETPh/CdS* composites on its base with different number of formation cycles.

[1] *J. Goldberger, He R., Y. Zhang.* Single-crystal gallium nitride nanotubes., Nature, 2003, vol. 422, pp. 599-602.

[2] *J.C. Hulteen, C.R. Martin.* A general template-based method for the preparation of nanomaterials., Journal of Materials Chemistry, 1997, vol.7, pp.1075-1087.

[3] *R.F. Khairutdinov.* Chemistry of semiconductor nano-particles., Chemistry successes, 1998, vol. 67, № 2, pp. 125-139.

[4] *A.A. Rempel.* The nano-technologies, properties and application of nano-structured materials., Chemistry successes, 2007, vol. 76, № 5, pp. 474-500.

[5] *B.P. Chandra, V.K. Chandra, P. Jha.* Luminescence of II-VI Semiconductor Nanoparticles., Solid State Phenomena, 2015, vol. 222, pp.1-65.

[6] *D. Denzler, M. Olschewski, K. Sattler.* Luminescence studies of localized gap states in colloidal ZnS nanocrystals., J. Appl. Phys., 1998, vol. 84, N 5, pp. 2841-2845.

[7] *R. Lozada-Morales, O. Zelaya-Angel, G. Torres-Delgado.* Photoluminescence in cubic and hexagonal CdS films., Appl. Surface Sci. 2001. vol. 175–176. pp. 562-566.

[8] *M. Hayne, B. Bansal.* High-field magneto-photoluminescence of semiconductor nanostructures, Luminescence. 2012. vol. 27. №3. pp. 179-196.

[9] *X. Sun, L. Xie, T. Wang, et. al.* Optical fiber amplifiers based on PbS/CdS QDs modified by polymers., Optics Express, 2013. vol. 21. №7. pp. 8214-8219.

[10] *B. Li, X. Zhang, L. Li et. al.* (2014). White luminescence from CdS nanocrystals under the blue light excitation. Journal of Solid State Chemistry, 2014. vol. 214. pp. 108–111.

[11] *E.V. Ushakova, T.K. Kormilina, M.A. Burkova et. al.* The Influence of Ligand Type on Self-Organization and Optical Properties of Cadmium Selenide Quantum Dots, Optics and Spectroscopy, 2017, vol. 122, №1, pp. 25–29.

[12] *I.A. Akimov, I.Yu. Denisuk, A.M. Meshkov.* Nano-crystals of semiconductors in polymer matrix are new optical mediums., Optics and

spectroscopy, 1992., vol. 72, № 4, pp. 1026-1032.

[13] *N.M. Ushakov, K.V. Zapsis, G.Yu. Yurkov et. al.* Optical Properties of Cadmium Sulfide Nanoparticles on the Surface of Polytetrafluoroethylene Nanogranules., Optics and Spectroscopy, 2006, vol. 100, № 3, pp. 414–418.

[14] *M.A. Zvaigzne, I.L. Martynov, V.A. Krivenkov et. al.* The Influence of the Quantum Dot/Polymethylmethacrylate Composite Preparation Method on the Stability of Its Optical Properties under Laser Radiation., Optics and Spectroscopy, 2017, vol. 122, №1, pp. 69–73.

[15] *A.A. Mashenzeva, B.N. Aubakirov, M.B. Zdorovetz, A.B. Rusakova, A.T. Akilbekov.* Some aspects of argenthum precipitation in channels of track membranes on PETPh base, Eurasia National University Buletin University named after L.N. Gumilyev, 2012, №2, pp.84-92.

[16] *E.Yu. Kanyukov, E.E. Shumskaya, M.D. Kutuzov D.B. Borgekov, I.E. Kenjina, A.L.Kozlovskii, M.V. Zdorovetz.* Ferromagnetic nano-tubes in pores of track membranes for the elements of flexible electronics., Devices and measurement techniques, 2017, vol. 8, №3, pp. 214–221.

[17] *A.M. Magerramov, M.A. Nuriyev, A.A. Shukurova.* Electret properties of nano-structured films of Teflon., Plastic masses, 2012, №10, pp.7-9.

[18] *A.M. Magerramov, M.A. Nuriyev, A.A. Shukurova.* On orientation of polyethylene irradiated films of low density and electric conduction of its compositions with nano-Cu_2S, Perspective materials, 2015, №5, pp.62-68.

[19] *M.A. Nuriev, A.M. Magerramov, A.A. Shukyurova.* Electrical Conductivity of Nanocomposites Based on Low-Density Polyethylene and Cu_2S Nanoparticles., Surface Engineering and Applied Electrochemistry, 2018, vol. 54, №1, pp. 32–37.

[20] *A.A. Shukurova, M.A. Nuriyev, A.I. Gasimova, I.M. Nuruyev, A.Sh. Mammadova.* The nano-composites on the base of crystal polymers and cadmium sulfide., Transactions, ANAS, series of phys-tech and math sciences, physics and astronomic, №5, 2021, pp.121-127.

[21] http://www.newchemistry.ru/material.php?id=40

[22] *S.S. Federova.* The modification of electro-physical properties of polyethylene terephthalate films by ion-plasma precipitation of nano-dimensional coverings on carbon base., PhD thesis, Moscow, 2005, p.153.

[23] *A.N. Georgibiani, M.K. Sheynkman.* Physics of the A_2B_6 compounds., M.: Science, 1986, pp.42–44.

[24] *S.A. Sadikhov, D.K. Palchayev, J.Kh. Murliyeva, M.N. Alikhanov, M.Kh. Rabadanov, S.Kh. Gadjimagomedov, S.N. Kallayev.* Ac-electric conduction of $BiFeO_3$ ceramics obtained by the method of spark plasma baking of nano-powder., Solid-state Physics, 2017, vol. 59, № 9, pp.1747-1753.

[25] *Yu.M. Poplavko, L.P. Pereverzeva, I.P. Raevski.* Physics of active dielectrics, Rostov-na Donu., 2009, pp162-164.

[26] *Shalini Kumari, N. Ortega, A. Kumar, S.P. Pavunny, J. W. Hubbard, C. Rinaldi, G. Srinivasan, J. F. Scott,* and *Ram S. Katiyar.* Dielectric anomalies due to grain boundary conduction in chemically substituted $BiFeO_3$, Journal of Applied Physics, 117, 114102, (2015), pp.1-13.

Received: 05.04.2022

BLUSHING OF PHASE TRANSITIONS $Y_{0,7}Cd_{0,3}Ba_2Cu_3O_{7-\delta}$ IN NTSC MATERIAL

V.M. ALIYEV, G.I. ISAKOV, V.I. EMINOVA, S.Z. DAMIROVA
Institute of Physics of the National Academy of Sciences of Azerbaijan,
AZ 1143, Baku, H. Javid Ave., 131
v_aliev@bk.ru, gudrat.isakov@gmail.com

The effect of substitution of Y for Cd on the mechanism of the formation of excess conductivity in $YBa_2Cu_3O_{7-\delta}$ polycrystals is investigated. With the substitution of Cd for Y, the resistivity ρ of the $Y_{0,7}Cd_{0,3}Ba_2Cu_3O_{7-\delta}$ sample increases noticeably, and the value of the critical temperature of the transition to the superconducting state (T_c) decreases.

It is shown that superconducting phase transitions (PTS) in them have a diffuse character. The parameters of the blurring of the FP are determined: T_0, *a*, L_0 (T), and dL_0 / dT. It was found that in $YBa_2Cu_3O_{7-\delta}$ HTSC material, partial substitution of Y for Cd atoms significantly reduces the PT region and increases dL_0 / dT.

Keywords: superconductivity, phase transition, Y0,7Cd0,3Ba2Cu3O7-δ, transition rate.
PACS: 74.25. Fy, 74.20.Mn, 74.72. ± h, 74.25. ± q, 74.25.Jb

INTRODUCTION

Although more than thirty years have passed since the discovery of high-temperature superconducting materials, their synthesis is an unsolved problem. The main disadvantages of traditional methods for obtaining HTSC materials are low rate, incomplete completion of the solid-phase reaction, as well as the complexity of directional formation of the real structure of the final material, which determines its structure-sensitive properties.

The study of phase transitions (PT) is one of the topical and studied areas of solid state physics. This is due to the close connection between PT and many branches of solid state physics. One of the topical issues is to identify the classification of the studied FP, to what extent it is blurred, and how it is possible to influence the degree of blurring. For this, it is necessary to determine the parameters of the phase transition, which makes it possible to judge the degree of its blurring. An analysis of the temperature dependences of the electrical properties of high-temperature superconductors near and in the region of the phase transition shows that the phase transitions in them are of a diffuse nature and this follows from the features of type-II superconductors. But the study of blurring issues near and in the FP region reveals the mechanisms leading to blurring, with the help of which one can judge the quality of the object under study. This is especially true for new modified HTSC materials. The first studies of PT smearing in HTSCs were performed for bismuth ceramics and a polycrystalline sample [1, 2]. The results were interpreted within the framework of the theory of diffuse phase transitions [3]; therefore, this work is devoted to the determination of the parameters of phase transitions blurring in $Y_{0,7}Cd_{0,3}Ba_2Cu_3O_{7-\delta}$ HTSC material.

EXPERIMENTAL RESULTS AND THEIR ANALYSIS

The synthesis of $YBa_2Cu_3O_{7-\delta}$ and $Y_{0,7}Cd_{0,3}Ba_2Cu_3O_{7-\delta}$ was carried out in two stages [4, 5]. At the first stage, the initial components in a stoichiometric ratio were mixed and annealed in air at a temperature of 1120 K for 25 h. At the second stage, the resulting compositions were annealed in oxygen (P = 1.2–1.5 atm) at a temperature of 1190 K for 25 h and slowly cooled to room temperature.

Samples with dimensions 8 × 4 × 3 mm were cut from compressed tablets (diameter 12 mm, thickness 3 mm) of the synthesized polycrystals. The electrical resistance was measured according to the standard four-probe scheme. The current contacts were created by applying a silver paste with the subsequent connection of silver wires 0.05 mm in diameter to the ends of the polycrystalline to ensure uniform current spreading over the sample. Potential contacts were also created, which were located on the surface of the sample in its middle part. Then, a three-hour annealing was carried out at a temperature of 200 ° C in an oxygen atmosphere. This procedure made it possible to obtain a contact resistance of less than 1 Ohm and to carry out resistive measurements at transport currents up to 10 mA in the ab-plane.

RESULTS AND ITS DISCUSSION

The temperature dependences of the resistivity ρ (T) = ρab (T) of the synthesized polycrystals $YBa_2Cu_3O_{7-\delta}$ (1) and $Y_{0,7}Cd_{0,3}Ba_2Cu_3O_{7-\delta}$ (2) are shown in Fig. 1. The ρ (T) dependences of the $YBa_2Cu_3O_{7-\delta}$ sample (Fig. 1) have a shape characteristic of optimally doped HTSCs. The linear course of the temperature dependence of the resistivity of samples Y1 and Y2 in the normal phase is well extrapolated by the expression $\rho n (T) = (\rho_0 + \kappa T + BT^2)$ (here B and k are some constants).

As seen from Fig. 1, the critical temperatures of samples Y1 and Y2 are T_c1 = 90.1K and T_c2 = 88K, respectively. In this case, the resistivity ρ (T) of the Y2 sample in the normal phase at 300 K in comparison with $YBa_2Cu_3O_{7-\delta}$ increases by almost 2 times. The critical temperature of samples Y1 and Y2 is T01 = 92.58K and T02 = 91.1K, respectively.

In papers [6-9], the questions of PT smearing in HTSC are investigated. It is shown that the

131, H.Javid ave, AZ-1143, Baku
ANAS, Institute of Physics
E-mail: jophphysics@gmail.com

determination of the PT parameters contributes to the identification of the law of the transition of the normal phase to the SC phase, the degree and region of its smearing, the influence of the magnetic field and various types of defects in ceramic samples. This becomes possible if the exact temperature of the FP-T_0, the temperature constant of the FP-a, the phase distribution function – L_0 (T) and the temperature rate of the FP-dL_0/dT are determined from the experimental data. The method for determining these parameters is based on the theoretical model of the RFP [3] and is described and tested in detail in [1, 2, 6-9].

The theory of diffuse phase transitions (RFP) in condensed systems is based on the introduction of the switch-on function L (T). It is assumed that if the thermodynamic potentials of the α and β-phases are denoted by Φ_α and Φ_β, then the total thermodynamic potential in the region of coexistence of the phases Φ (T) can be represented as:

$$\Phi(T)= \Phi_\alpha(T)-\Delta\Phi(T).L(T) \quad (1),$$

where its change is $\Delta\Phi$ (T) = $\Phi\alpha$(T) - $\Phi\beta$ (T). When FP occurs in the interval $\Delta T = T2-T1$ (T2> T1), the switching function L must satisfy the conditions

$$L_0(T)= \begin{cases} 0 & T < T_1 \\ 0 < L < 1 & T_1 < T < T_2 \\ 1 & T > T_2 \end{cases} \quad (2)$$

According to the theory of the RFP, for L (T) in the zeroth approximation it was obtained

$$L_0(T)= \frac{1}{1+exp[a_0(T-T_0)]} \quad (3)$$

Taking into account that L0 (T) characterizes the relative fraction of phases in the region of their coexistence, it can be represented in a simple form

$$L_0(T)=\frac{m_\beta(T)}{m_\alpha(T)+m_\beta(T)}=\left[1+\frac{m_\alpha(T)}{m_\beta(T)}\right] \quad (4)$$

where mα and mβ are the masses of the α and β phases. From the joint solution of (3) and (4) it is obtained that

$$a = (T_0-T)-1.\ln m_\alpha/m_\beta \quad (5)$$

Since and is a constant, the factor $\ln(m_\alpha/m_\beta)$ in (5) must be a linear function of temperature. Therefore, from the temperature dependence of $\ln(m_\alpha/m_\beta)$, the temperature PT = T_0 is determined. The most informative is the derivative L_0 (T) with respect to temperature, which expresses the temperature rate of phase transformations of each phase:

$$\partial L/\partial T = -\frac{a}{2}\cdot\frac{1}{1+ch[a_0(T-T_0)]} \quad (6)$$

To quantitatively characterize the blurring of the PT, one can the half-width of the dL0/dT curve, i.e. temperature range

$$2\Delta T^*= -3{,}52/a. \quad (7)$$

In the case of superconductors, if the normal phase (n.f.) is taken as one phase, and the superconducting phase (s.p.f.) is taken as the other, then the proposed method can be applied to HTSC as well. Then the corresponding masses will take the value of mn and ms and they should be determined from the changes in the physical characteristics in the region of the SP FP. In this case, they are determined from the data ρ (T). From the temperature dependence ln (m_n / m_s), the temperature FP-T_0 (the point of intersection of straight lines with the abscissa axis) was found, and from the slope $\Delta\ln$ (m_n / m_s) / ΔT (tangent of the angle) the temperature constant a (Fig. 2).

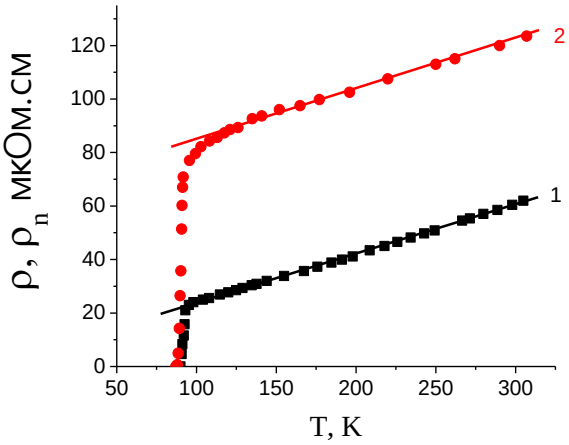

Fig. 1. Temperature dependences of the resistivity of the samples: 1- $YBa_2Cu_3O_{7-\delta}$, 2- $Y_{0,7}Cd_{0,3}Ba_2Cu_3O_{7-\delta}$. The straight lines represent $\rho_n(T)$, extrapolated to low temperatures.

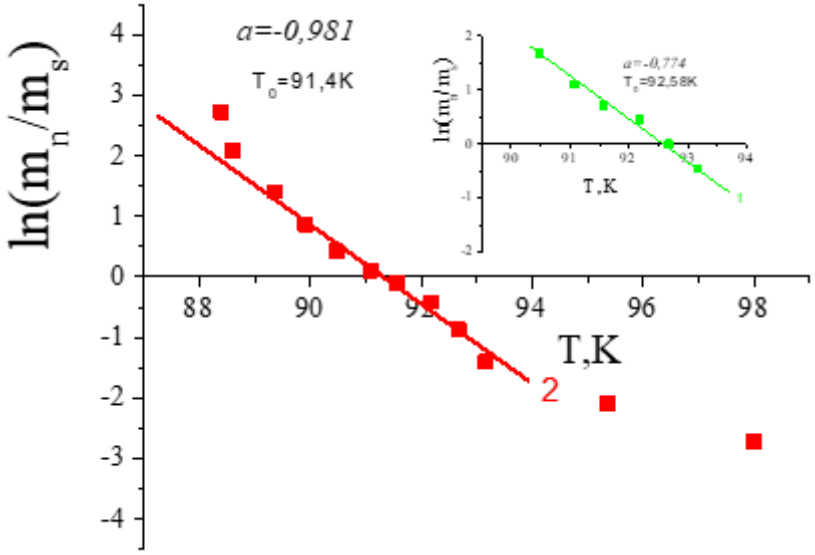

Fig. 2. Temperature dependences $\ln(m_n/m_s)$ for samples: 1- $YBa_2Cu_3O_{7-\delta}$, 2- $Y_{0,7}Cd_{0,3}Ba_2Cu_3O_{7-\delta}$.

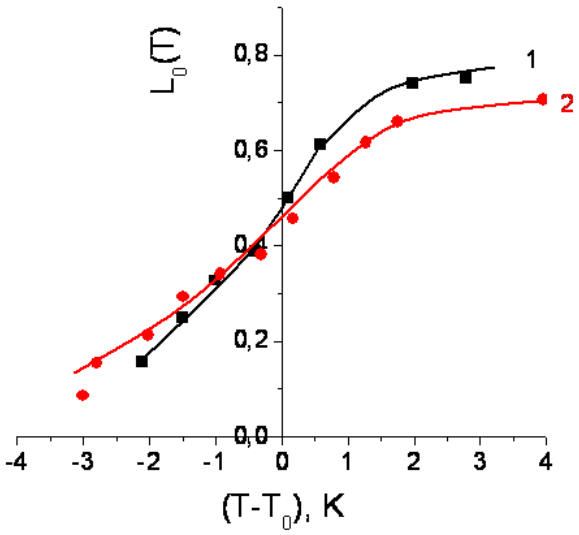

Fig. 3. Temperature dependences of the switch-on function L (T) for samples: 1- $YBa_2Cu_3O_{7-\delta}$, 2- $Y_{0,7}Cd_{0,3}Ba_2Cu_3O_{7-\delta}$.

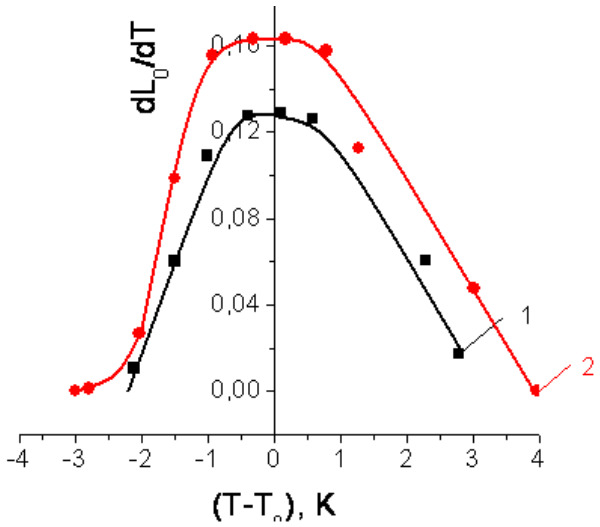

Fig. 4. Temperature dependences of the derivative of the switch-on function dL / dT for samples: 1- $YBa_2Cu_3O_{7-\delta}$, 2- $Y_{0,7}Cd_{0,3}Ba_2Cu_3O_{7-\delta}$.

These parameters made it possible to calculate the temperature dependence L_0 (T) using formula (3) (Fig. 3), and using (6) dL_0 / dT (Fig. 4). The results of calculations showed that with partial substitution of cadmium for yttrium in Y-Ba-Cu-O, the indicated PT parameters change, i.e. for $YBa_2Cu_3O_{7-\delta}$ SP material T_0 = 92.58K, *a*= -0.774, L_0 (T) = 0.5 and dL_0 / dT = 0.128, and for $Y_{0,7}Cd_{0,3}Ba_2Cu_3O_{7-\delta}$ was T_0 = 91.4K, *a* = -0,981, L_0 (T) = 0.44 dL_0 / dT = 0.162. Note that with the substitution of Cd for Y, the degree of blurring calculated according to equation (7) decreases and for Y1 and Y2 is 2.27K and 1.79K, respectively. In this case, the rate of phase transformations (dL_0 / dT) of sample Y2 in comparison with Y1 increases 1.26 times. Thus, we can conclude that the quality of yttrium ceramics improves upon partial substitution of Y atoms for Cd atoms. It can be assumed that, in this case, the concentration of defects decreases.

CONCLUSION

Studies and analyzes have shown that the substitution of Cd for Y leads to a slight decrease in the critical temperatures of the $Y_{0,7}Cd_{0,3}Ba_2Cu_3O_{7-\delta}$ sample in comparison with $YBa_2Cu_3O_{7-\delta}$ (respectively, T_c1 = 90.1K and T_c 2 = 88K). In this case, the resistivity ρ (T) of the Y2 sample in the normal phase at 300 K in comparison with $YBa_2Cu_3O_{7-\delta}$ increases by almost 2 times.

It is shown that superconducting phase transitions (PTs) in them have a diffuse character. The parameters of the blurring of the FP are determined: T_0, a, L_0(T), and dL_0/dT. It was found that the degree of smearing (ΔT*) of the $Y_{0,7}Cd_{0,3}Ba_2Cu_3O_{7-\delta}$ sample upon the substitution of Cd for Y in the Y–Ba–Cu – O system decreases three times.

[1] *S.A. Aliev, S.S. Ragimov, V.M. Aliev.* Transactions of ANA of sciences physics and astronomy. 2001, 2.5, p. 67-71.
[2] *S.A. Aliev, S.S. Ragimov, V.M. Aliev.* Azerbaijan Journal of Physics. 2003, 3-4, p. 30-34.
[3] *B.N. Rolov*. "Blurred phase transitions". Riga, 1972, p. 311.
[4] *S.A. Aliev, S.S. Ragimov, V.M. Aliev.* Azerbaijan Journal of Physics, 2004, 10, 4, p.42-43.
[5] *V.M. Aliev, R.I. Selimzade, J.A. Ragimov et al.* Physics of low temperatures, 2020, 46, 9, p. 1068–1077.
[6] *S.A. Aliyev.* Azerbaijan Journal of Physics. 2002, 8, 4, p. 32-36.
[7] *V.M. Aliev.* Transactions of ANA of sciences physics and astronomy. 2010, 30, 2, p. 59-63.
[8] *V.M. Aliev.* Transactions of ANA of sciences physics and astronomy. 2011, 31, 2, p. 113-117.
[9] *S.A. Aliyev.* "Blurring of phase transitions in semiconductors and high temperature superconductors", Baku: publishing house "science", 2007, p. 286.

Received: 26.04.2022

FREQUENCY DEPENDENCE OF ELECTRIC CONDUCTION OF POLYETHYLENE OF HIGH DENSITY/ α-Al_2O_3 NANO-COMPOSITES MODIFIED BY GAMMA BEAMS

M.N. BAYRAMOV, N.Sh. ALIYEV
Institute of Radiational Problems of Azerbaijan NAS, Az 1143,
B.Vakhabzade, 9, Baku,Azerbaijan
nabi.aliyev.1958@ mail.ru

The frequency dependence of electric conduction of initial and γ-irradiated HDPE (polyethylene of high density)/ α-Al_2O_3 nano-composites are investigated in the given work. It is shown that absorption doze of gamma-radiation significantly influences on composite sample electric conduction causing its increase in the direction of high frequencies and this increase connects with accumulation of stabilized charge carriers in irradiated materials. It is established that influence of irradiation dose 100kGy on nano-composite electric conduction is caused by not the change of molecular motion spectrum, but the accumulation of stabilized charge carriers in the samples and at least the radiolysis molecular products presenting the trapping centers. The relatively rapid increase of electric conduction real part at alternating current σ_{ac} (ν) on frequency dependences of HDPE/α-Al_2O_3 nano-composite samples with volume content correspondingly 1,3% and 5% with heterogeneous structure is caused by electron polarization where charge transfer probably takes place with the help of hopping conduction. The values found for *s* index (from 0,081 up to 0,43) in irradiated nano-composite samples are also indicate on this fact.

Keywords: polyethylene of high density, nano-dimensional aluminum oxide, electric conduction, electric conduction real part, irradiation dose, polarization.
PACS: 61.80Ed;72.80.Tm;72.80.Le

INTRODUCTION

Nowadays, the formation of multifunctional polymer compositional materials (PCM) on the base of nano-dimensional fillers from different metal oxides (Fe_2O_3, Fe_3O_4, TiO2, Al_2O_3, ZnO, CuO, BeO, ZrO_2 and etc.) is the one of the perspective directions of the radiational material science. Note that the structure and properties of nano-and low-dispersed fillers of inorganic origin including polymer composites modified by Al_2O_3 significantly change because of interphase interactions and nano-layer formation near the boundary of polymer with filler particles. By other hand, the properties of polymer composites also depend on the nature of polymer matrix and filler, their initial properties, form and filler sizes, and also on interaction and adhesion between polymer matrix and filler [1,2].

The prediction and taking under consideration of external factor influence (external electric field, magnetic field, temperature, humidity, pressure, ionizing radiation and etc) are ones of the important and key questions at PCM production which are applied in different devices and installations. That's why investigators working in this field pay significant attention to availability of again developed many-functional PCM in radiation field. These materials should be stable to high radiational action and have the minimum dependence on the change of environment properties. By other hand, the study of PCM radiational modification process is also the interest for electron, cable and electro-technical industry. Thus, in cable production the lifetime of cable materials modified by ionizing radiation is bigger in several times [3,4]. It is need to note that PCM stability to radiation, heating and also the fact that it has the less dielectric losses is the main condition of its obtaining.

The investigation of electric conduction of YSPE/α-Al_2O_3 nano-composites modified by gamma-irradiation is the aim of the given work.

EXPERIMENTAL PART

The nano-composite samples HDPE/α-Al_2O_3 on the base of HDPE homogeneous mixture of mark 20808-024 by GOST 16387-85 with powder-like nano-dimensional aluminum oxide α-Al_2O_3 («Skyspring Nanomaterials, Inc.», USA) are prepared in the form of films by thickness 130-200 μm and diameter 20 mm by the way of hot pressing on hydraulic press at temperature 413-423K and pressure 15MPa with the following their hardening of mixture ice-water. In composite the filler mass relation is 1,3% and 5%.

The powder-like HDPE (20808-024 mark, average molecular weight is 95000, crystallinity degree is 52%, melting point is T = 403K, density is d = 0,93 gr/cm^3, resistivity is $\rho_v = 1 \cdot 10^{16}$ Om·cm 20-40) taken as a polymer matrix is mixed in porcelain cup with nano-α-Al_2O_3 filler powder (density is d = 4,4 gr/cm3, average dimension is 50 nm, resistivity is $\rho_v = 1 \cdot 10^{12}$ Om·cm) in the beginning stage of works for the obtaining of

HDPE/α-Al_2O_3 nano-composite. The nano-composite samples by thickness 130-200μm and diameter 20mm, are obtained from this homogeneous mixture on hydraulic press at pressure 15MPa at temperature 423K with ageing during 5 min, which further are cooled at 273K (ice-water mixture). The filler volume content in composite is 1,3% and 5%.

The frequency dependences of σ(ν) electric conduction of HDPE/α-Al_2O_3 nano-composite in alternating field are measured with the help of impedance measurer E7-20 in frequency interval 25-10^6 Hz at temperature 293K.

131, H.Javid ave, AZ-1143, Baku
ANAS, Institute of Physics
E-mail: jophphysics@gmail.com

The composite film samples are treated by γ-radiation at room temperature in installation with irradiation source ^{60}Co. The absorbed dose rate is $3{,}3\cdot10^{3}$ Gy/h.

RESULT DISCUSSION

The frequency dependences of electric conduction logarithmic values of HDPE/α -Al_2O_3 lqσ=f(lqν) nano-composite samples before irradiation, are shown in Fig.1.

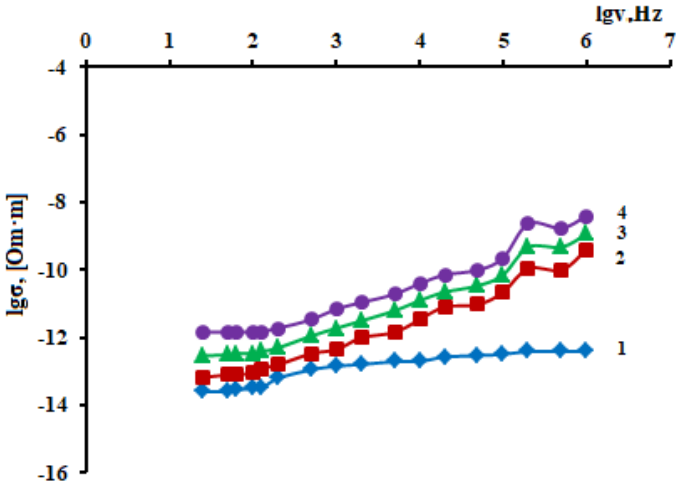

Fig.1. The frequency dependences of logarithmic values of HDPE/α- Al_2O_3 lgσ = f (lgν) nano-composite electric conduction before irradiation: 1 is pure HDPE; 2 is content of 1vol.% nano- α-Al_2O_3; 3 is content of 3vol.% nano-α- Al_2O_3; 4 is content of 5vol.% nano-α- Al_2O_3.

The frequency dependences of electric conduction (Fig.1 and Fig.2) in investigated HDPE/ α -Al_2O_3 nano-composites as heterogeneous structures according to law of universal dielectric response are described by Jonsher power law [9]:

$$\sigma(\omega) \approx \sigma_{dc} + A\,\omega^{s}$$

where σ_{dc} is electric conduction at constant current not depending on frequency, circular frequency $\omega = 2\pi\nu$; A and s are coefficients depending on temperature and frequency. The power frequency dependence σ(ω) shows the hopping conduction in these systems. Value s also defines the charge carrier motion type. The value of frequency index s we calculate from curve inclination of the dependence $\ln\sigma_{ac} = f(\ln\nu)$, where $0 < s = 0{,}081 \div 0{,}43 < 1$.

As it is seen from Fig.1, the three regions of electric conduction change values (curves 2 – 4) are observed for unirradiated HDPE/ α -Al_2O_3 nano-composites; two regions are observed for HDPE polymer (curve 1): I region is observed at frequency (25-120) Hz, II region is observed at $(200\text{-}5\cdot10^{4})$ Hz and III region is observed at frequency $(2\cdot10^{5}\text{-}10^{6})$ Hz.

The linear increase of electric conduction of all samples with frequency increase are character for I and II regions. Herewith, electric conduction value increases with the increase of filler content. At low frequencies (I region) on alternating voltage the insignificant change of (σ_{ac}) electric conduction in the dependence on frequency can be explained by the interphase polarization (Maxwell-Vagner polarization) caused by trapping of volume charges in interphase and polar elements forming as a result of sample partial oxidation at thermal pressing [31]. The voltage applied to the sample in this region transfer the system charge carriers in big distances and σ_{ac} electric conduction dominates in the given region. Here, the frequency increase leads to the decrease of average distance of charge carrier transfer and electric conduction real part changes according to $\sigma_{ac}(\nu) \sim \nu^{0{,}48}$ law after the fact that the frequency achieves the definite value ν_c.

The corresponding values calculated for the inclination of $\lg\sigma_{ac} = f(\lg\nu)$ dependence linear sections show that s parameter depends on filler volume concentration and increases with the increase of Al_2O_3 filler concentration in polymer matrix. In I region s_1 decreases from 0,43 up to 0,081, s_2 decreases from 0,37 up to 0,18 that well coincides with results obtained in [14]. The found values of s parameter (from 0,081 up to 0,43) shows on the fact that the rebound conduction is the near-wall mechanism [10, 13]. According to this model, the electric conduction frequency dependence can be explained as charge carrier jumps $\sigma_{ac}(\nu)$ on localized levels round Fermi levels [5,6,7,8].

At low frequencies the insignificant increase of electric conduction values is observed in I region in the polymer pure sample (curve 1), linear increase of electric conduction values is observed in II and III regions. The electric conduction significantly increases with the increase of filler volume concentration to the direction of high frequencies in samples of HDPE/α -Al_2O_3 nano-composites. Note that electric conduction maximums in frequency range $2\cdot10^{5} \div 10^{6}$ are observed on resonance frequency.

The frequency dependences of logarithmic values of electric conduction of HDPE/α -Al_2O_3 nano-composite samples lqσ=f(lqν) after γ-irradiation by dose D=100kGy are shown in Fig.2.

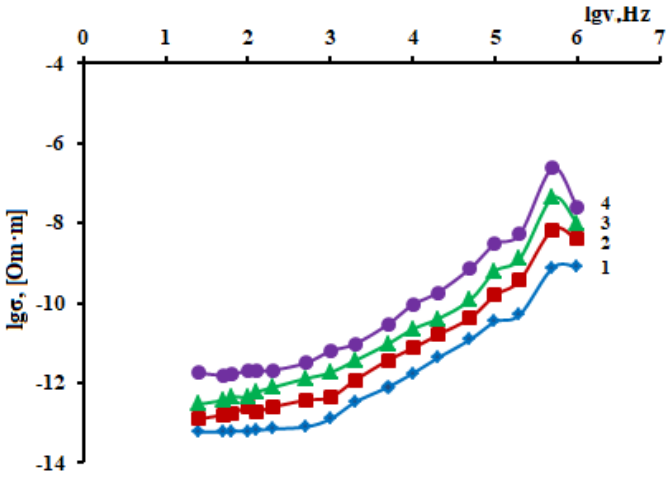

Fig.2. The frequency dependences of logarithmic values of HDPE/α- Al_2O_3 lgσ = *f* (lgv) nano-composite electric conduction after γ-irradiation by dose 100kGy: 1 is pure HDPE; 2 is content of 1vol.% nano- α-Al_2O_3; 3 is content of 3vol.% nano-α- Al_2O_3; 4 is content of 5vol.% nano- α- Al_2O_3.

As it is seen from the Fig.2 the value change character of electric conduction in all regions is identical one on $\ln\sigma_{ac} = f(\ln\nu)$ dependences after γ-radiation by dose D=100kGy of polymer sample and nano-composites containing 1,3 and 5 vol.% of nano-α -Al_2O_3.

The three regions of electric conduction value changes lgσ: I region at frequency 25 – 200 Hz, II region at frequency $(5\cdot10^2\text{-}5\cdot10^4)$Hz and III region at frequency $(1\cdot10^5\text{–}10^6)$ Hz, are observed in the comparison with unirradiated samples. At influence of γ -radiation the electric conduction values of polymer and nano-composite samples increase with the increase of nano- α -Al_2O_3 content in the comparison with analogous unirradiated samples [15,15].

The relatively rapid $\sigma_{ac}(\nu)$ increase is caused by electron polarization with the frequency increase [6,11]. As a rule, the presence of the linear sections on $\ln\sigma_{ac} = f(\ln\nu)$ dependence for heterogeneous system in which HDPE/α -Al_2O_3 nano-composites investigated by us are included, shows the hopping of charge transfer.

CONCLUSION

The study of frequency dependences $\lg\sigma = f(\lg\nu)$ in frequency interval 25 - 10^6 Hz shows the presence of the two linear regions with higher values of γ-irradiated samples by dose 100kGy than unirradiated samples have which change according to law $\sigma_{ac}(\nu) \sim \nu^{0,43}$. The change character of the electric conduction values in all regions is identical one. The electric conduction values of HDPE/α -Al_2O_3 nano-composites increase with the increase of volume content of nano- α -Al_2O_3 on frequency dependences.

The relatively rapid increase of conduction real part at alternating current σ_{ac} (ν) in frequency dependencies of HDPE/α -Al_2O_3 nano-composite samples after γ-irradiation by dose 100kGy is caused by electron polarization where charge transfer takes place probably with the help of conduction hopping.

[1] *O.S. Gefle, S.M. Lebedev, Yu.P. Pokholkov.* Frequency spectrums of complex dielectric constant of composite dielectrics on the base of polyvinylchloride, Bulletin of the Tomsk Technical University, 2007, vol.310, №1, pp.87-91.

[2] *T. Tanaka.* Dielectric nanocomposites with insulating properties. IEEE Trans. Diel. Electr. Insul. 2005, v.12, No5, p.914-918.

[3] *A.M. Magerramov, M.M. Kuliyev, R.S. Ismayilova, E.G. Gadjiyeva.* The influence of γ-irradiation on composite electrophysical properties on the base of polyethylene with CdS/ZnS inclusions. Theses of 9th International Conference "Nuclear and radiational physics", September, 24-27, 2013, Almaty, Kazakhstan.

[4] *A.M. Magerramov.* Structural and radiational modification of electret, piezoelectric properties of polymer composites, Baku: Science, 2001, p.327.

[5] *O.S. Gefle, S.M. Lebedev, Yu.P. Pokholkov.* Frequency spectrums of complex dielectric constant of compositional dielectrics on the base of polyvinylchloride, Bulletin of the Tomsk Technical University, 2007, vol.310, №1, pp.87-91.

[6] *M.A. Kudrashov, A.I. Mashin, A.A. Logunov, G. Chidichimo, G. DeFilpo.* Dielectric properties of nano-composites Ag/PAN, JTPh, 2014, vol.84, в.7, pp.67-71.

[7] *A.A. Ormont, I.P. Zvyagin.* The peculiarities of frequency dependence of the electric conduction of disordered semiconductors in the region of transfer change mechanism, PhTS, 2015, vol. 49, № 4, pp.449-452.

[8] *N.Sh. Aliyev, M.M. Guliyev, A.M. Maharramov, R.S. Ismayilova.* Features of Electrocon-

ductivity of γ-Irradiated Composites in Heating-Cooling Conditions. American Journal of Physics and Applications. February 28, 3(2), 2015 p.15-20

[9] *Jonscher, K. Andrew.* "The 'universal' dielectric response". Nature. 267 (5613): 673 (1977).

[10] *S. Barrau, P. Demont, A. Peigney, C. Laurent and C. Lacabanne.* DC and AC Conductivity of Carbon Nanotubes-Polyepoxy Composites.Macromolecules, 2013, v.36, №14, pp.5187-5194.

[11] *H.J. Jafar, N.A. Ali and A. Shawky.* Study of AC-Electrical Properties of Aluminum-Epoxy Composites. J. of Al-Nahrain University, 2011, v.14, №3, pp.77-82.

[12] *Li Yu Chao, Li Robert Kwok Yiu and Sie Chin Tjong.* Frequence and Temperature Dependences of Dielectric Dispersion and Electrical Properties of Polyvinylidene Fluoride/Expanded Graphite Composites.Jour. of Nanomaterials, v.2010, Article ID 261748, 10 pages.

[13] *V. Tommer, G. Polizos, C.A. Randall and E. Manias.* Polyethylene nanocomposite dielectrics: İmplications of nanofiller orientation on high Polymer Science, 2012, 2(6), pp.135-140.

[14] *R.H. Young, J.J. Fitzgerald.* Effect of Polar Additives on Dielectric Properties and Charge Transport in a Moleculrly Doped Polymer: A Test of Dielectric Polarization Models. J.Cem.Phys. 1995, 102(15) 6290-6300.

[15] *V.V. Gromov.* Physicochemical processes at dielectric polarization, journal of Physical Chemistry ,2005, vol.79, pp.121-125.

[16] *A.P. Tyutnev, V.S. Sayenko,E.V. Smirnov, Yu.V. Pojidayev.* Radiational electric conduction of polymer at long-term exposure. High Energy Chemistry, 2006, vol. 40, №5, pp. 364-375.

Received: 26.04.2022

QUANTUM DOTS DYE-SOLAR CELLS SENSITIZED: A REVIEW

B. EMDADI[2], A. ASIMOV[1, 2], F. TATARDAR[1, 2]
[1]Institute of Physic of Azerbaijan National Academy of Science, AZ-1143, 131, H. Javid ave., Baku, Azerbaijan
[2]Institute of Physics & Electronic of Khazar University (Neftchilar Campus), AZ-1096, Khazar University 41 Mahsati Str., Baku, Azerbaijan
Corresponding author: emdadi.babak2021@khazar.org

An excellent utilization amount of fossil vigor has led to the crisis of energy as well as the surroundings. Thus, it is an immediate duty to research renewable scavenging energy to dissolve these issues. Among them, solar energy is reliable to be the most promising renewable energy resource due to its fascinating properties such as being inexhaustible and environmentally friendly. the growth of solar cells is already in the third stage, and investigation focuses contain dye-sensitized solar cells. Dye-sensitized solar cells make use of a similar sense, and light to electric power transformation efficiencies above 10% have been reached with DSCs. Quantum dots-sensitized solar cells have been broadly investigated and display promise for the improvement of the subsequent generation of energy, due to the specifications of small expense, environmental defense, and better theoretic vigor transformation efficiency. Quantum dot-sensitized solar cells (QDSCs) have appeared as a promising candidate for subsequent-generation solar cells due to the preferable optoelectronic aspects of quantum dot (QD) light-harvesting materials, such as high light, thermic, and moisture consistency, high absorption coefficient and solution processability as well as their easy construction and low-cost accessibility.

Keywords: Dye-Sensitized Solar Cells, Solar Cells, Quantum dots, Renewable energy, solar energy
PACS: 65.80 Ck 61.48 Gh 63.37 Hk

1. QUANTUM DOTS

Quantum dots are small nanocrystals that shine when exhilarated by outdoors originals, for instance, bright (UV) glory [1]. Employed Quantum Dots (QDs) can be built by utilizing a domain of materials; indeed, the majority of the regular materials synthesize zinc sulfide, lead sulfide, cadmium selenide, and indium phosphate. A striking number of promising applications for quantum specks will see them utilized intranet the human fame [1].

At the spot when the electron comes back to its lower and permanent express, this further vitality is transferred as glory relating to a particular recurrence. Quantum dots work analogously however a Quantum dots valuable stone goes about as one extensive particle. The important provenance used to motivate a quantum spot is generally vivid light. The recurrence or shadow of light eradiated isn't recognized with the material used in the quantum spot, however by the gamut of the quantum particle.

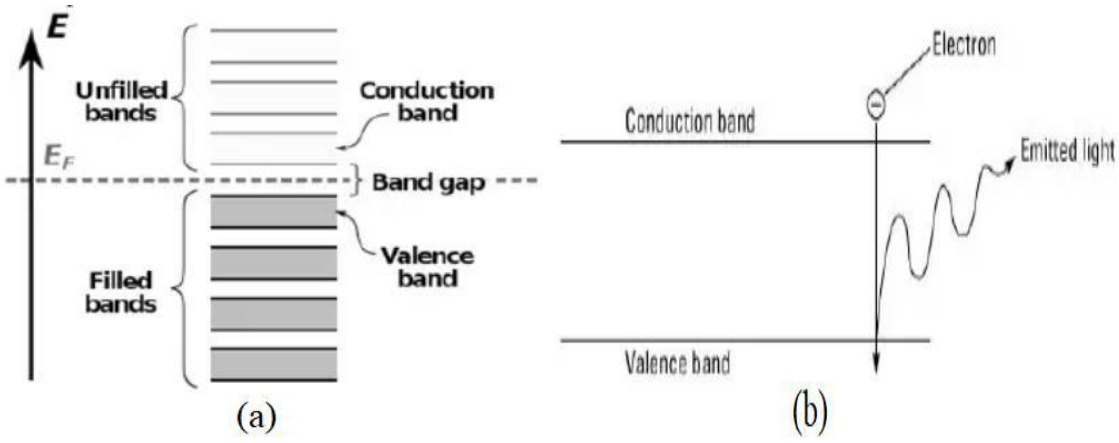

Fig. 1. (a). Band Gap, (b). Electron Transmition.

We have to say these prominent points about the quantum dots' size and color relationship, these kinds of dots release light with a high wavelength and tiny Quantum dots build light with little wavelengths [1]. As far as shading in the substantial span, this indicates extensive Quantum dots make red light, and small Quantum dots hand over blue light–sizes in the middle of record for the several colors in the span. By unifying the scope of measures of Quantum dots in an analogous instance, the total light span can be delivered at an equal time and shows up as white light.

131, H.Javid ave, AZ-1143, Baku
ANAS, Institute of Physics
E-mail: jophphysics@gmail.com

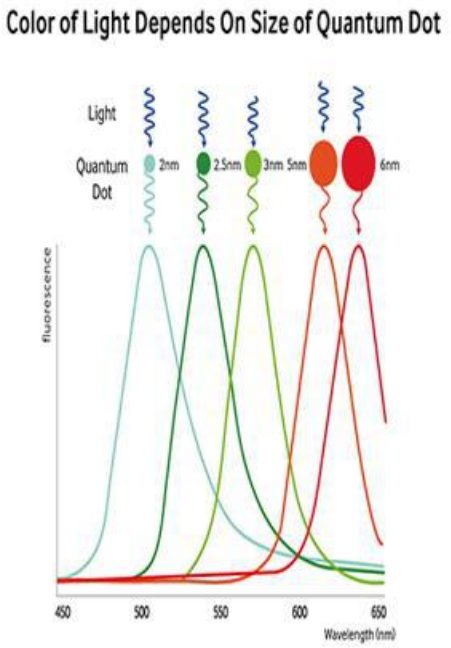

Fig. 2. Quantum dots size and color.

The evacuation of wavelengths of QDs spans from the explicit (UV) to the infrared (IR). QDs are promising for light emerging tools and may boost the performance of light-producing diode(LED), prompting the novel structure of "Quantum Dot light Emitting Diode". QDs are phenomenally useful for representing tools contemplating their kind optical attributes. They are equipped for introducing clearly more accurate and special colors. An evidence-of-idea QDs display has been effectively completed from specialized standpoint years prior and shows a decent performance and shining phenomenon in the region of doubtless and close infrared span. QDs depict copious fascinating optical and electronic attributes. In the current days, QDs are being progressed in an extensive span of applications (e.g., recognition of the illnesses, solitary protein tracking, medicine delivery, intracellular and therapy) [2]. QDs have wide utilization in clinical applications owing to their measure and attributes. Furthermore, in as much as the excellent characteristics of QDs, including physical, optical, and exciting electrical attributes, they are applied in other applications such as diagnostics, bio-imaging, tissue engineering, cancer therapy, photo-thermal treatment, biosensing, bioterrorism inhibition, and especially drug delivery [3]. QDs are considered excellent volunteers in the improvement of luminescent and electrical searches due to their benefits resulting from their little measure and unique physicochemical attributes [4]. The attributes of QDs can be summarized in three major and prominent sections expressed in the appendix list:

1. QDs have a wider stimulation spectrum resulting in using a sole light source to stimulate multicolor QDs. Also, a thin sharp publication summit decreases spectral overlap [5].
2. The remarkable disagreement among the attraction and transpiration wavelengths of QDs, the Stokes switch, lets collecting the full of publication spectra by segregating the QDs fluorescence signal from the background auto-fluorescence, ameliorating the sensibility of detection. This is a necessary factor for imaging tissue, mainly in formalin-fixed and paraffin-embedded tissue specimens due to their great background auto-fluorescence [6].
3. Compared to organic dyes, QDs have a lengthy fluorescence lifetime (about 10 to 40 ns) due to the mineral combination of QDs, more radiant publication, and superior signal-to-noise proportion. QDs brightness is about 10 to 20 times superior in comparison to the only organic fluorophores molecules [7].

2. SOLAR CELLS APPLICATION

Energy is a fundamental subject and problem that all generations should be confronted with at present and in the future [24]. For decades, emerging of novel systems and technologies to produce, supply, and usefully use solar power has been a persuasion to study recent procedures for the generation of pure power. Sun is a full, secure, inexpensive, and clean provenance of the vigor that can be straightly altered to electricity without generating contamination and environmental difficulties. An excellent utilization amount of fossil vigor has led to the crisis of energy as well as the surroundings. Thus, it is an immediate duty to research renewable scavenging energy to dissolve these issues. Among them, solar energy is reliable to be the most promising renewable energy resource due to its fascinating properties such as being inexhaustible and environmentally friendly. A solar cell is an electronic system that straightly changes sunlight into electricity. glory righting on the solar cell products both a current and a voltage to produce electric energy. This procedure needs in the first step, a material in which the attraction of light increases an electron to a superior vigor case, and secondly, the motion of this premier force electron from the solar cell into an outer circuit.A diversity of solar cells have been improved and sections of them have been realized the industrial production. usually, solar cells can be organized into three generations according to the materials and technological improvement [25, 26].

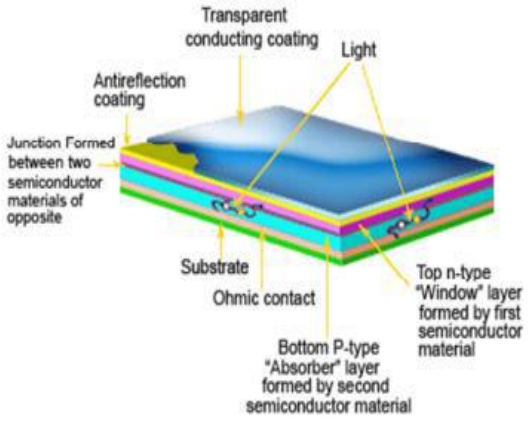

Fig. 3. Structure of thin film solar cells.

The prominent usage of solar energy is solar photovoltaic transformation, which is meant by the transformation of solar energy into electrical vigor using solar cells. Due to some important errors in crystalline silicon solar cells, people started to check thin-film solar cells, and so solar cells entered the second phase of expansion. Thin-film solar cells use materials with a great molar absorptivity and straight energy band structure (Figure. 2).

The benefits of these thin-film solar cells are their small thickness, low-cost [7].

Now, the growth of solar cells is already in the third stage, and investigation focuses contain dye-sensitized solar cells (DSSCs), polymer solar cells, perovskite solar cells, and quantum dot solar cells. As shown in Figure 3, it demands three substantial steps to transform sunlight into electricity: recently, the third race solar cells mostly contain dye-sensitized solar cells (DSCs), organic/polymer solar cells (OSCs), perovskite solar cells (PSCs), and quantum dot (QD) based solar cells [12-20]. In the previous two decades, third-generation solar cells have absorbed great investigation concern and undergone rapid progress (Figure. 4).

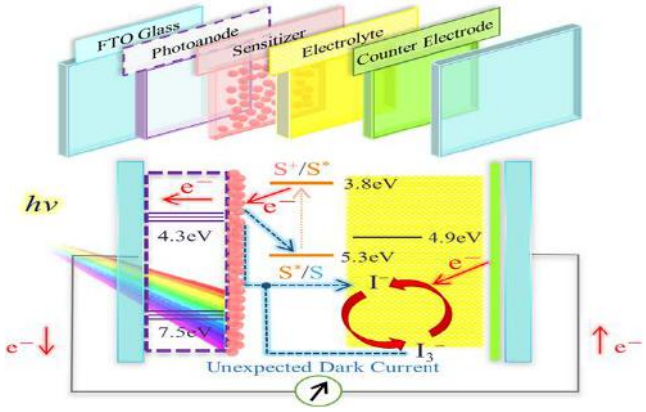

Fig. 4. Structure and schematic diagram of charge transfer in dye-sensitized solar cells.

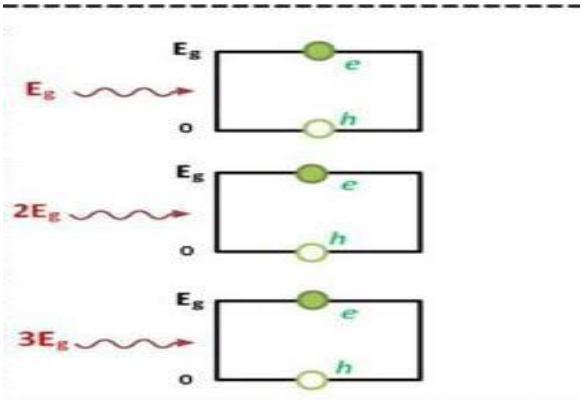

Fig. 5. Schematic illustration of the generation of carriers under the excitation of photon energy traditional solar cell.

The utilization of solar vigor is boosting in homes as well. Residential appliances can easily use electricity generated through solar power. Besides this solar energy is running solar stoves to reserve hot water in residential places. In many places, solar energy is used for ventilation targets. It aids in running bath fans, floor fans, and ceiling fans in houses. Fans run mostly every time in a building to control humidity and odor and in homes to take the warmth out of the galley. It is possible to increase a serious amount of utility bills, to decrease these bills solar energy is used for ventilation aims. subsequent-generation solar cells are possibly unlimitedly more helpful thanks to a recently discovered nanotube structure able of carrying electrical charges 100 million times more than precedent measured. The majority of solar cells recently use silicon to suck up light, however, inefficiencies in the material have led erudite to foster carbon nanotubes that can be implemented to boost the light attraction abilities of common cells. Checking the third generation solar cells, of special interest, was concentrated on QD-based solar cells [15, 16, 21-23]. Dye-sensitized solar cell (DSSCs) is the first third-generation that has engrossed much consideration due to their low construction cost and geat performance, flexibility in color, shape, and clearity. Dye-sensitized solar cells (DSSCs) are a kind of solar cells that transform the sun's energy to electric vigor using a sensitizing dye [27-28]. DSSCs based on natural dyes though are environmentally friends usually have relatively low efficiencies. DSSCs fabricated using synthetic dyes on the other hand have relatively higher solar-to-electric energy conversion efficiency yet dyes frequently

contain certain metals that are not environment friendly. Solar cells can be built of one single layer of light-absorbing material (single-junction) or use numerous physical shapes (multi-junction) to catch the benefit from diverse absorption and charge segregation mechanisms. Solar cells can be organized into first, second, and third-generation cells. Dye-Sensitized solar cells (DSSC), also somewhen referred to as dye-sensitized cells (DSC), are third-race photovoltaic (solar) cell that changes any seeming glory into electrical power. This novel category of progressed solar cells can be likened to artificial photosynthesis due to the way in which it imitates nature's attraction of light vigor (Figure. 5).

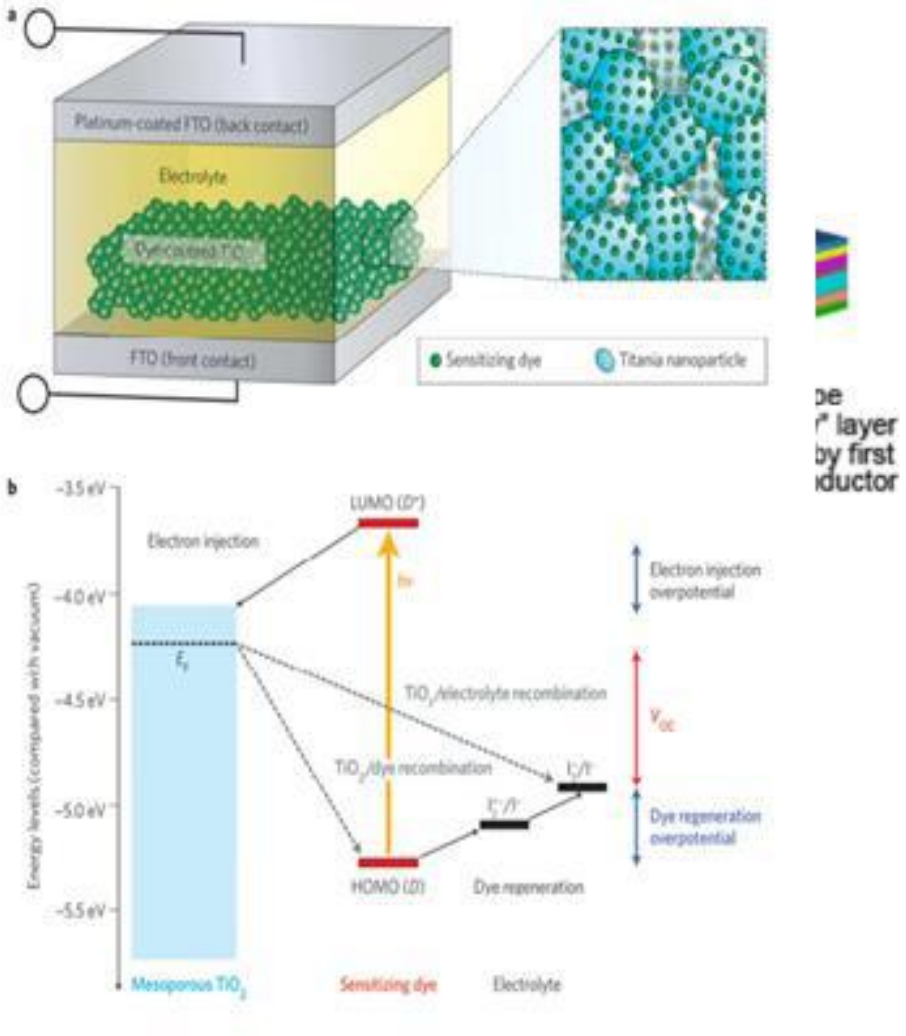

Fig. 6. Dye-sentisized solar cell device schematic and operation.

3. QUANTUM DOTS SENSITIZED SOLAR CELLS

Quantum dot sensitized solar cells (ADSCs) organize one of the important promising approaches to third-generation solar cells. Quantum dot-sensitized solar cells (QDSCs) have appeared as a promising candidate for subsequent-generation solar cells due to the preferable optoelectronic characters of quantum dot (QD) light-harvesting materials, such as great light, thermal, and moisture stability, facilely tunable attraction range, great absorption coefficient, multiple exaction generation probabilities, and solution process ability as well as their easy construction and low-cost accessibility. Semiconductor quantum dots (QDs) have been drawing large consideration lately as a material for solar energy transformation due to their versatile visual and electrical attributes. Of course, quantum dots-sensitized solar cells have been broadly investigated and display promise for the improvement of the subsequent generation of energy, due to the specifications of small expense, environmental defense, and better theoretic vigor transformation efficiency [8-10]. The QD-sensitized solar cell (QDSC) is one of the burgeoning semiconductor QD solar cells that demonstrates promising advances for the next generation of solar cells [11]. On the other hand, QDs can make a profit from non-conventional attributes, as demonstrated in Fig. 3. Usually, we can see the figure of the quantum dot-based solar cells in Fig. 6.

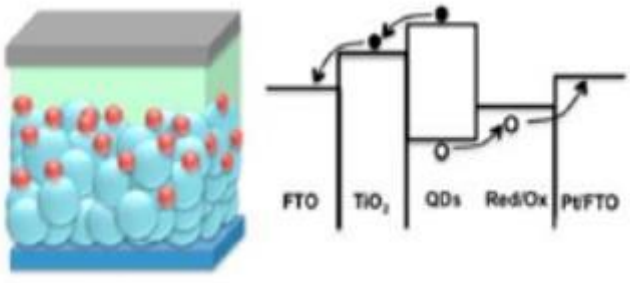

Fig. 7. Schematic illustration of device configurations and energy band diagram of QD based solar cells: QD sensitized solar cell.

The low optical compression of a QD monolayer is compensated by a light path that passes through tens to hundreds of QD monolayers. Dye-sensitized solar cells make use of a similar sense, and light to electric power transformation efficiencies above 10% have been reached with DSCs. The eminent improvement trend of QDSCs displays their great possible as a promising candidate for subsequent-generation photovoltaic cells. Quantum dot-sensitized solar cells (QDSCs) have appeared as a promising candidate for subsequent-generation solar cells due to the preferable optoelectronic aspects of quantum dot (QD) light-harvesting materials, such as high light, thermic, and moisture consistency, facilely tunable sorption span, high absorption coefficient, multiplex exciton generation probabilities, and solution processability as well as their easy construction and low-cost accessibility [29]. The prominent progression tendency of QDSCs displays their excellent possibility as a promising candidate for subsequent-generation photovoltaic cells. Although the election of appropriate material combinations in QDSCs is momentous, we accentuate that good control over the interface processes is critical for systems' operation and betterment [30].

4. COCLUSION

Solar energy is reliable to be the most promising renewable energy resource due to its fascinating properties such as being inexhaustible and environmentally friendly. A solar cell is an electronic system that straightly changes sunlight into electricity. The utilization of solar vigor is boosting in homes as well. Residential appliances can easily use electricity generated through solar power. Dye-Sensitized solar cells (DSSC), also somewhen referred to as dye-sensitized cells (DSC), are third-race photovoltaic (solar) cell that changes any seeming glory into electrical power. The eminent improvement trend of QDSCs displays their great possible as a promising candidate for subsequent-generation photovoltaic cells. Quantum dots illustrate a warranty for utilization in a vast diversity of uses from the quantum PCs of things to come, to medicinal facilities, high goals TV screens, and family lighting. Quantum dots are nanoscale materials that have contrasting optical attributes related to their physical measure. in as much as quantum mechanical impacts, where the potent semiconductor bandgap of the material increases as size decreases. The urgent preferred status of Quantum dots is the capacity to tune light evacuation to a specific modulation and the content to use a singular semiconducting material to emerge at several frequencies by using bits of different measures. This has displayed a particularly desirable status by boosting red and green light when consisting of a blue LED light source, making more powerful the age of white light yield.

[1] *T. Suhasini, P.M. Reddy, & C.R.G. Reddy.* 2020. A Review of Quantum Dots and Its Applications.

[2] *L.D. Field, S.A. Walper, K. Susumu, G. Lasarte-Aragones, Oh.E. Medintz, I. L. & J.B. Delehanty.* 2018. A quantum dot-protein bioconjugate that provides for extracellular control of intracellular drug release. Bioconjugate Chemistry, 29, 7, 2455-2467.

[3] *Q. Duan, Y. Ma, M. Che, B. Zhang, Y. Zhang, Y. Li, ... & S. Sang.* 2019. Fluorescent carbon dots as carriers for intracellular doxorubicin delivery and track. Journal of Drug Delivery Science and Technology, 49, 527-533.

[4] *U. Badıllı, F. Mollarasouli, N.K. Bakirhan, Y. Ozkan & S.A. Ozkan.* 2020. Role of quantum dots in pharmaceutical and biomedical analysis, and its application in drug delivery. TrAC Trends in Analytical Chemistry, 131, 116013.

[5] *M.C. Dos Santos, W.R. Algar, I.L. Medintz & N. Hildebrandt.* 2020. Quantum dots for Förster resonance energy transfer (FRET). TrAC Trends in Analytical Chemistry, 125, 115819.

[6] *D.K. Pandurangan, & K.S. Mounika.* 2012. Quantum dot aptamers-an emerging technology with wide scope in pharmacy. International Journal of Pharmacy and Pharmaceutical Sciences, 4(3), 24-31.

[7] *U. Badıllı, F. Mollarasouli, N.K. Bakirhan,*

Y. Ozkan & S.A. Ozkan. 2020. Role of quantum dots in pharmaceutical and biomedical analysis, and its application in drug delivery. TrAC Trends in Analytical Chemistry, 131, 116013.

[8] *M. Gratzel.* Nature, 414 (2001), p. 338-344.

[9] *P.V. Kamat, K Tvrdy, D.R Baker, and Radich, J.G, Chem.* Rev. Forum vol. 110 (2010), p. 6664-6688.

[10] *I Mora-Sero, J. Bisquert.* J Phys. Chem. Lett. Forum vol. 1 (2010), p. 3046-3052.

[11] *J. Tian & G. Cao.* (2013). Semiconductor quantum dot-sensitized solar cells. Nano reviews, 4(1), 22578.

[12] *M. Graetzel.* Acc. Chem. Res., 2009, 42, 1788–1798.

[13] *Y.J. Cheng, S.H. Yang and C.S. Hsu.* Chem. Rev., 2009, 109, 5868–5923.

[14] *S. Guenes, H. Neugebauer and N.S. Sariciftci.* Chem. Rev., 2007, 107, 1324–1338.

[15] *G.H. Carey, A.L. Abdelhady, Z. Ning, S.M. Thon, O.M. Bakr and E.H. Sargent.* Chem. Rev., 2015, 115, 12732–12763.

[16] *A.J. Nozik, M.C. Beard, J.M. Luther, M. Law, R.J. Ellingson and J.C. Johnson.* Chem. Rev., 2010, 110, 6873–6890.

[17] *A. Kojima, K. Teshima, Y. Shirai and T. Miyasaka, J. Am.* Chem. Soc., 2009, 131, 6050–6051.

[18] *G. Hodes.* Science, 2013, 342, 317–318.

[19] *M.M. Lee, J. Teuscher, T. Miyasaka, T. N. Murakami and H.J. Snaith.* Science, 2012, 338, 643–647.

[20] *A. Hagfeldt, G. Boschloo, L. Sun, L. Kloo and H. Pettersson.* Chem. Rev., 2010, 110, 6595–6663.

[21] *I. J. Kramer and E. H. Sargent.* ACS Nano, 2011, 5, 8506–8514.

[22] *P.V. Kamat, K. Tvrdy, D.R. Baker and J.G. Radich.* Chem. Rev., 2010, 110, 6664–6688.

[23] *I.J. Kramer and E.H. Sargent.* Chem. Rev., 2014, 114, 863–882.

[24] *R.E. Smalley.* Abstr. Paper Am. Chem. Soc., 2003, 226, U24

[25] *J. Wu, Z. Lan, J. Lin, M. Huang, Y. Huang, L. Fan and G. Luo.* Chem. Rev., 2015, 115, 2136–2173.

[26] *J. Wu, Z. Lan, J. Lin, M. Huang, Y. Huang, L. Fan, G. Luo, Y. Lin, Y. Xie and Y. Wei.* Chem. Soc. Rev., 2017, 46, 5975–6023.

[27] *D. Wei.* 2010. Dye-sensitized solar cells. International journal of molecular sciences, 11(3), 1103-1113.

[28] *M. Ye, X. Wen, M. Wang, J. Iocozzia, N. Zhang, C. Lin, & Z. Lin.* 2015. Recent advances in dye-sensitized solar cells: from photoanodes, sensitizers and electrolytes to counter electrodes. Materials Today, 18(3), 155-162.

[29] *Z. Pan, H. Rao, I. Mora-Seró, J. Bisquert & X. Zhong.* 2018. Quantum dot-sensitized solar cells. Chemical Society Reviews, 47(20), 7659-7702.

[30] *S. Rühle, M. Shalom, & A. Zaban.* 2010. Quantum-dot-sensitized solar cells. ChemPhysChem, 11(11), 2290-2304.

Received: 28.04.2022

EXCITATION OF UNSTABLE WAVES IN MULTI-VALLEY SEMICONDUCTORS GaAs TYPE IN EXTERNAL ELECTRIC AND STRONG MAGNETIC FIELDS

E.R. HASANOV[1,2], G.M. MAMMADOVA[2], Sh.G. KHALILOVA[2]
[1]Baku State University Acad. Z. Khalilov,str.23, Baku, Azerbaijan Republic
[2]Institute of Physics, ANAS, AZ-1143, H. Javid 131, Baku, Azerbaijan Republic
shahlaganbarova@gmail.com

Using the Boltzmann kinetic equation, the frequency of excited waves in two-valley semiconductors of the GaAs type in external electric and strong magnetic fields ($\mu H > c$) is theoretically calculated. Analytical expressions are found for the critical electric field at which an unstable electromagnetic wave is excited. A characteristic expression for the magnetic field H_{char} is found. The oscillation frequency of the electric field is calculated in three cases: 1) $H = H_{char}$, 2) $H > H_{char}$, 3) $H < H_{char}$. It is found that the frequency of the excited waves has the highest value in the case of $H > H_{char}$. It has been proven that the geometry of the sample L_x, L_y, L_z must be determined when unstable waves are excited inside the sample. The ratios between the sizes L_x, L_y, L_z are found. The directions of the external electric and magnetic fields significantly affect the frequencies of the excited waves. The theoretical calculation was carried out at $\vec{E}_0 \| \vec{H}_0$.

Keywords: effect Gunn's, Boltzmann equation, multi-valley semiconductors, external electric field, magnetic field, increment, frequency.
PACS: 78,55, 73.22.CD, 73.22

INTRODUCTION

In theoretical studies [1–5], the excited oscillation of unstable waves was calculated inside a two-valley semiconductor of the GaAs type. These theoretical works were done when the external electric field is strong, i.e. $\vartheta_{дреф} > \vartheta_{зв}$. This criterion is satisfied if the external electric field is $E_0 > \frac{\vartheta_{зв}}{\mu_{под}}$ ($\mu_{под}$ -mobility of charge carriers). The external magnetic field changes as $\mu H > c$.

In the above works, a theoretical study was carried out with the fulfillment of the condition

$$\frac{dj}{dE} = \sigma_d = 0 \qquad (1)$$

(j is the current flux density, E is the electric field, σ_d is the differential conductivity). However, from condition (1) it is impossible to determine the oscillation frequencies inside the sample. Therefore, to calculate the oscillation frequency of the excited wave inside the sample, we proceed as follows. First, the current density is calculated by applying the Boltzmann kinetic equation. After that, we calculate the current density using the Maxwell equation

$$\frac{\partial \vec{H}'}{\partial t} = -crot\vec{E}' \qquad (2)$$

The current density

$$\vec{j} = \sigma\vec{E} + \sigma_1\left[\vec{E}\vec{H}\right] + \sigma_2\vec{H}\left[\vec{E}\vec{H}\right] \qquad (3)$$

At condition

$$\vec{E}_0 = \vec{h}E_0 , \quad \vec{H}_0 = \vec{h}H_0 \qquad (4)$$

This task is quite capable of determining the oscillation frequency of the excited waves inside the sample.

THEORY

Figure 1 shows the dependence of the current density in a spatially homogeneous system on the field strength. Here, the volt-ampere characteristics has a falling section and in the region $j_2 < j < j_p$, the field strength is a multivalued function of the current density. In this region, the system is in one of three states. Since the Gunn effect is associated with an N-shaped characteristic, electrical domains appear with negative differential conductivity. Domains appear by the Ridley-Watkins-Hilsum mechanism [5, 6]. Figure 2 shows the dispersion law in GaAs.

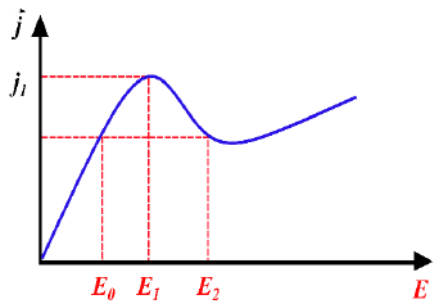

Fig.1. Dependence of the current density on the electric field in two-valley semiconductors of the GaAs type N-shaped characteristic.

131, H.Javid ave, AZ-1143, Baku
ANAS, Institute of Physics
E-mail: jophphysics@gmail.com

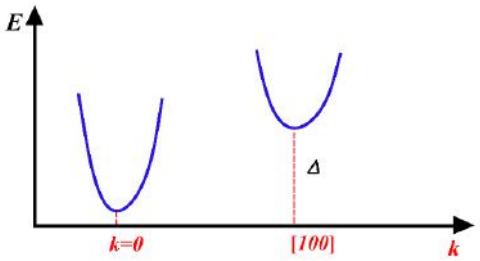

Fig.2. Dependence of the electron energy on the wave vector in GaAs.

The energy distance between the minimum $\Delta = 0.36eV$, $\Delta >> T_p$ is the lattice temperature. The presence of upper minimum does not affect the electron statistics. At a sufficiently high temperature, the electrons go to the upper minimum. Effective mass of electrons

$$m_a << m_b \tag{5}$$

m_a, $m_б$- effective mass of electrons in the lower and upper valleys, respectively.

Electron mobility

$$\mu_a << \mu_b \tag{6}$$

Then

$$\vec{j} = en_a\mu_a\vec{E} + en_b\mu_b\vec{E} \tag{7}$$

electron concentration

$$n = n_a + n_b = const \tag{8}$$

$eEl >> k_0T$ (e is elementary charge, l is electron mean free path). Diffusion current is neglected. Intervalley scattering is small compared to intravalley scattering. When solving the Boltzmann equation, the conditions for the appearance of current fluctuations were obtained.

Until now, there are no theoretical works of the Gunn effect, which take into account the intervalley scattering of the application of the Boltzmann kinetic equation.

In this paper, we will analyze the effect of a strong magnetic field on the Gunn effect, taking into account the above.

BASIC EQUATIONS OF THE PROBLEM

The state of charge carriers, described by the distribution function $f\left(\vec{k},\vec{r}\right)$, which is the probability of electrons with a wave vector $\vec{k}$ ($\hbar\vec{k}$ is quasi-momentum) located near the point $\vec{r}$, is found from the Boltzmann kinetic equation. In a stationary process, the distribution function $f\left(\vec{k},\vec{r}\right)$does not depend on time, but under the influence of lattice vibrations (phonons) and crystal defects and under the influence of external factors, it changes, and these factors mutually compensate each other.

$$\left(\frac{\partial f}{\partial t}\right)_{exter} + \left(\frac{\partial f}{\partial t}\right)_{coll} = 0 \tag{9}$$

In the presence of external electric and magnetic fields, equation (9) has the form [7]

$$\vartheta\nabla_{\vec{r}} f + \frac{e}{h}\left\{\vec{E} + \frac{1}{c}\left[\vec{\vartheta}\vec{H}\right]\right\}\nabla_{\vec{k}} f = \left(\frac{\partial f}{\partial t}\right)_{coll} \tag{10}$$

Where $\vec{\vartheta} = \frac{1}{\hbar}\nabla_k\varepsilon\left(\vec{k}\right)$, ϑ is the electron velocity, $\nabla_{\vec{r}}$ and $\nabla_{\vec{k}}$ is the gradient in the space of coordinates and wave vectors. It is assumed that for the lower valley, intervalley scattering prevails over intravalley scattering, and for the upper valley, intravalley scattering prevails over intervalley scattering. Then the Boltzmann equation for the lower valley

$$\left(\frac{\partial f}{\partial t}\right)_{inter} + \left(\frac{\partial f}{\partial t}\right)_{intervalley} = 0 \tag{11}$$

For the upper valley

$$\left(\frac{\partial f^b}{\partial t}\right)_{inter} + \left(\frac{\partial f^b}{\partial t}\right) = 0 \tag{12}$$

Davydov [4] showed that in a strong electric field the distribution function has the form:

$$f = f_0 + \frac{\vec{p}}{p}\vec{f}_1 \tag{13}$$

f_0 is equilibrium distribution function, $\vec{p}$ is momentum of charge carriers.

It is clear that one can write

$$f^a = f_0^a + \frac{\vec{p}}{p}\vec{f}_1^a,\ f^b = f_0^b + \frac{\vec{p}}{p}\vec{f}_1^b \tag{14}$$

The distribution function $f\left(\vec{k},\vec{r}\right)$ was found from equation (12) in [4]

$$f_0^a = Be^{-\alpha_a(\varepsilon-\Delta)^2} \tag{15}$$

$$f_1^b = -\frac{em_bl_b}{p}\vec{p}\frac{\partial f_0^b}{\partial p} \tag{16}$$

Here

$$l_b = \frac{\pi\hbar^4\rho u_0^2}{D^2m_b^2k_0T} \tag{17}$$

$$\alpha_a = \frac{3D^4 m_b^5 k_0 T}{e^2 \pi^2 \hbar^8 \rho^2 u_0^2} \tag{18}$$

It is clear that for the valley "a" you can write similar formulas (17-18) replacing "a" with "b". l_b is the mean free path, D is the deformation potential, T is the temperature of the solution, ρ is the density of the crystal, u_0 is the speed of sound in the crystal.

Full current

$$\vec{j} = \vec{j}_a + \vec{j}_b \tag{19}$$

$$\vec{j} = \frac{2e}{(2\pi)^3} \int_0^\infty \frac{\vec{p}}{p} \vec{f} \vec{\vartheta} d\vec{k} \tag{20}$$

In an external electric and magnetic field, for intravalley scattering f_1^b it has the following form [4]

$$f_1^b = -\frac{e m_b l_b}{p} \frac{\partial f_0^b}{\partial p} \cdot \frac{\vec{E} + \left(\frac{e l_b}{cp}\right)\left[\vec{E}\vec{H}\right] + \left(\frac{e l_b}{cp}\right)^2 \vec{H}\left[\vec{E}\vec{H}\right]}{1 + \left(\frac{e l_b}{cp}\right)^2 H^2} \tag{21}$$

$$\alpha_b = \frac{3D^4 m_b^5 k_0 T \left[1 + \left(\frac{e l_b}{cp}\right)^2 H^2\right]}{e^2 \pi^2 \hbar^8 \rho^2 u_0^2 \left[E^2 + \left(\frac{e l_b}{cp}\right)^2 \left(\vec{E}\vec{H}\right)^2\right]} \tag{22}$$

If we replace "b" with "a" in (21-22) f_1^b and α_b are obtained. After a simple calculation of the current density $\vec{j}_a$ and $\vec{j}_b$ from (16) it turns out:

$$\vec{j}_a = \frac{e^2 l_a \alpha_a A}{12\pi^2 \hbar^2 m_a^2} \left\{ \vec{E} \frac{c^2}{e^2 l_a^2 H^2} \left(\frac{4m_a^2}{\alpha_a}\right)^2 + \left[\vec{E}\vec{H}\right] + \frac{c\Gamma\left(7/4\right)}{e l_a H^2} \left(\frac{4m_a^2}{\alpha_a}\right)^{7/4} + \vec{H}\left[\vec{E}\vec{H}\right] + \frac{\Gamma\left(3/2\right)}{H^2} \left(\frac{4m_a^2}{\alpha_a}\right)^{3/2} \right\} \tag{23}$$

After calculating the total current by formula (19)

$$j_z' = \frac{8nc^2 m_a^{1/2}}{3\sqrt{2}\Gamma\left(3/2\right) \cdot l_a} \frac{E_z'}{H^2} \cdot \frac{\alpha_a^{-1/4}}{1 + \gamma_z^{-3/2} \, 3/4 \, \beta} \left\{ 1 + t\gamma_z^{-2}\beta + \frac{e^2 l_a^2 \alpha_a^{1/2}}{2c^2 m_a} H^2 \Gamma\left(3/2\right) \left[1 + t\gamma^{-1} z^{1/2} \beta\right] \right\} \tag{24}$$

Here

$$A = t\gamma^{-1} z^{-1/2} = \frac{m_b}{m_a}, \; \gamma = \frac{m_a}{m_b}, z = \frac{\alpha_a}{\alpha_b}, \; t = \frac{l_b}{l_a}, \; \beta = z^{-1} e^{-\alpha_a \Delta^2}$$

$$e^{-\alpha_a \Delta^2} = e^{-\left(\frac{E_x}{E}\right)^2} = \left(1 - \frac{E_x}{E}\right)^2, \; E^2 = \frac{3D^4 m_0 m_a^3 k_0 T}{e^2 \pi^2 \hbar^8 \rho^2 u_0^2}$$

Let us write (24) in the following form

$$\vec{j} = \sigma \vec{E} + \sigma_1 \left[\vec{E}\vec{h}\right] + \sigma_2 \vec{h}\left[\vec{E}\vec{h}\right] \tag{25}$$

$\vec{h}$ is unit vector in the magnetic field. For current density j_z' (21), it is directed the electric field and magnetic field H_0 as in (4) as follows

The value E_x is derived from the following condition

$$\frac{dj_z'}{dE_z'} = 0 \tag{26}$$

For GaAs - E_x^2

$$E_x^2 = 43.84 \left(V/sm\right)^2 \tag{27}$$

For strong electric fields, the condition

$$E >> E_x \tag{28}$$

quite satisfied. Now we calculate the frequency of current oscillations. An alternating magnetic field H' arises when an alternating electric field E' is excited inside the medium

$$\frac{\partial \vec{H}'}{\partial t} = -crot\vec{E}' \tag{29}$$

In the presence of electric and magnetic fields, the current density has the form

$$\vec{j} = \sigma\vec{E} + \sigma_1\left[\vec{E}\vec{H}\right] + \sigma_2\vec{H}\left[\vec{E}\vec{H}\right] \tag{30}$$

By directing the external electric and magnetic field according to (4), taking into account (29), j'_x, j'_y, j'_z are found from (30) ($\vec{h}$ -unit vector in z).

$$j'_x = \sigma\left(1-\frac{\mu k_z E_0}{\omega}\right)E'_x + \sigma_1\left[\left(1+\frac{ck_x E_0}{\omega H_0}\right)-\frac{2\sigma_2 ck_z E_0}{\omega H_0}\right]E'_y + \frac{2\sigma_2 ck_y E_0}{\omega H_0}E'_z \tag{31}$$

$$j'_y = -\sigma_1 E'_x + \left(\sigma - \frac{\sigma_1 ck_z E_0}{\omega H_0}\right)E'_y + \sigma_1\left(1+\frac{ck_y E_0}{\omega H_0}\right)E'_z \tag{32}$$

$$j'_z = (\sigma+\sigma_2)E'_z - \frac{2\sigma_2 ck_y E_0}{\omega H_0}\left(E'_x + E'_y\right) \tag{33}$$

For $j'_x = 0$ and , E'_z and E'_y are found from (31-32), E'_z and E'_y supplying and to (33) under the condition $\mu H_0 >> c$

$$j'_z = \left[\sigma_2 + \frac{2\sigma_2 ck_x E_0}{\omega H_0}\left(1+\frac{c}{\mu H}\frac{ck_z E_0}{\omega}+\frac{c}{\mu H_0}\frac{ck_y k_z \mu E_0}{\omega_0^2}\cdot\frac{E_0}{H_0}-\frac{ck_y}{\omega}\frac{c}{\mu H_0}\frac{E_0}{H_0}\right)+\right.$$
$$\left.+\frac{2\sigma_2 ck_y}{\omega}\cdot\frac{E_0}{H_0}\left(\frac{ck_y}{\omega}+\frac{c\mu k_z ck_y \mu E_0}{\omega^2}\right)\frac{E_0}{H_0}\right]E'_z \tag{34}$$

When strong $\mu H_0 >> c$, equating (34) and (24) yields the following dispersion equation

$$(\sigma_2 - \tilde{\sigma}\Phi)\omega^3 + \frac{2\sigma_2 ck_x E_0}{H_0}\left(1+\frac{E_0}{H_0}\right)\omega^2 + \frac{2\sigma_2 ck_x E_0}{H_0}\omega + \frac{\sigma_2 ck_x E_0}{H_0}ck_y\mu k_z E_0\left(\frac{c}{\mu H_0}\cdot\frac{E_0}{H_0}+2\frac{E_0}{H_0}\right)=0 \tag{35}$$

Denote σ and Φ

$$\tilde{\sigma} = \frac{8nc^2 m_a^{1/2}\alpha_a^{-1/4}}{3\sqrt{2}\Gamma\left(3/2\right)l_a H^2}, \Phi = \frac{1}{1+\gamma_z^{-3/2}z^{9/4}\beta}\left\{1+t\gamma^{-2}Z\beta+\frac{e^2 l_a^2 H^2 \alpha_a^{1/2}}{2c^2 m_a}\Gamma\left(3/2\right)+\left(1+t\gamma^{-1}z^{1/2}\beta\right)\right\} \tag{36}$$

i.e.

$$H_x = H_0 = \left[\frac{8c^2 m_a^{1/2}\alpha_a^{-1/4}}{3\sqrt{2}\Gamma\left(3/2\right)e\mu l_a}\right] \tag{37}$$

The following dispersion equation is obtained

$$\left(\frac{\sigma_2'}{\sigma_2}-1\right)\omega^4+2\omega_x\frac{E_0}{H_0}\omega^3+\left(2\omega_x\omega_z\frac{E_0}{H_0}-2\omega_y\omega_x\frac{c}{\mu H}\frac{E_0}{H_0}+2\omega_y^2\frac{E_0}{H_0}\right)\omega^2+$$
$$+\left(2\omega_x\frac{c}{\mu H}\omega_y\omega_z+2\omega_y^2\omega_z\frac{E_0}{H_0}\right)\omega=0 \qquad (38)$$

I case $H_0=H_x$

Then from (38) we obtain the following dispersion equation

$$\Omega_1\omega^2+\Omega_2^2\omega+\Omega_3^2=0 \qquad (39)$$

Solution (39) shows that the growing wave at

$$L_x=\frac{c}{\mu H}L_y \qquad (40)$$

and electric field

$$E_0>\frac{H_0}{4}\frac{\mu H}{c}\cdot\frac{L_x}{L_z} \qquad (41)$$

Ratio $\frac{\omega_0}{\gamma_0}$ (γ is growth increment)

$$\frac{\omega_0}{\gamma}=\left(\frac{L_y}{L_z}\right)^{1/2}\left(\frac{\mu H}{c}\right)^{1/2}\frac{E_0}{H_0}>>1 \qquad (42)$$

i.e. excitation of oscillation by increment

$$\gamma=\frac{\left[2\omega_x\omega_z\omega_x\left(\frac{c}{\mu H}\right)^2+2\omega_x^2\omega_z\frac{E_0}{H_0}\left(\frac{c}{\mu H}\right)^2\right]^{1/2}}{\left(2\omega_x\frac{E_0}{H_0}\right)^{1/2}}=\left(\frac{\omega_z}{\omega_x}\right)^{1/2}\cdot\frac{\frac{c}{\mu H}\left(1+\frac{E_0}{H_0}\right)^{1/2}}{\left(\frac{E_0}{H_0}\right)^{1/2}}\omega_x \qquad (43)$$

Here $\omega_z=ck_z$, $\omega_x=ck_x$

To solve the dispersion equation (38) when (40) is satisfied,

$$x^3+\frac{2E_0}{H_0}x^2+\frac{\omega_z E_0}{\omega_x H_0\varphi}x+\frac{2\omega_z}{\omega_x\varphi}\left(\frac{c}{\mu H}\right)^2=0 \qquad (44)$$

$$\varphi=\frac{\sigma_2'}{\sigma_2}-1$$

The dispersion equation has the following form

$$x^3+ax^2+bx+c=0 \qquad (45)$$

$$x=\frac{\omega}{\omega_x}$$

From (45) the equation is reduced to the form

$$y^3+3py+q=0 \qquad (46)$$

Here $y=\frac{b}{3a}$

Applying the Cardano formula to equation (46) we get 3 roots

$$y_1=u+\vartheta$$
$$y_2=\varepsilon_1 u+\varepsilon_2\vartheta=\left(-\frac{1}{2}+i\frac{\sqrt{3}}{2}\right)u+\left(-\frac{1}{2}-i\frac{\sqrt{3}}{2}\right)\vartheta=-\frac{u+\vartheta}{2}+i\frac{\sqrt{3}}{2}(u-\vartheta)$$
$$y_3=\left(-\frac{1}{2}-i\frac{\sqrt{3}}{2}\right)u+\left(-\frac{1}{2}+i\frac{\sqrt{3}}{2}\right)\vartheta=-\frac{u+\vartheta}{2}+i\frac{\sqrt{3}}{2}(\vartheta-u) \qquad (47)$$
$$u=\sqrt[3]{-q+\sqrt{q^2+p^3}}$$
$$\vartheta=-\sqrt[3]{q+\sqrt{q^2+p^3}}$$

$$3p=\frac{3ac-b^2}{3a^2}$$

$$2q = \frac{2b^3}{27q^3} - \frac{cb}{3a^3} + \frac{d}{a}$$

Substituting the values of q and p into equations (47)

$$E_0 = (6)^{1/2}\frac{c}{\mu} \text{ at } a = -1, \text{ i.e } H_0 >> H_x \tag{48}$$

A growing wave with a certain frequency is excited. In case when $H << H_x$

$$x = -\frac{bH^2}{3H_x^2} + i\frac{\sqrt{3}}{2}\left(\frac{2bH^2}{3H_x^2} + \frac{2bH^2}{3H_x^2}\right) = -\frac{bH^2}{3H_x^2} + i2\sqrt{3}\frac{bH^2}{3H_x^2} \tag{49}$$

From (49) it can be seen that the ratio of the increment to the frequency

$$\omega_0 = -ck_x\frac{bH^2}{3H_x^2}, \quad \omega_1 = -\frac{2}{\sqrt{3}}\frac{bH^2}{H_x^2}ck_x$$

$$\frac{\omega_1}{\omega_0} = \frac{2}{\sqrt{3}} = 2\sqrt{3} > 1 \tag{50}$$

This inequality occurs when

$$E_0 > H_0\left(\frac{L_x}{24L_z}\right)^{1/3}\left(\frac{H_x}{H_0}\right)^{4/3}\left(\frac{c}{\mu H}\right)^{2/3} \tag{51}$$

Substituting (40) into (51) we obtain the following relationship between L_x and L_z

$$L_y < L_z 3^{5/6}\cdot 2^{1/2}\left(\frac{H_x}{H}\right)^{2/3}\left(\frac{c}{\mu H}\right)^{1/3} \tag{52}$$

Thus, a growing wave of an electromagnetic nature is excited in two-valley semiconductors of the GaAs type. The growth rate of this wave changes significantly with the change in the ratio $\frac{H}{H_x}$. The excited wave depends very strongly on the size of the crystal (L_x, L_y, L_z).

DISCUSSION OF THE RESULTS

It is shown that the radiation of electromagnetic waves in the form of these media occurs in three cases I, II, III. Thus, an unstable wave is not excited at all values of the magnetic field, only at certain values relative to the characteristic magnetic field H_x.

[1] *B.K. Ridley, T.B. Watkins.* The Possibility of Negative Resistance Effects in Semiconductors, Pros.Phys.Soc., 1961, v. 78, p. 293.

[2] *C.H. Hilsum.* Transferred Electron Amplifiers and Oscillators. Proc. IRE. 1962, V.50, p.185.

[3] *A.I. Anselm.* Introduction to the theory of semiconductors. Moscow. M. 1962.

[4] *B.I. Davydov.* On the theory of the motion of electrons in gases and in semiconductors. ZhETF. 1937, T.7., 1069.

[5] *E.R. Hasanov, R.A. Hasanova.* External and Internal Instability in the Medium Having Electron Typ Conductivity, IOSR Journal of Applied Physics, (May-June. 2018), Volume 10, Issue 3, Ver. II, p.18-26.

[6] *E. Conwell.* Kinetic properties of semiconductors in strong electric fields. ("Mir" Moscow, 1970), p.339-344.

[7] *L.E. Gurevich, E.R. Hasanov.* Spontaneous current oscillations in semiconductors with deep traps in strong electric and magnetic fields, *Solid State Physics*, 1969, vol. 11 № 12, p.3544-3548.

Received: 17.05.2022

SPATIAL MODELS OF GLUCOSE AND DI-GLUCOSE OPTIMIZED STRUCTURES

G.D. ABBASOVA, E.Z. ALIYEV, G.R. SAFARLI
Chair of optics and molecular physics, Baku State University,
Z. Khalilov st.23, AZ-1148, Baku, Azerbaijan

The spatial and electron structure of dextran-glucose monomer units is investigated by semiempirical methods of molecular mechanics and quantum chemistry with the help of computer calculative programs. Glucose and di-glucose complexes with iron oxide Fe_2O_3 are studied. The geometric parameters characterizing the energy-stable states of investigated compounds and their coordination complexes are calculated.

Keywords: dextran, glucose, di-glucose, iron oxide.
PACS: 3115; 3315

INTRODUCTION

The nano-medicine which is new interdisciplinary direction including the control under biological systems on the base of nano-technology achievements, is the one of the priority directions of the modern medicine. The scientists all over the World work under development of technologies for nano-medicine field including first of all address delivery of medicines to affected cells (cancer cells; cells infected by virus; atherosclerotic plaques and etc), diagnostics with the help of quantum dots, chip laboratories, new antibacterial agents. The developed systems of medicine delivery are used practically in all fields of medicine: endocrinology, pulmonology, cardiology, oncology and etc. The investigations on construction of nano-devices, the implantation of which into human brain allows us to increase the human knowledge and rate of its thinking in many times, appear. Big successes in the field of gene therapy are achieved.

The modern nano-medicine has achieved the great success in the search and formation of new classes of medicines used in the therapy of cancer illnesses. Known that antineoplastic drugs have the low therapeutic indexes and their use efficiency is limited by high general toxicity, metabolic instability in organism and bad penetration into cancer cell. For the solution of these problems the carriers of anticancer drugs which defend the medicine from ferment influence and prevent their biological degradation in biological liquids, for example, in blood, are used. The principal possibility of liposome application as carriers of such medicines is shown in series of fundamental works. The substance including in liposome not only effectively assimilate the medicine but also causes to increase of medicine life-time because of its release from liposomes.

In the given work the spatial and electron structures of monomer unit dextran-glucose, di-glucose are investigated by methods of molecular modeling and empiric methods of quantum chemistry; their coordination complexes with iron oxide Fe_2O_3 are studied. The electron structures of glucose and di-glucose are calculated on the base of equilibrium nuclear configuration coordinates obtained as a result of molecule geometry optimization in potentials of semiempirical methods of molecular mechanics MM+. In molecular mechanics' methods the atoms are considered as Newtonian particles being in force field and interaction between them is described by potential energy. The potential energy depends on bond length, angles between bonds, dihedral angles of rotation round single bonds and on interaction of unbound molecular fragments with the help of electrostatic forces, Van-der-Waals forces or interactions causing the hydrogen bonds. There are different modifications of calculative programs ((MM+, AMBER, BIO and etc.) in the dependence on approximations used at calculation of force field and on harmonic functions describing this field.

CALCULATION METHODS

In the given work the calculations are carried out with the help of MM^+ method. Big database allows us to form the proteins, polymers, DNA fragments, metal clusters, modern systems of organometallic compound. The semiempirical methods of quantum chemistry in the dependence on use degree of zero differential overlap and approximation of core, Coulomb and exchange integrals included in matrix elements of Fock operator, have the different modifications. These methods MO CCП INDO/1,2,S, CNDO/1,2, MINDO/1,2,3, MNDO, AM1, PM3, MP2, Huckel method and series of other methods are well known. Each of methods allows us to obtain the series of either electron or spectral characteristics the values of which well coincide with the experiment in the result of calculation. In the work the calculations are carried out with the help of the PM3 method parameterized for the atoms of transition metals.

RESULTS AND THEIR DISCUSSION

The results of total energy calculation of glucose and di-glucose before and after molecule geometry optimization by MM^+ method are given in Table 1. The glucose total energy decreases on 16.13 kkal/mol, the di-glucose total energy decreases on 486.21 kkal/mol. These values also characterize the bonding energy in the investigated compounds. The changes in the values of electron energy are the essential ones:

131, H.Javid ave, AZ-1143, Baku
ANAS, Institute of Physics
E-mail: jophphysics@gmail.com

the decrease of electron energy on 828.46 kkal/mol is observed for glucose whereas for di-glucose the relative energy increases on 36747.21 kkal/mol. Correspondingly, the opposite picture is observed at comparison of nuclear repulsion energy: if in glucose the nuclear repulsion energy increases on 844.68 kkal/mol then in di-glucose this value is 37233.42 kkal/mol.

The one of the important molecule characteristics defining their behavior in the different force fields is the dipole moment having the additivity property. The optimized structure of di-glucose is characterized by the value of dipole moment 4.71D which on 1.39 D bigger than sum of dipole moments of glucose isolated molecules.

Table 1.

Calculation results by PM3 method data before (upper line) and after (low line) optimization

Molecule	Energy parameters, kkal/mol				Dipole moment, Debye
	Total energy	Electron energy	Nuclear repulsion energy	Bonding energy	
Glucose	-61301.29	-325723.21	264421.91	-2258.03	2.30
	-61317.42	-324894.75	263577.33	-2274.16	1.66
Di-glucose	-114656.53	-882892.67	768236.14	-3845.47	5.54
	-115142.74	-846145.46	731002.72	-4331.68	4.71

The geometric parameters characterizing the optimized spatial structure of di-glucose molecules are given in Table 2.

Table 2.

Parameters characterizing the low-energy state of di-glucose

Valence angle	**Value (degree)**
O_6-C_5-O_{12}	106.09
C_5-O_{12}-C_{30}	115.62
O_{12}-C_{30}-C_{24}	112.64
C_{30}-C_{24}-O_{29}	104.74
C_{30}-C_{24}-C_{25}	111.42
O_6-C_5-C_4	113.75
C_5-C_4-O_{11}	112.24
C_4-C_5-O_{12}	109.27
Torsion angle	**Value (degree)**
O_6-C_5-O_{12}-C_{30}	89.23
C_5-O_{12}-C_{30}-C_{24}	83.71
O_{12}-C_{30}-C_{24}-O_{29}	103.74
C_{30}-C_{24}-O_{29}-C_{28}	174.81
O_{12}-C_{30}-C_{24}-C_{25}	135.44
O_{11}-C_4-C_5-O_{12}	57.39
C_4-C_5-O_{12}-C_{30}	147.75
O_{29}-C_{28}-C_{27}-C_{26}	50.01
Bond	**Length (Å)**
C_5-O_{12}	1.42
O_{12}-C_{30}	1.41
C_{30}-C_{24}	1.56
C_{24}-O_{29}	1.43
C_{24}-C_{25}	1.55
O_{29}-C_{28}	1.41

In spite of the presence of different substituents of C_5 and C_{30} atoms, bond lengths C_5-O_{12} and C_{30}-O_{12} have practically the similar values which are equal to 1.4177 and 1.4129 Å, correspondingly. The torsion angle defining the glucose molecule orientation relatively each other has the value equal to 83.71^0, i.e. close to direct one.

As it is followed from calculation results, the decrease of negative charge value on oxygen atoms is observed as a result of transition of electron density

from p-orbitals of oxygen atoms on d-orbitals of iron atoms. The length of single bond of Fe-O is equal to 1.776 Å whereas the length of double bond of Fe=O is 1.4858 Å. The valence angle value of Fe-O-Fe which is equal to 76.4^0 provides the maximum good balance between electrostatic interactions of opposite charged atoms.

The results obtained in the given work can be used for construction of pharmacology medicines with potential therapeutic value and satisfying the wide range of qualitative criteria: high activity, high selectivity, minimal toxicity, high biological compatibility.

[1] *A. Petri-Fink, M. Chastellain, L. Juillerat-Jeanneret, A. Ferrari, H. Hofmann.* 2005 Development of functionalized superparamagnetic iron oxide nanoparticles for interaction with human cancer cells. Biomaterials, 2005, v. 26, p. 639-646.

[2] *A.M. Koch, F. Reynolds, H.P. Merkle, R. Weissleder, L. Josephson.* Transport of surface-modified nanoparticles through cell monolayers. Chem Biol Chem., 2005, v.6, p.337-345.

[3] *P. Gould.* Nanoparticles probe biosystems. Materials today, 2004, v. 7, iss. 2, p. 36-43.

[4] *E. Ruoslahti.* Anti-tumor Effect of nanoparticles that target blood clotting in tumor vasculature. Cancer Biology & Therapy, 2007, v.6, is.2, p. 133-134.

[5] *D. Simberg, T. Duza, J.H. Park, M. Essler, J. Pilch, L. Zhang, A.M. Derfus, M. Yang, R.M. Hoffman, S. Bhatia, M.J. Sailor, E. Ruoslahti.* Biomimetic amplification of nanoparticle homing to tumors. PNAS, 2007, v. 104, No. 3, p. 932-936.

[6] *M.R. Saboktakin, A. Maharramov, M.A. Ramazanov.* Synthesis and characterization of polyaniline/poly (p-hydroxyaniline)/Fe_3O_4 magnetic nanocomposite //N.Y.Science Journal, 2008, v.2, no.21, p.14-17. (http://www.sciencepub.org).

[7] *A.K. Gupta, M. Gupta.* Synthesis and surface engineering of iron oxide nanoparticles for biomedical applications. Biomaterials, 2005, v.26, iss.18, p.3995-4021.

[8] *T.K. Jain, M.A. Morales, S.K. Sahoo, Leslie-Pelecky D.L., Labhasetwar V. Iron.* Oxide Nanoparticles for Sustained Delivery of Anticancer Agents. Mol. Pharm., 2005, v. 2, No.3, p. 194 -205.

[9] *N.M. Godjayev, G.D. Abbasova, I.N. Aliyeva.* The investigation of spatial structure of new anticancer drug-molecule CREKA. Journal of Qafqaz University, 2008, №.21, pp.30-37.

Received: 17.05.2022

ISSN 1028-8546

2022, Vol. XXVIII, № 2
Section: En

CONTENTS